SAINT MARY'S UNIVERSITY SINCE 1802

One University. One World. Yours.

Final Report

Implications of Tidal Energy Extraction on Sedimentary Processes within Shallow Intertidal Environments

Queen's UNIVERSITY

Co-PI: Dr. Danika van Proosdij Dept. of Geography, Saint Mary's University and Dr. Ryan Mulligan, Dept. of Civil Engineering, Queen's University

Co-authors: Emma Poirier (Saint Mary's University) and Logan Ashall (Queen's University)

March 31, 2013

Funding provided by:

OERA Offshore Energy Research Association of Nova Scotia

SUMMARY

Sediments are the primary determinants of biological activity in the upper Bay of Fundy. Gaining an understanding of their behavior under varying environmental and energy conditions will provide a critical baseline to model anticipated effects of tidal energy extraction on sensitive intertidal ecosystems such as tidal flats and salt marshes. For example, changes in tidal energy or tidal range can induce changes in hydrodynamic forces, the structure and location of biotic communities and rates of sedimentation and erosion. These changes are most likely to be felt within intertidal communities at the upper reaches of the vertical influence of the tides. Since the processes of sedimentation and erosion are spatially and temporally variable, field data are required over a range of suspended sediment concentrations, current velocities, water depths, topographies, biotic communities (e.g. vegetation and benthos) and wind-wave energy. Any potential energy extraction or change in the tidal range will exert an influence on sediment dynamics within the system. However the magnitude of the change in intertidal areas is currently unknown and may or may not occur within a range of natural variability therefore it is vital to model these processes over a range of environmental conditions.

The purpose of this research project is to assess the implications of tidal energy extraction on sedimentary processes within shallow intertidal ecosystems. We specifically address OERA's research priority area regarding the relationships between tidal energy extraction and inshore areas (e.g. tidal creeks, marshes, intertidal flats). While previous modelling and field validation efforts have been able to resolve hydrodynamic and sedimentary processes at the basin scale (Smith and Mulligan, 2010), we focus on processes within the relatively shallow upper intertidal zone to gather much needed insight into hydrodynamics over smaller scale and ecologically sensitive areas. Our previous field work has already confirmed significant spatial and temporal variability in sedimentary processes between tidal creek and exposed salt marsh/mudflat ecosystems (van Proosdij et al. 2010). The additional data in this project have helped to refine preliminary empirical relationships including seasonal variability in processes, particularly suspended sediment concentration and sediment composition (e.g. grain size and floc fraction).

This study significantly advances our understanding of the seasonal variability in intertidal ecomorphodynamics: the interaction and adjustment of topography, vegetation, fluid and hydrodynamic processes, morphologies and sequence of change dynamics involving the movement of sediment. In addition, it provides the first numerical model in the Bay of Fundy that effectively integrates near and far field hydrodynamic processes and serves as an important step towards three-dimensional modelling the full impacts of tidal energy extraction in these important ecosystems.

In the field study, the seasonal control on deposition was strongest in the channel, seen at the creek and marsh bank stations. At these two stations, deposition and suspended sediment concentration were higher and this occurred in the winter, because of rapid deposition from high sediment supply. On the high marsh,

the amount of sediment in floc form decreased and the seasonal control was less prominent. The period of October to February was the most active period in terms of high suspended sediment concentrations and sediment re-suspension. Episodic events with strong winds and heavy rainfall were effective at changing the grain size distribution of deposited sediment, this re-suspension also changing the characteristics of the sediment in suspension and therefore the incoming sediment on following tidal cycles. In addition, these episodic events appear to play an important role in maintaining equilibrium and a balanced annual sediment budget within the salt marsh tidal creek channel. However, this study also demonstrates that using only one scale of data (e.g. tidal cycle versus seasonal GIS digital elevation models) may lead to an inaccurate estimation of the sediment budget, and more accurate sediment budgets should be developed by integrating over broad spatial and temporal scales.

The three-dimensional high-resolution hydrodynamic model (Delft3D) was used to simulate tidal currents and water levels, calibrated using acoustic observations over multiple tidal cycles in the intertidal zone at Kingsport. Using a system of three interconnected model domains at increasing resolution toward the intertidal zone, high resolution of the salt marsh and drainage channels was attained. A vegetation model that incorporated stem height, diameter and density was implemented and the resulting vegetation was determined to be crucial in reproducing currents in the marsh. A simulation that included turbines in Minas Passage was developed, representing the 2.5 GW of tidal power extraction. The test produced a 3.5% (0.2 m) tidal amplitude decrease within the Kingsport marsh, suggesting that turbines may have impacts on intertidal water level elevations and inundation times. Future work will address sediment dynamics, tidal currents and surface waves in June 2013, corresponding to the dataset collected during the CCGS Hudson research cruise in Minas Basin.

The numerical model was also used to simulate the combined effects of surface waves, tidal currents and sediments with results indicating that storm events have major impacts on sediment transport, with winds that generate fetch-limited surface waves. The waves are important for re-suspension over the shallow tidal flats in the basin, by inducing wave orbital velocities at the seabed that in addition to tidal currents, create strong shear stresses on the bed. The results indicate that locally generated wind waves, can vary significantly over seasonal timescales, contributing up to 1-5 Nm^{-2} to the bottom shear stresses on tidal flats. The added shear stress due to waves leads to increased erosion of the tidal flats around the rim of the basin and increases the suspended sediment concentrations by 100-200 gm^{-3} in intertidal areas and by 10-20 gm^{-3} in deeper areas of the basin, representing a doubling in concentration in these areas. Predicting sediment transport processes in macrotidal environments is therefore dependant on accurate simulation of the combined tidal flow and surface wave field properties.

The results of this project add tremendous value to industry and government partners involved in the Fundy FORCE initiative, but also build on two successful OERA projects led by Danika van Proosdij in collaboration with Peter Smith (Bedford Institute of Oceanography) and Ryan Mulligan (Queen's University). In addition, it contributes directly to building local capacity in environmental effects monitoring and modelling by enriching our baseline data sets, adopting leading edge technologies and, providing "real world" training grounds for young scientists in Canada. This project was the foundation for training two bright young scholars at the Masters level: Emma Poirier at Saint Mary's University and Logan Ashall at Queen's University. An additional three undergraduate research assistants were trained in the

field within the In_CoaST research unit. All team members have presented at regional, national and international conferences, disseminating our research widely and numerous papers will be submitted to referred journals in the near future. We have demonstrated that our team has taken full advantage of OERA's funding opportunity. By building on previous project investments and acquiring new data at key sites, we have developed a high resolution hydrodynamic model allowing us to integrate the field and model results that will help simulate anticipated TISEC installations while minimizing environmental impacts. Continuing work develop a combined wave/current/sediment transport model that can be used to investigate the impacts of turbines on ecologically sensitive intertidal areas. Finally, the project results will benefit Nova Scotians by serving as a baseline that can be used to understand whether or not future changes associated with commercial scale tidal power generating structures in the Minas Passage are outside the range of natural variability of stressors that intertidal ecosystems have adequate resilience to respond.

Table of Contents

Table of Figures

INTRODUCTION

Sediments are the primary determinants of biological activities in the Upper Bay of Fundy, notably benthic habitat and ecosystem processes; being able to forecast their behaviour is a high priority as indicated in the SEA report (Whitford, 2008). These areas are of high importance for primary productivity and functioning of the estuarine ecosystem. However, our current understanding of sedimentary processes operating in the upper intertidal zone is extremely limited and significantly limits our ability to accurately model far field effects of energy extraction. We know that a decrease in velocity will affect the transport and deposition of sediments and alter their properties (e.g. grain size, cohesiveness, organic matter content) however the relative magnitude of these changes in upper intertidal zones such as tidal creeks and salt marshes is unknown. In addition, we do not know if these changes would fall within the bounds of natural variability or how processes would be either amplified or dampened with climate change.

While previous modelling and field validation efforts have been able to resolve hydrodynamic and sedimentary processes at the basin scale (Smith and Mulligan, 2010), we focus on processes within the relatively shallow upper intertidal zone to gather much needed insight into hydrodynamics over smaller scale and ecologically sensitive areas. Our previous field work has already confirmed significant spatial and temporal variability in sedimentary processes between tidal creek and exposed salt marsh/mudflat ecosystems (van Proosdij et al. 2010) as well as the importance of water depth and suspended sediment concentration in controlling sediment deposition (O'Laughlin et al., 2013; O'Laughlin et al., 2014). The additional data in this project will help to refine preliminary empirical relationships including seasonal variability in processes, particularly suspended sediment concentration and sediment composition (e.g. grain size and floc fraction). This study directly addresses a significant gap in our previous understanding of the seasonal variability in intertidal ecomorphodynamic. In addition, it provides the first numerical model in the Bay of Fundy that effectively integrates near and far field hydrodynamic processes and serves as an important step towards three-dimensional modelling the full impacts of tidal energy extraction in these important ecosystems.

Scientific Objectives

The purpose of this research is to assess the implications of changes in tidal energy on sedimentary processes within intertidal ecosystems of the Minas Basin using a hydrodynamic and sediment transport model. The differences in tidal prism and energy between neap and spring tidal cycles will be used as a proxy for energy extraction due to in-stream tidal power devices. In addition, seasonal variations in sediment mobility and sedimentary processes will be addressed. Specific objectives for the proposed research include:

1. Determine the seasonal variability in sediment mobility and distribution during the spring/neap cycle within the intertidal environments during spring, summer and fall.
2. Develop empirical relationships between tidal energy, suspended sediment concentration and resultant sediment deposition within a range of intertidal environments.

3. Determine the natural range of seasonal variability in sedimentary processes (including impact of wave activity and precipitation) within mudflat and salt marsh environments with varying tidal energy over a range of temporal and spatial scales.
4. Develop a high resolution hydrodynamic and sediment transport model using Delft3D of the Cornwallis Estuary under a range of tidal energy conditions.
5. Validate the model using field data.

Study Area

A study site was chosen near Kingsport, NS in the Cornwallis Estuary (Figure 1) in consultation with concurrent OERA project teams at the Bedford Institute of Oceanography and Dalhousie University. This report will focus primarily on work conducted within the tidal creek and adjacent marsh surface (Figure 2) as well as model development from May 2012 to June 2013, however will also place these findings within the context of prior field deployments.

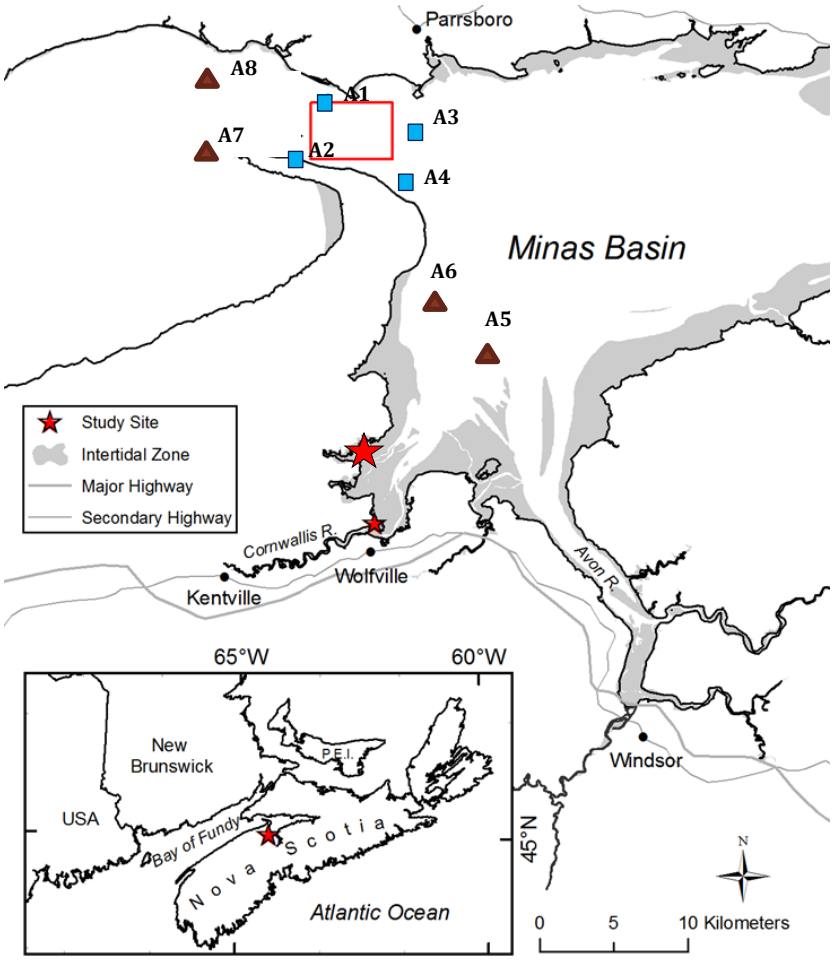

Figure 1: Geographical overview of study area and model domain. The large star denotes Kingsport and the smaller star indicates Starr's Point. The FORCE tidal test area indicated by red box. Summer sensors deployed by the Bedford Institute of Oceanography indicated by triangle, winter sensors indicated as squares.

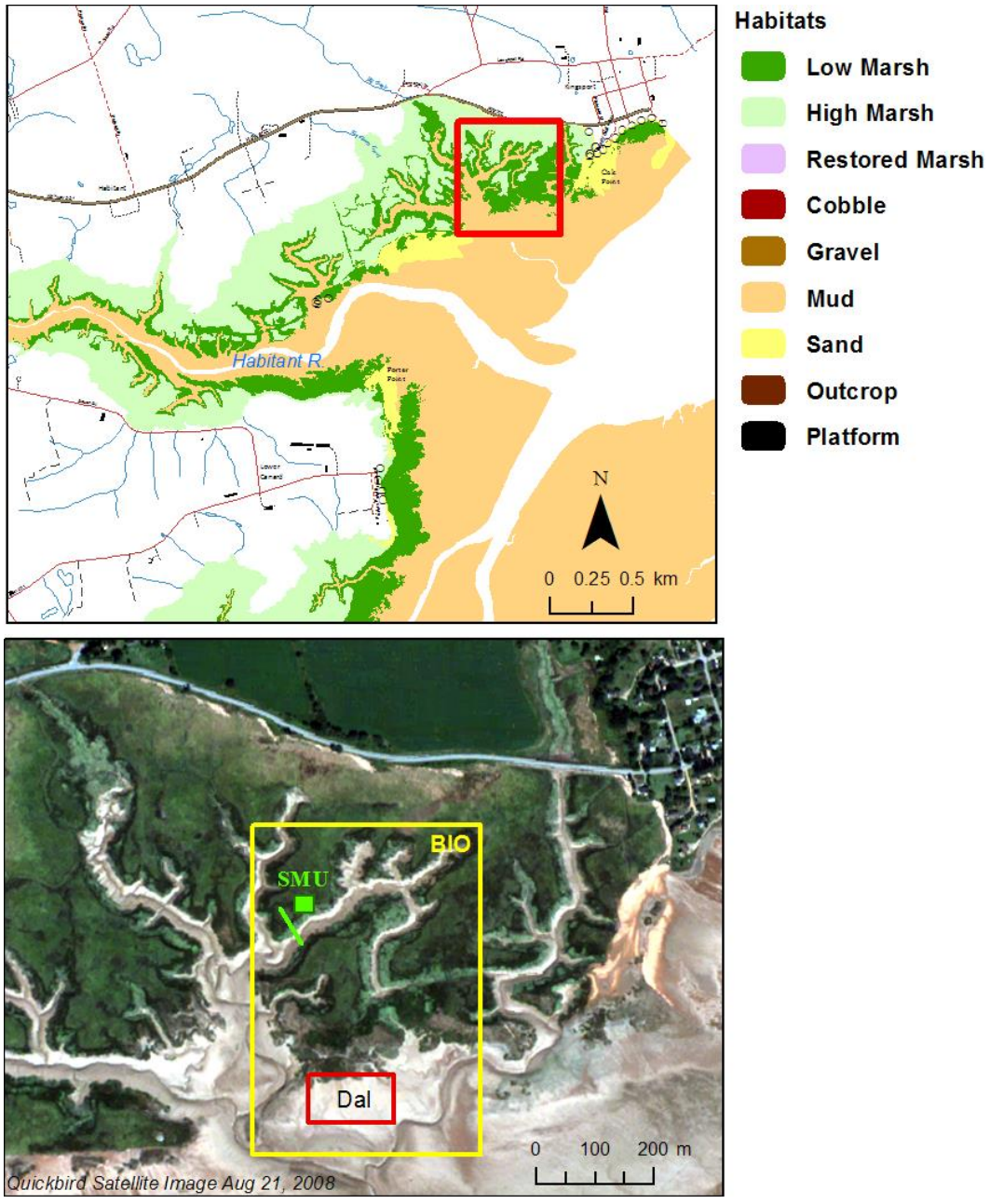

Figure 2: Coastal geomorphology of the Kingsport study site within the Cornwallis Estuary and spatial arrangement of concurrent research being conducted by BIO and Dalhousie University in separate OERA contracts.

The Kingport saltmarsh and mudflat system is located within the Cornwallis Estuary, north of the Town of Wolfville. The marsh itself consists of deeply incised tidal creek networks typical of a salt marsh in a high macro tidal system. The majority of the marsh platform is dominated by high marsh species, particularly *Spartina patens* while lower elevations grading into creeks and mudflats are dominated by the low marsh species *Spartina alterniflora.* The system is exposed to waves from the Cornwallis estuary and once submerged, is influenced by large scale tidal circulation. The Saint Mary's transect is located within a large

2nd order tidal creek that serves as a major conduit of water and suspended material through the marsh system. This transect within the larger sampling grid of the complementary project at BIO and researchers were in regular correspondence to coordinate sampling efforts.

Figure 3: Panoramic photo of study site including sampling tower. Photo taken June 17, 2012.

FIELD and LABORATORY METHODS

A field, lab and modelling campaign was designed to examine the influence of extrinsic (e.g. tidal currents, waves, suspended sediment concentration) and intrinsic (e.g. grain characteristic, vegetation) variables on sedimentation within the intertidal system at multiple spatial and temporal scales. Sampling at multiple resolutions would permit better validation for modelling the potential effects of tidal energy extraction. This section addresses the field and laboratory analyses.

Field Deployments

Seasonal Tidal Cycle Scale

A field sampling program was designed to target tides that would exceed the creek bankfull level and flood the marsh surface. Nine discrete sampling intervals were chosen based on tidal conditions, rate of vegetation growth (e.g. more frequent interval of sampling in summer months) and availability of research personnel. Where possible, the timing of such activities was linked with field sampling campaigns being conducted by Dalhousie University (Hill) and BIO (Law) (Figure 2). The final June 2013 deployment was part of a concurrent spatially intensive sampling effort extending from the Minas passage, to the mudflats fronting the Kingsport marsh into the main tidal creek network involving multiple researchers from Dalhousie University, Bedford Institute of Oceanography and Queen's University.

A Nortek Aquadop shallow water ADCP was deployed near the creek thalweg and sampled in high resolution mode at a rate of 1Hz in 3 cm bins, observing currents over 3 m range, in order to concentrate on processes operating close to the bed. The May 2013 deployment however was conducted using 'normal' mode with 50 cm bins over a 9 m range, allowed the full water column to be sampled. An RBR turbidity, temperature and salinity probe was deployed slightly downstream of the instrument to measure incoming tidal conditions. Three ADVs were deployed along a transect that extended into the high marsh (Figure 4). These sampled at 16Hz in 5 minute bursts every 10 minutes. The first (M3) was deployed on the creek

bank within the *Spartina alterniflora* zone and co-located with the nozzle of the ISCO automated water sampler and optical backscatter sensor (OBS). The second station (M2) was situated within 2 m of the creek bank. M1 was positioned furthest onto the marsh surface approximately 10 m way from station M2 and also co-located with an OBS instrument.

Figure 4: Sampling transect from high marsh (M1) to un-vegetated tidal creek (C4) for deployments from May 2012 to June 2013.

Figure 5: ADV, sediment traps, rising stage sampler and ISCO inlet nozzle at M3 on Sept. 19th, 2012. Note considerable vegetation growth.

Figure 6: Emma Poirier (MSc candidate) downloading data from station M2 ADV on Sept 19, 2012.

The sampling volume for all marsh ADVs was located 15 cm above the marsh surface. Data from all instruments were downloaded regularly in the field at low tide due to the high sampling resolution and limited memory capacity within the instruments (Figure 6). All tides were grouped into seasonal divisions for analysis (Appendix A).

All four stations had 3 co-located surface mounted sediment traps to collect the net amount of sediment that deposited over each tide (Figure 7). In addition, rising stage bottles were deployed at two elevations to measure incoming suspended sediment concentrations (Figure 8). An ISCO automated water sampler was deployed from a tower built on the marsh platform and collected 200 ml water sediment every 15 minutes over the duration of the tidal cycle. The tower was equipped with a heated sampling tube and an insulated enclosed housing for winter deployments. The sampler was powered by a gas generator on site.

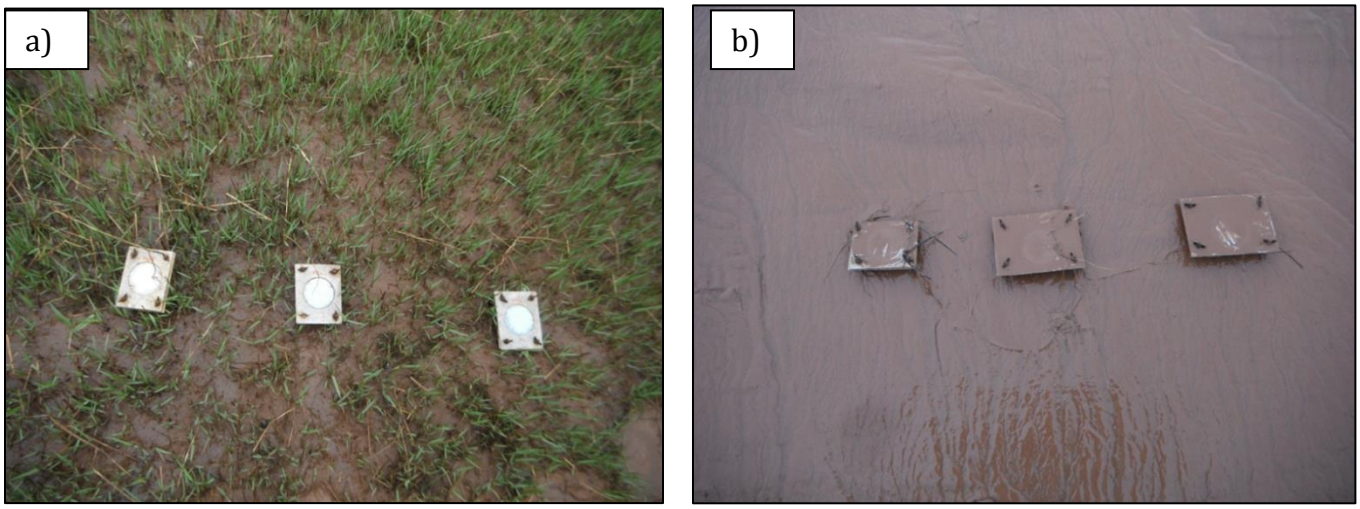

Figure 7: Surface mounted sediment traps deployed at a) M3 prior to the tide on May 25 and b) after the tide at C4 March 27, 2013.

Surface scape samples were collected daily at each station and at the end of each deployment upstream and downstream of the sampling transect. Vegetation biomass was sampled at the end of each deployment at each station to account for differences in the influence of vegetation on flow velocity and sedimentation. Each sample was separated into living and dead biomass. A weather station was established just west of the site and deployed continuously from May 2012-Dec 2013 (Figure 9), however the anemometer was away for repairs during the month of September 2013.

Figure 8: Rising stage bottles deployed at C4 in May 2013.

Figure 9: Weather station deployed on a cliff immediately west of the sampling site

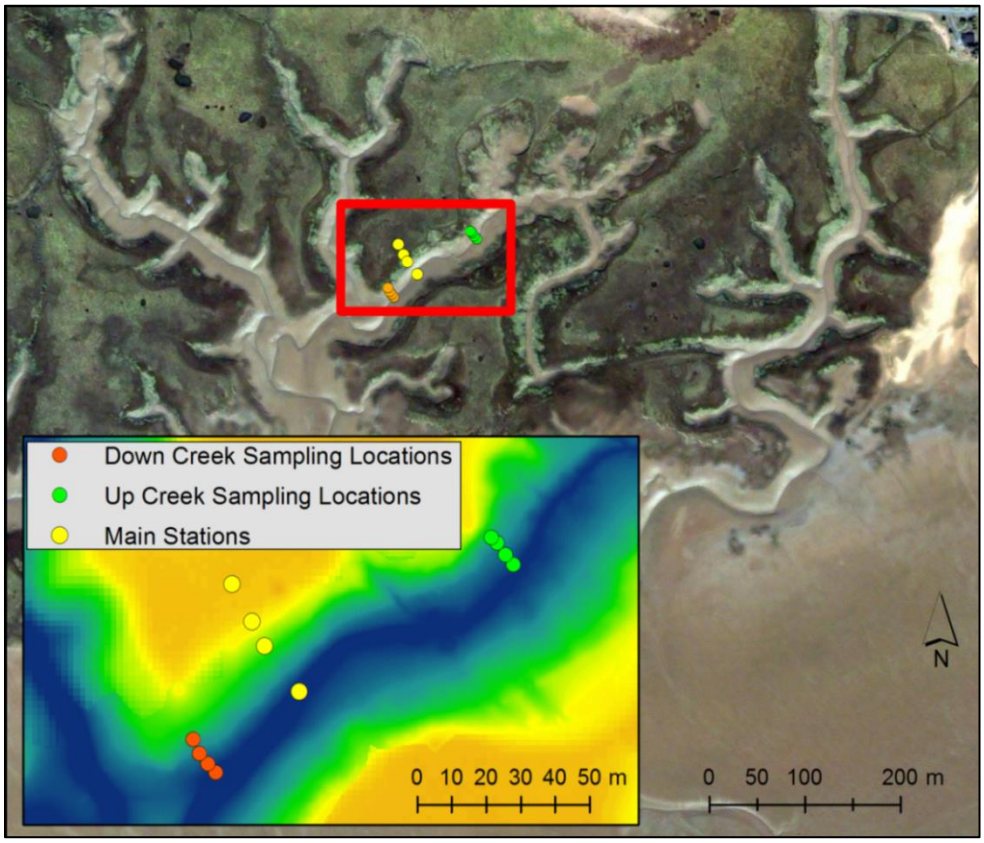

Figure 10: Location of surface scrape samples for detailed grain characteristics.

Seasonal Sediment Budget

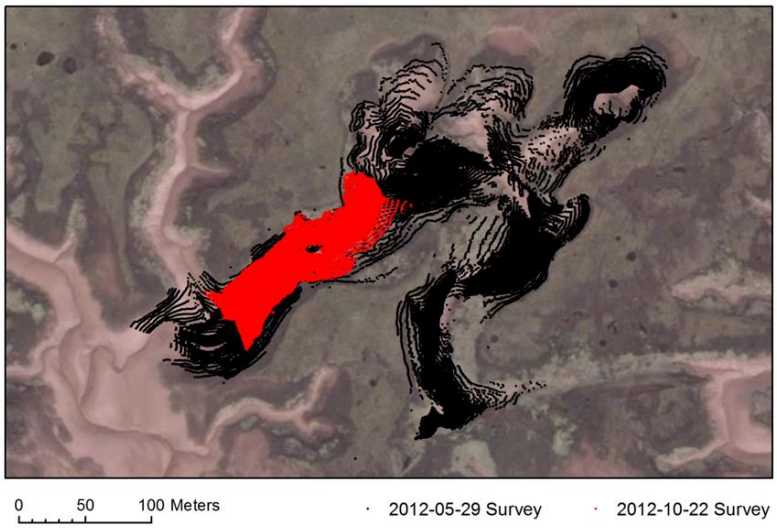

Figure 11: Spatial distribution of sampling for high resolution reflectorless total station measurements. Black indicates full tidal creek network surveys in May 2012 and 2013. Red indicates higher frequency seasonal surveys.

Since we knew from previous work that the hydrodynamics of the creek system are closely tied to the tidal prism moving through it, and is therefore influenced by changes in surface form, it was decided to also conduct a high resolution terrestrial survey seasonally to compliment the aerial LIDAR flown earlier in the spring in collaboration with the team from BIO. A high resolution automated terrestrial survey was conducted, using a Trimble VX total station, of the main creek and feeder creek systems in May 2012. The shallow angle of signal return prevented the fronting mudflat from being surveyed at the same time unfortunately. A total of 78,000 points were collected with cm level accuracy. The total error of the survey was ± 0.08 m. These data were coupled with the earlier larger airborne LIDAR survey and Logan Ashall (MSc candidate Queens) used them to create a high resolution (8 m) Delft3D model bathymetry grid. Additional high resolution terrestrial surveys were conducted using a Trimble VX total station, of the main creek and feeder creek systems in May 29 and 30th 2012, October 22 2012 , Feb 19 2013, May 30-31, 2013 and July 16 2013 (Figure 11). These data were coupled with the earlier larger airborne LIDAR survey and the results integrated into a high resolution mesh in Delft3D, and surface elevation differences were calculated using ArcGIS 10.0. A cross sectional transect of pins were also laid out upstream and downstream of the main sampling area and changes in surface elevation were measured every deployment. However, these pins did not survive winter conditions.

Laboratory Analysis

Sediment trap filters were weighed after air drying for 24-48 hours, to determine the total amount of sediment collected on each paper, on each trap, and at each trap location. Samples were not rinsed prior to weighing, since salinity measured at the mouth of the study creek (with a RBR XR-420 logger) remained relatively constant (~30), and the amount of salt accumulated over individual tidal cycles was minimal relative to the amount of sediment. One filter from each trap was used for grain size analyses. A Kolmogorov-Smirnov test was used to test for normalcy and since the data did not have a normal distribution, a Kruskal-Wallis test was performed. All statistical analyses were performed using Matlab. Suspended sediment concentrations were determined from bottle samples and standard suction filtration methods. Subsamples of the surface scrapes were heated in an oven at 60°C to determine water content and a muffle furnace at 550°C to determine organic matter content.

In order to perform the disaggregated grain size analysis on both deposited and suspended samples, all organic material within the samples needed to be eliminated. Hydrogen peroxide solution at a concentration of 30% was used to dispose of the organic matter. A small amount was placed into 20 ml beakers and 2.5 ml of hydrogen peroxide solution was applied to them. The beakers were placed on hot plates, starting at a temperature of 60°C, and heating up to 80°C. If necessary, an additional 2.5 ml of hydrogen peroxide solution was added. After all of the liquid solution was evaporated, the remaining sediment was only inorganic content.

Disaggregated inorganic grain size (DIGS) analysis was performed on samples of suspended and deposited sediment, using a Beckman-Coulter Multisizer III electroresistance particle counter, following methods described by Milligan and Kranck (1991), Kranck et al. (1996a, 1996b) and Curran et al. (2004). Small subsamples (0.1 - 0.5 g) for DIGS analysis were extracted from field samples of deposited sediment. In most cases, sediment was easily removed from the filter papers. After treatment with hydrogen peroxide (30%) to remove organic materials, subsamples were added to ~10 ml of deionized, reverse osmosis water, and placed in a sonic bath for 1 minute to disaggregate particles. For processing samples of suspended sediment, known volumes of sample laden-water were filtered onto Millipore 8.0 mm SCWP (cellulose acetate) pre-weighed filters using standard gravimetric methods. Millipore filters were selected based on previous studies that recommend these filters due to high retention of particles less than their nominal pore sizes (Sheldon, 1972; Sheldon and Sutcliffe, 1969). Filters were oxidized at <60° C in a low temperature oxygen/plasma asher, to prevent the fusing together of mineral grains while removing the filter. Once subsamples were isolated, they were diluted in a 1% NaCl solution and re-sonicated for 3 minutes using a sapphire-tipped ultrasonic probe, before processing with the Coulter Multisizer III. Both 30 and 200 μm aperture tubes were used in these analyses, the size distributions measured of which were merged to create continuous grain size spectra. In addition, grain size statistics were calculated on the merged grain spectra using GRADISTAT (Blott and Pye, 2001).

Data Processing

Acoustic data recorded by the ADCP were filtered, viewed and interpreted using the standard settings in Storm (ver. 1.14, Nortek). Flow velocity and average signal strength were considered for each tidal cycle. ADCP data collected for this study were not calibrated for quantitative estimates of suspended sediment concentration however can be used as a measure of relative concentrations within a tide. Wave conditions during the sampling periods were investigated using raw pressure signals from the bank ADV, where consistent centimeter-scale waves were observed. Mean current velocity derived from ADV records were estimated through time-averaging over 5-minute measurement bursts. Instantaneous horizontal flow components (x, y) were rotated into down-stream (u) and cross-stream (v) velocities following methods outlined by Roy *et al.* (1996) and Lane *et al.* (1998), and velocity was calculated as $\sqrt{u^2 + v^2}$. Instantaneous turbulent components (u_t, v_t, w_t) were derived using the relationship $u = U + u_t$, and turbulence intensities (i_u, i_v, i_w) were calculated as the root mean square of turbulent components. Turbulent kinetic energy (TKE) was calculated using:

$$TKE = \frac{1}{2}\,\rho\,({u_t}^2 + {v_t}^2 + {w_t}^2) \qquad \text{Equation (1)}$$

where ρ is water density at 20°C (ρ = 1025 kg·m^{-3}) (Neumeier and Amos, 2006; Voulgaris and Meyers, 2004). Mean kinetic energy ($\overline{KE}$) in the tidal creek was estimated with:

$$\overline{KE} = a\,(\,{}^{1}/_{2}\;\rho\,u^{2}\,), \qquad \text{Equation (2)}$$

where a is channel cross-sectional area and u is upstream current velocity (Karsten *et al.*, 2008). Friction velocity (u_*) was computed using the Reynolds stress method (Soulsby, 1983; Kim et al. 2000):

$$u_* = (-\overline{u_t\,w_t})^{1/2}, \qquad \text{Equation (3)}$$

where u_t and w_t are instantaneous components of down-stream and vertical velocity, respectively. Friction velocity can then be applied to calculate bed shear stress (τ_0) (N·m^{-2}):

$$\tau_0 = \rho\,{u_*}^2 \qquad \text{Equation (4)}$$

where z is the measurement elevation above the sea bed, and h is the total local water depth in the channel (Kim et al., 2000; Biron *et al.*, 2004; Voulgaris and Meyers, 2004).
Instantaneous suspended sediment flux in the creek was calculated using:

$$Q_{st(creek)} = Q_{wt} \cdot SSC_t \qquad \text{Equation (5)}$$

(Murphy and Voulgaris 2006), where SSC_t (g·m^{-3}) is the suspended sediment concentration from the RBR in 10 minute means and $Q_{wt}$is the 10 minute mean of water discharge through the channel calculated by:

$$Q_{wt} = \overline{U}_t \cdot A(h_t) \qquad \text{Equation (6)}$$

(Murphy and Voulgaris 2006), where $\overline{U}_t$ (m·s^{-1}) is the 10 minute mean of velocity and $A(h_t)$ is the cross-sectional area calculated using an ArcGIS tool developed by Graham (2012). For the cross-sectional area during the middle portion of the tide where the banks were overtopped, only the area above the channel was considered, and not the area over the marsh surface adjacent to the channel.

Instantaneous suspended sediment flux at the two marsh stations with continuous suspended sediment concentration measurements was calculated using:

$$Q_{st(marsh)} = SSC_t \cdot \overline{U}_t \cdot W \cdot h_t \qquad \text{Equation (7)}$$

(van Proosdij 2001). Q_{st}(g·s^{-1}) is the mean instantaneous sediment flux which was calculated for every 10 minute mean throughout the tidal cycle. SSC_t (g·m^{-3}) is the 10 minute mean of suspended sediment concentration while $\overline{U}_t$ (m·s^{-1}) is the 10 minute mean of velocity. W is a 1m wide portion of water and h_t (m) is the height of the water depth during the 10 minutes. Because suspended sediment concentrations and marsh velocities were point measurements at 10 and 15 cm above the bed, using the water depth in the sediment flux calculations assumes that the conditions are the same throughout the water column.

The total sediment flux over the tidal cycle, Q_s (kg), was then obtained by:

$$Q_s = \sum_{i=1}^{n-1} \frac{y_i + y_{i+1}}{2} (x_{i+1} - x_i) \quad \text{Equation (8)}$$

(van Proosdij 2001) where y_i is the instantaneous suspended flux at time x. Calculating sediment flux is difficult (Coco et al. 2013), but based on the assumption that all sediment on flood tide is input material and all sediment on ebb tide is output material, Q_s is therefore the net mass balance (van Proosdij 2001).

Disaggregated Grain Size (DIGS) distributions of deposited sediment were parameterized using a non-linear, least-squares fit 'inverse floc model', through a semi-automated MATLAB routine developed by Curran et al., (2004) and based on work by Kranck and Milligan (1991) and Kranck et al. (1996a, 1996b). Deposited sediment DIGS distributions are expressed as the log of equivalent weight percent versus log of particle diameters, normalized over the size range (Kranck et al., 1996a, 1996b; Milligan and Kranck 1991). Figure 12 illustrates the components of the Inverse Floc model. The source slope *m* represents the property of the source material; the roll off diameter *dhat* reflects the largest grain size in suspension; the floc limit *df* represents the particle diameter whose flux to the bed as single grains and as flocs is equal; finally, the floc fraction *Kf* represents the mass fraction of floc-deposited mud to the bed. The model assumes a single source of material and no re-suspension (Curran et al., 2004). Suspended samples are expressed using log of concentration in parts per million (PPM) (Law et al., 2008).

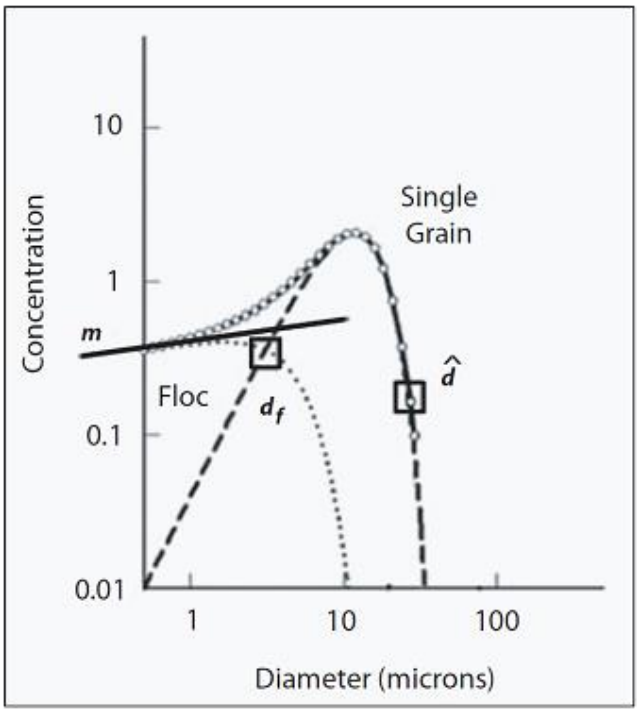

Figure 12: Idealized DIGS distribution (solid line) showing concentration versus diameter on log-log axes. The floc-settled (dotted line) and single-grain (dashed line) components are determined by the inverse floc model. Graphical locations of model parameters of model parameters (d_f, $\hat{d}$, m) are shown. Modified from deGelleke et al. (2013).

RESULTS and DISCUSSION

Sixty-two tidal cycles were sampled between May 2012 and June 2013 over a range of environmental, vegetative and tidal conditions. All instruments (including sediment traps and ISCO sampler) worked perfectly over 34 tides and sediment trap data from 11 tides have some missing data due to rain or unsafe field conditions (Appendix A). Data were collected over the widest range of tide elevations to date (CHS 42.0 to 49.3 ft), representing maximum water depths of 6.3 to 8.3 m at the ADCP (Appendix A). The March deployment provided exemplary results, with every tide having complete data sets. Both May and June saw frequent rainfall which resulted in five days' worth of sediment deposition data being under rain conditions (Appendix A). During the passage of post tropical storm Andrea on June 8th, 62.4 mm of rain fell within a 12 hr period, the majority occurring on the rising tide mid-morning resulting in significant volumes of water passing through the creek channels (Figure 13).

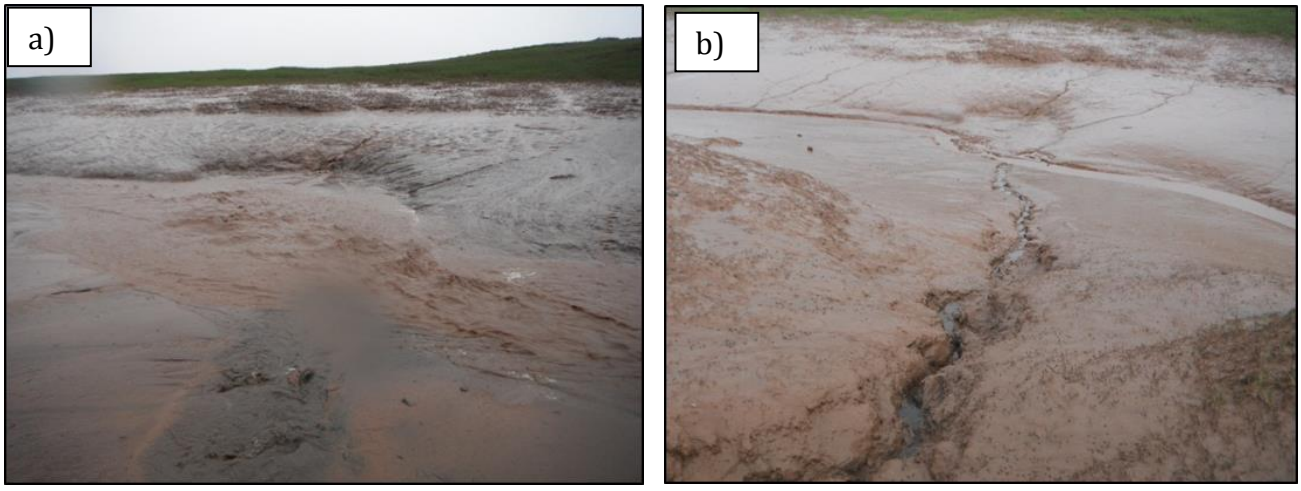

Figure 13: Small tributary creek thalweg into main channel on low tide on a) June 8, 2013 during Post Tropical Storm Andrea and b) June 10, 2013. Note fluid sediment and new slump.

Seasonal Variations: Tidal Cycle Scale

Sediment Deposition

Spatially, sediment deposition was much higher in the creek thalweg than on the marsh, as can be seen in Figure 14 , with a mean value of 66 $g \cdot m^{-2}$. Including all the deployments, the creek thalweg had on average 3.5 more deposition than the mean of the three marsh stations. The marsh bank, the only station on the low marsh, consistently had an intermediate level of sediment deposition, with a mean of 28.7 $g \cdot m^{-2}$. The marsh edge and marsh surface, both stations being on the high marsh, experience very similar amounts of deposition, with mean values of 13.7 $g \cdot m^{-2}$ and 13.6 $g \cdot m^{-2}$ respectively. After a Kolmogorov-Smirnov test was run on the depositional data and showed the data to be non-normal, Kruskal-Wallis tests were run to determine statistical significance between stations and between seasons. These tests resulted in the creek thalweg and the marsh bank to both be independently statistically significant ($p<0.05$) from all other

stations while the marsh surface and the marsh edge were not statistically significant from each other. The creek station also displayed the greatest variability and range of values between deployments (Figure 15).

To determine seasonal variability in deposition, the nine field deployments were divided into three categories. The winter category included November, January and March, the spring category included May 2012, May 2013 and June, and the summer category included July, August and September. At all stations, the winter group experienced more deposition, and this increase in winter was higher at the marsh bank and creek thalweg stations (Figure 16).

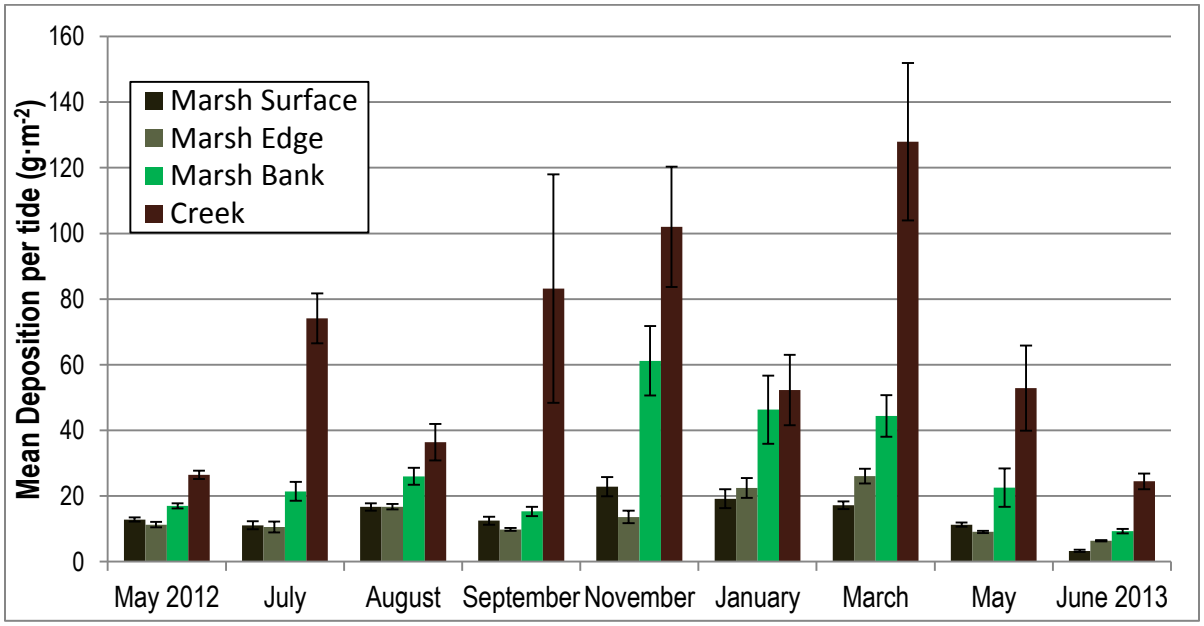

Figure 14: Mean sediment deposition per deployment from M1 (marsh surface) to C4 (creek). Error bars represent standard error.

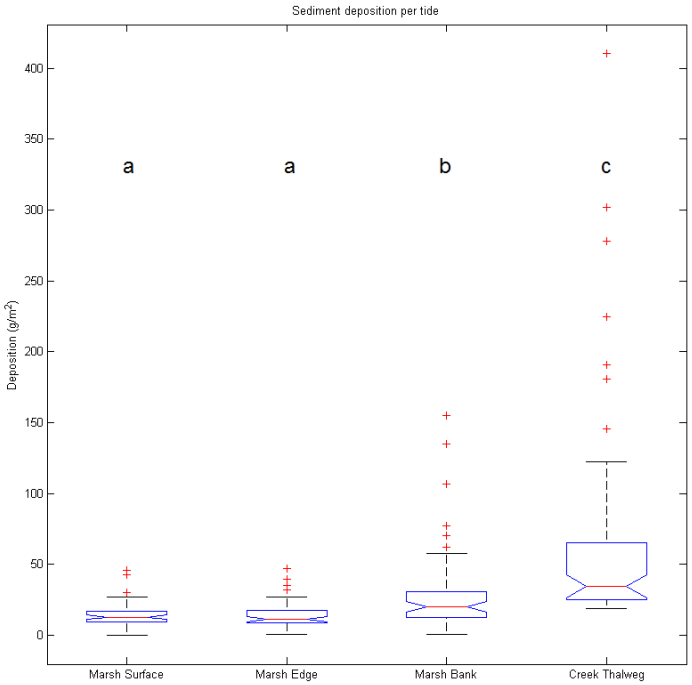

Figure 15: Box plot of mean sediment deposition from May 2012 to June 2013. Letters that are different represent statistically significant differences between them at the 95% confidence interval. The creek thalweg exhibits statistically significantly higher deposition between sites however also displays the greatest seasonal variability.

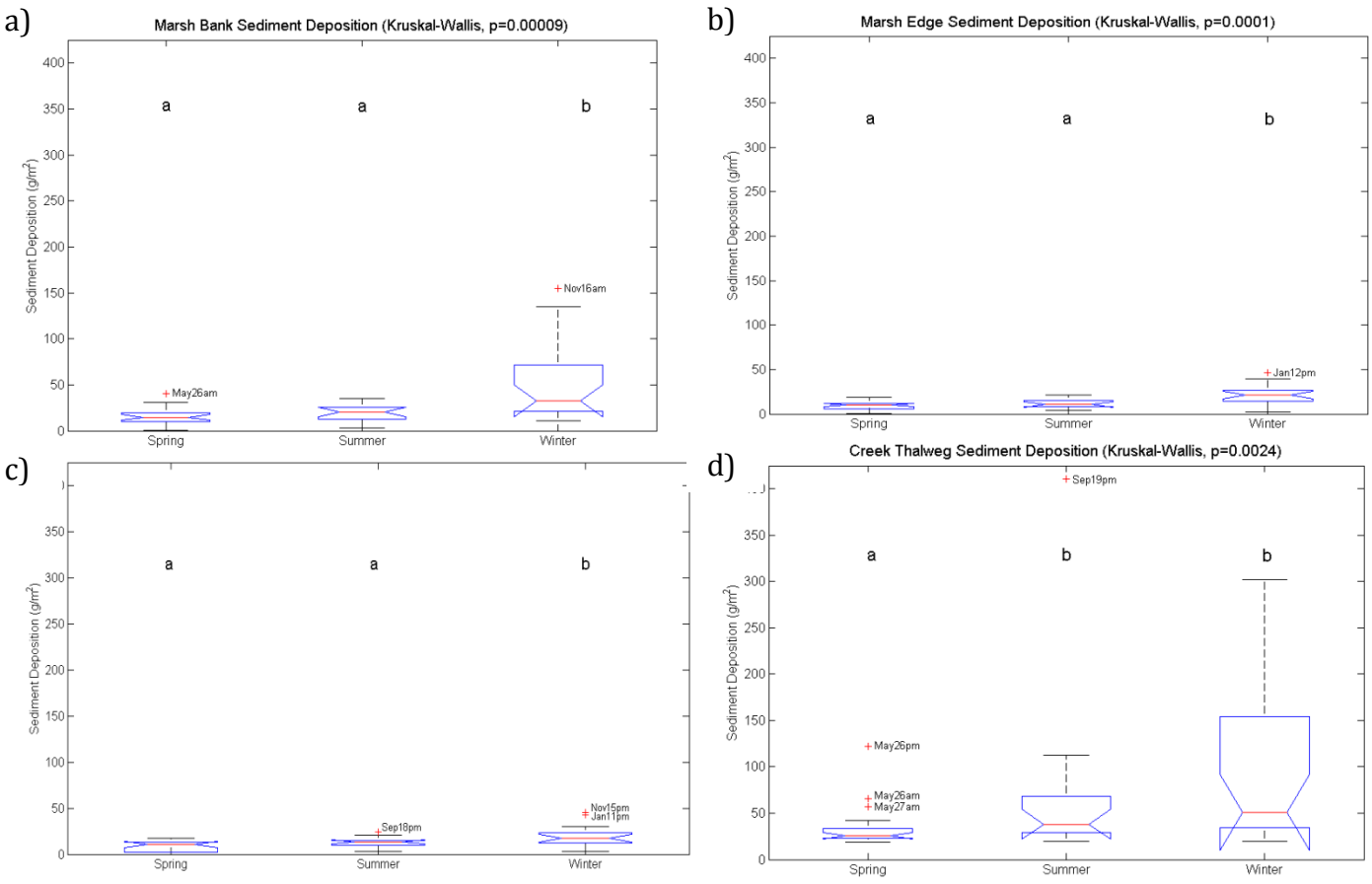

Figure 16: Seasonal variation in mean sediment deposition at a) M1 marsh surface, b) M2 marsh edge, c) M3 vegetated tidal creek bank and d) creek thalweg.

Hydrodynamics and Sediment Transport

The mean horizontal velocities on the marsh (Figure 17) saw a pattern of flood dominance at the marsh bank. This flood dominance was strongest during certain months, such as November, January, March and May 2013. The flood dominance pattern was diminished as the measurements were further in the marsh. At the marsh surface, certain tides change to a slight ebb dominance. The values for the marsh edge and the marsh surface are mostly in the range of 1 – 3 $cm \cdot s^{-1}$, with the values on the marsh bank spanning further out of that range (up to 9 $cm \cdot s^{-1}$) (Figure 17). The slowest velocities are seen on the marsh bank in the deployment of November, which led to November having the highest sediment deposition values on the marsh bank (Figure 14).

Suspended Sediment Dynamics

An increase in incoming suspended sediment concentration in the creek in the cold temperature deployments, November, January and March, which were categorized in the winter group, led to an increase in sediment deposition at the creek thalweg and on the marsh bank (
Figure 16). When the initial suspended sediment concentration is high, it leads to more rapid deposition because of increased aggregation between particles driving sediment to the bottom (Milligan et al. 2007). Because of the rapid settling in the channel and on the marsh bank, suspended sediment concentrations were reduced to typical levels when the water reached the marsh edge and subsequently the marsh surface. As this high winter incoming concentration is present, the incoming spring concentrations, although still significantly lower than the winter, were higher than the summer values. This spring concentration distribution is driven up by the tides of the May 2013 deployment, caused by notably higher flood velocities. In terms of incoming suspended sediment concentration from the rising stage bottles, the creek thalweg was the only station for which the winter was significantly higher than both the spring and summer (Figure 18).

Spatially, suspended sediment concentration followed the same pattern as did sediment deposition, being highest at the creek thalweg, intermediate at the marsh bank and lowest at both the marsh edge and the marsh surface. Concentrations rarely exceeded 100 $mg \cdot l^{-1}$ on the marsh surface and marsh bank with the exception of August and September (~300 $mg \cdot l^{-1}$) at the marsh bank (Figure 19). Tidal cycle patterns of suspended sediment concentration were markedly different in the creek than they were on the marsh. In the creek, clear flood and ebb pulses of concentration are evident (up to 2500 $mg \cdot l^{-1}$), with a more uniform decrease during the middle of the tide (less than 300 $mg \cdot l^{-1}$). The November and January deployments had the most consistently high concentrations close to 500 $mg \cdot l^{-1}$ after the tidal bore (Figure 19). On the marsh, such flood and ebb pulses are not as prominent.

The marsh bank experienced high suspended sediment concentrations in August and September (Figure 19). The marsh bank, located on the low marsh, is the only station dominated by *Spartina alterniflora.* With the alive biomass of *Spartina alterniflora* at its highest during August and September (Figure 21), this may be causing a congregation of suspended sediment in the area, as this plant has been studied to retain sediment on its stems (Yang et al. 2008) and a study by Leonard and Luther (1995) found velocities in a *Spartina alterniflora* canopy to be at their lowest between 7 cm and 12 cm above the bed, which may explain the high concentrations but lack in increased deposition.

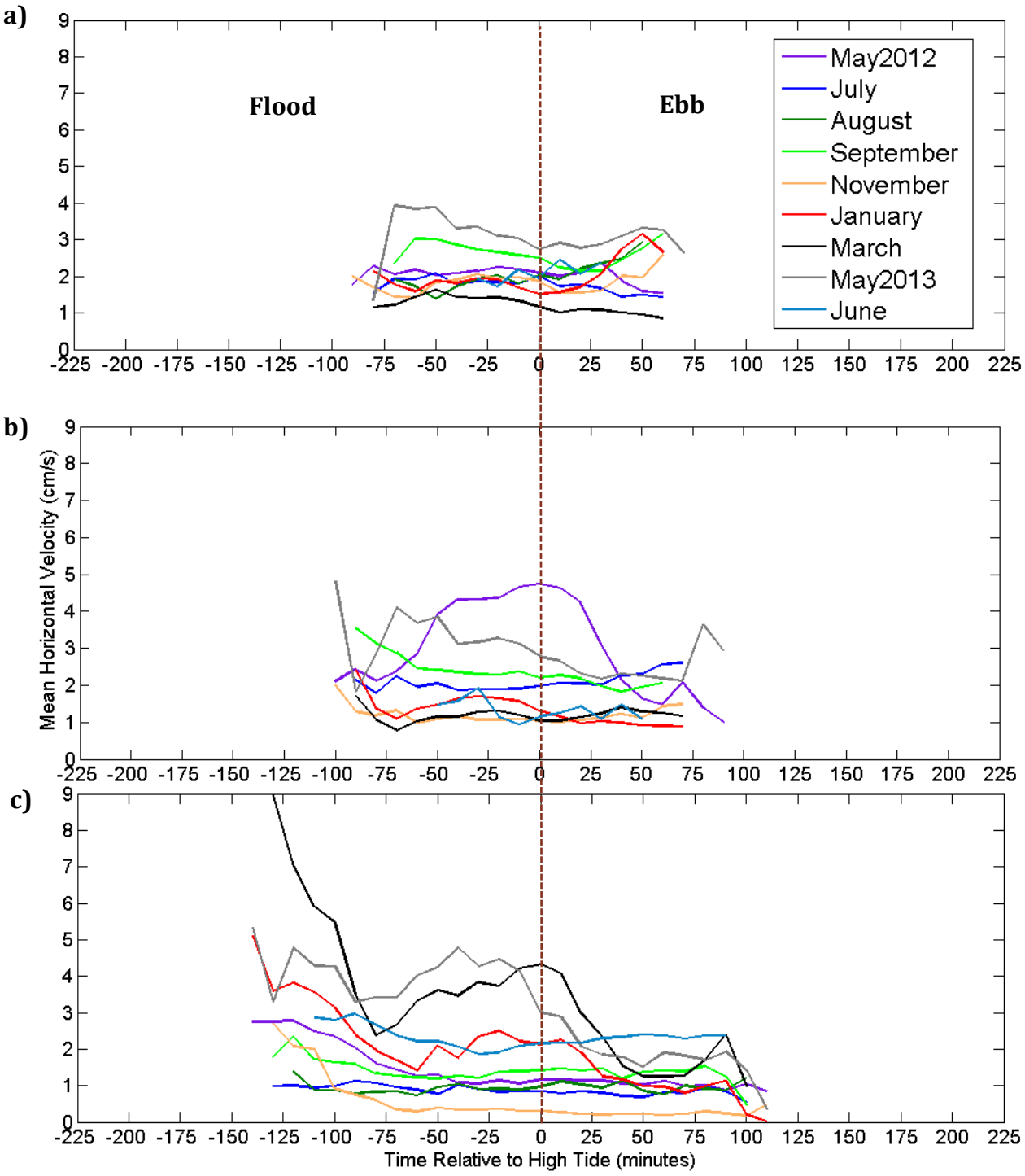

Figure 17: Time series of mean horizontal velocities per deployment at the a) marsh surface, b) marsh edge and c) marsh bank.

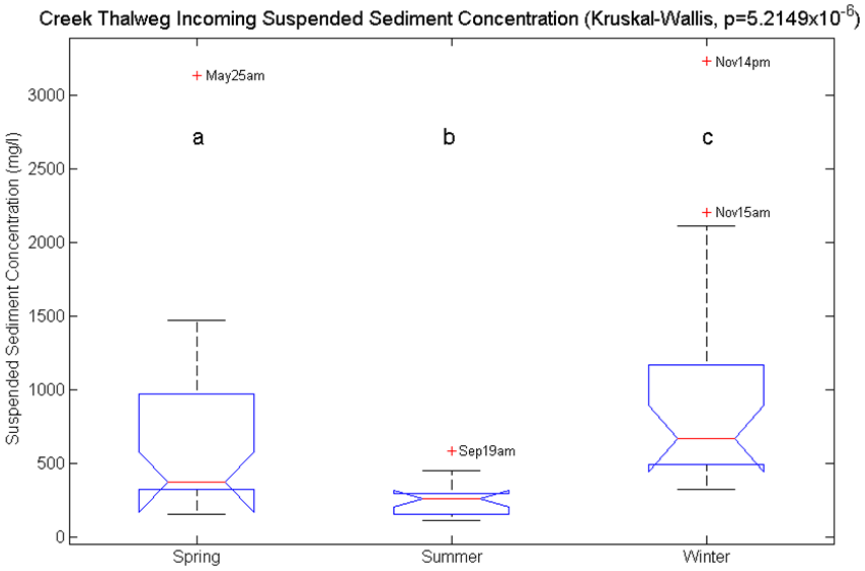

Figure 18: Incoming suspended sediment concentration at the creek thalweg from rising stage bottles 20 cm above the bed. Kruskal-Wallis tests show all three seasons to be statistically significant ($p<0.05$) from each other.

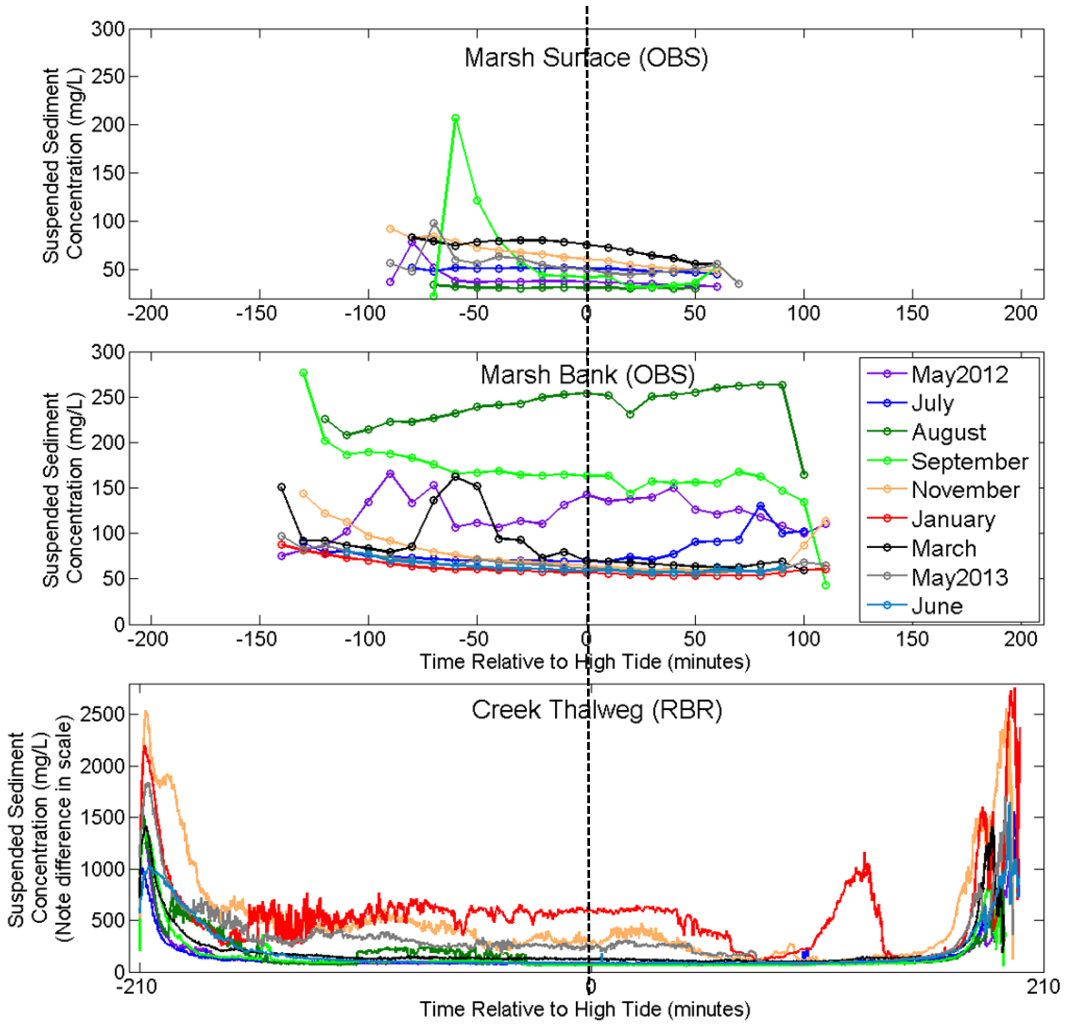

Figure 19: Time series of suspended sediment concentration throughout the tide from the OBS for the marsh surface and the marsh bank and from the RBR at the creek thalweg.

Variation in Vegetation and Surface Conditions

Vegetation characteristics (e.g. biomass) vary greatly throughout the year, particularly throughout the typical growing season (May to Sept.). These changes will lead to varying surface roughness and influence both hydrodynamics and sediment deposition. In addition, dead versus alive biomass will exert different influences and this influence is limited during the winter months as material is generally frozen to the bed or beneath a layer of ice or snow. The marsh surface and marsh edge are dominated by the high marsh species *Spartina patens* while the marsh bank is dominated by *Spartina alterniflora.* Surface roughness is also influenced by the presence and absence of ice (**Error! Reference source not found.**).

Figure 20: Example of seasonal changes in vegetative cover and channel form between November, 2012 and January 2013.

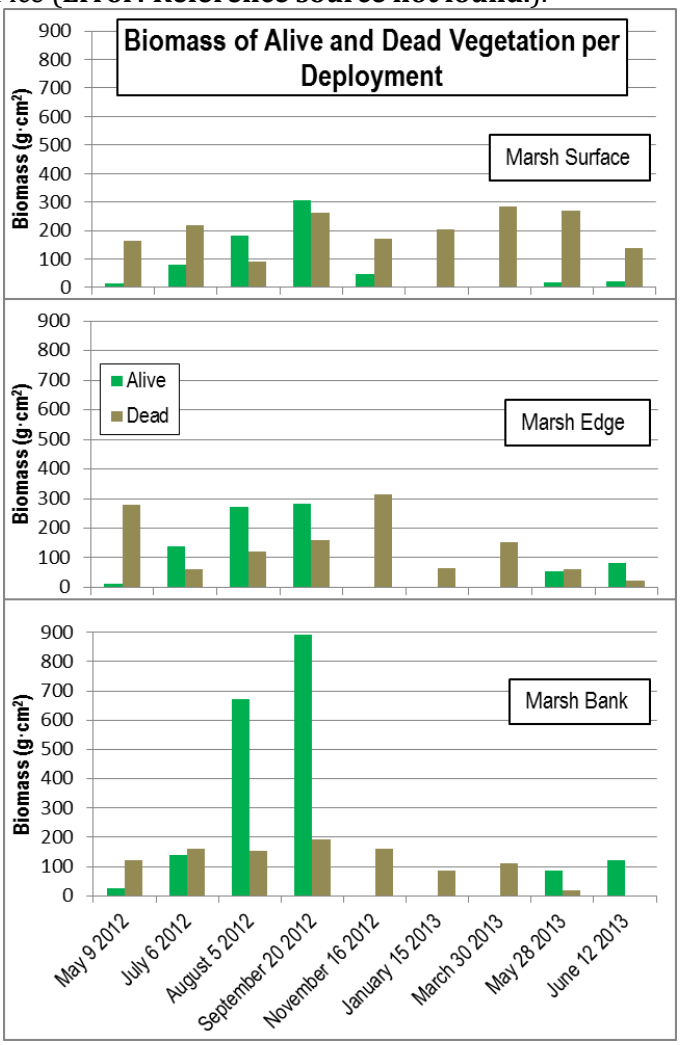

Figure 21: Quantification of live versus dead vegetation biomass at marsh stations from May 2012 to June 2013.

Live biomass is present at all stations from May to September as expected. Peak biomass occurs in August and September, ranging from approximately 300 g·cm^{-2} at both the marsh edge and marsh surface to up to almost three times as much on the marsh bank (Figure 21). This may potentially explain the lower velocities on the marsh bank in July, August and September. The remaining months show limited differences between stations. In general, more dead biomass remains on the marsh surface (M1) than any other station (Figure 21). The most significant changes in surface roughness occur during the winter

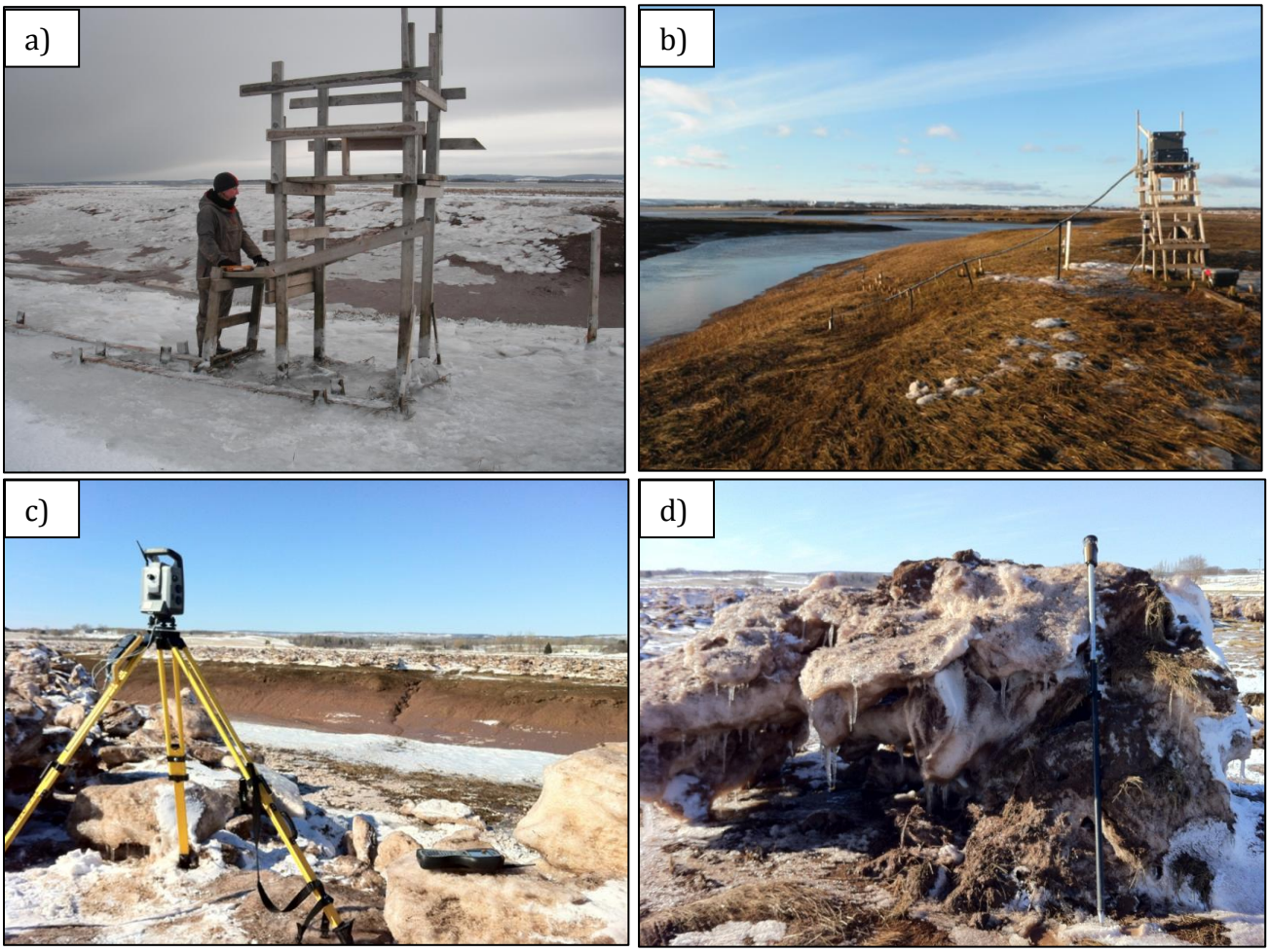

Figure 22: Rapid changes in surface conditions during the winter season. Conditions on a) Jan 7, 2013; b) Jan 12, 2013; c) Feb 19, 2013; d) Large, sediment laden ice blocks are periodically present and some will ground in the high marsh. 1 m hiking pole for scale.

months. In addition, surface conditions can change dramatically within a few short days with the appearance and disappearance of ice. This is most noticeable on the marsh surface (Figure 22).

In addition, periods of milder temperatures during the winter itself or during the spring, will allow for large deposits of sediment to be deposited in mounds on the marsh surface or upper creek bank. Many of these were observed during the January deployment. Visual observation also suggests that these ice deposits will also import coarse material, including gravel and cobble into the marsh system.

Figure 23: Sediment deposited by melting ice block observed near station M1 on Jan 13, 2013.

Sediment Characteristics

Surface sediment followed a spatial pattern of being coarsest in the creek with a mean value of 11.9 µm and consistently fining with increasing distance from creek with mean grain sizes of 9.6 µm, 9.3 µm and 9.1 µm at the marsh bank, edge and surface respectively. The sediments which were most dominated by grains in floc form were at the marsh bank with 83% of surface sediments in floc form (Figure 24). The marsh bank is an ideal location for sediment to flocculate because the single grains have already settled out at lower elevation and the concentration is still high therefore presenting ample opportunity for sediment to form flocs (Curran et al. 2004). These single grains would have settled in the channel, which is the station with the lowest floc fraction value of 76%. As the water reaches the marsh edge and the concentration has decreased from the marsh bank, floc fraction subsequently decreases to 82% and then 79% at the marsh surface. After the single grains have settled out, there is a connected decrease in grain size, relative amount of sediment in floc form and consequently deposition. The samples from the bank up creek and down creek of the main stations (Figure 25) show two things. Firstly, there is a fining of sediments further up creek. Secondly, there is a fining of sediments with increasing elevation.

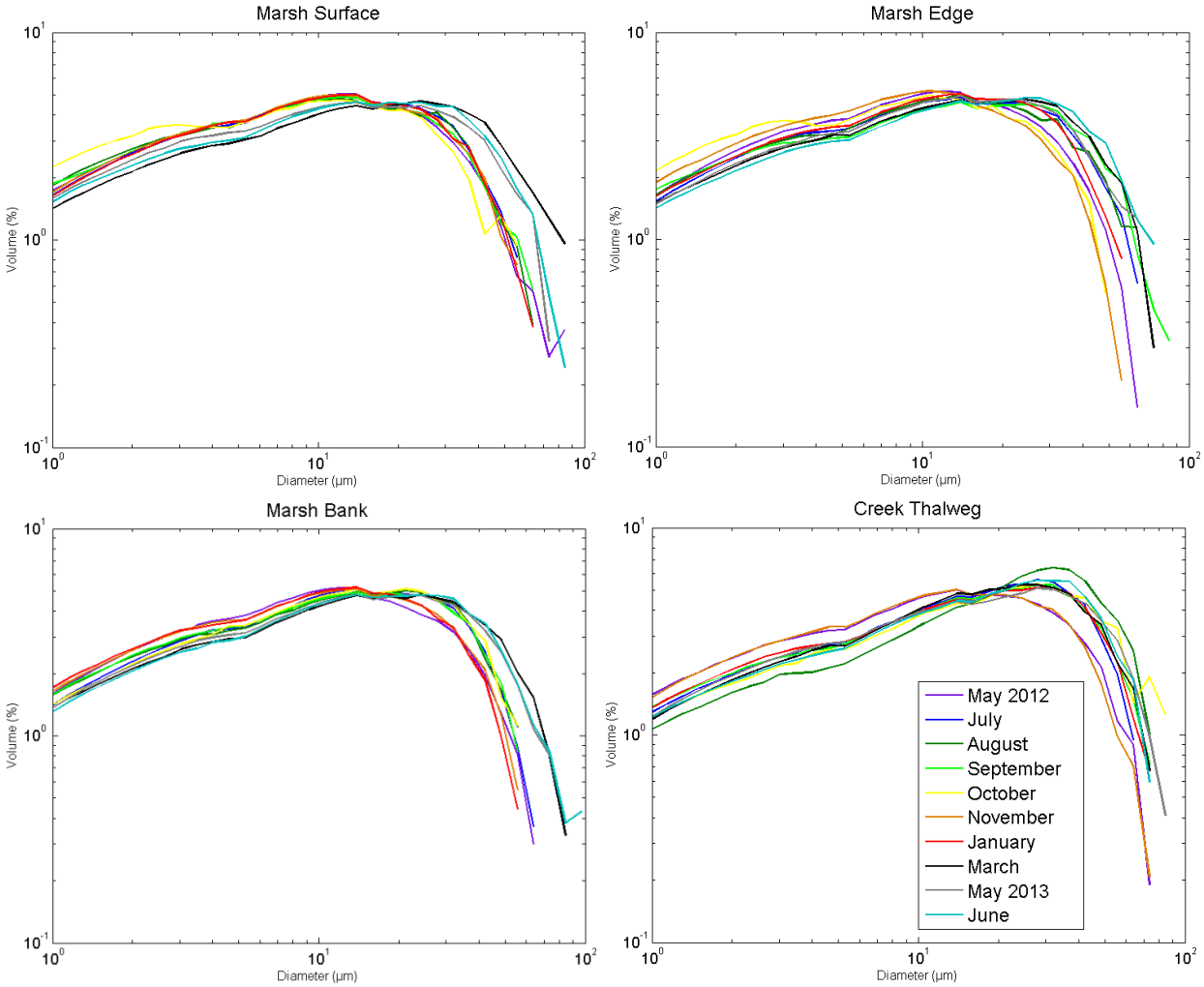

Figure 24: Mean disaggregated inorganic grain size of the daily surface scrapes per deployment at each station.

Sediment characteristics of the material deposited on the traps were the most variable amongst all grain size datasets (Figure 26). Although the majority of the tides do seem to have very similar grain sizes consistent between tides, certain tides did show a grain size distribution which is relatively coarser than the typical tide. Examples of this scenario occur during May25am, May26pm, Sep19am and Sep19pm tides. When plotted as their representative weights of the sediment collected on the traps (Figure 26), these particular distributions that seemed coarse now show rather an absence of fine sediments. This may suggest fines were preferentially removed from the traps on the ebb, likely associated with the small surface waves observed during those tides.

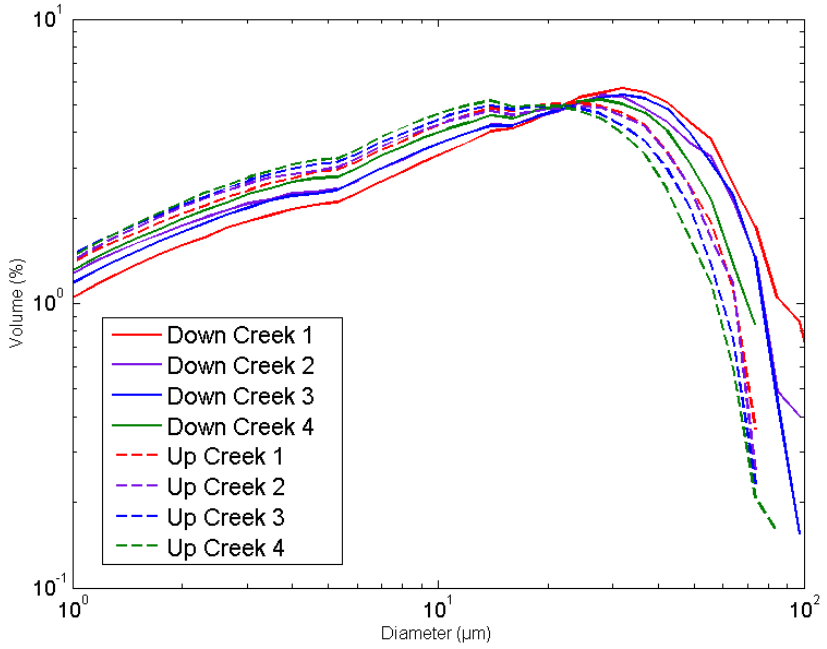

Figure 25: Mean disaggregated inorganic grain size of scrape samples on the bank at the down creek and up creek transects including samples of all deployments, plotted per sampling location.

As with the surface samples, the sediment from the suspended samples also shows a fining of sediment from the channel to the marsh surface (Figure 26). Grain size throughout the tidal cycle did not vary to a great degree (Appendix D), but there were some differences in grain size between tides. In particular, tides from the June deployment were markedly finer than any other tides in the samples from the ISCO water sampler on the marsh bank (Figure 27). The rising stage bottles support the observations of minimal variation in grain spectra between marsh stations but generally coarser in the tidal creek (Figure 28).

Examination of grain size concentrations of one tidal cycle for each deployment collected from the ISCO water sampler at the marsh bank every 15 minutes illustrates the general consistency in sample composition at each time interval (
Figure 29). In most cases there is an overall decrease in concentration with time.

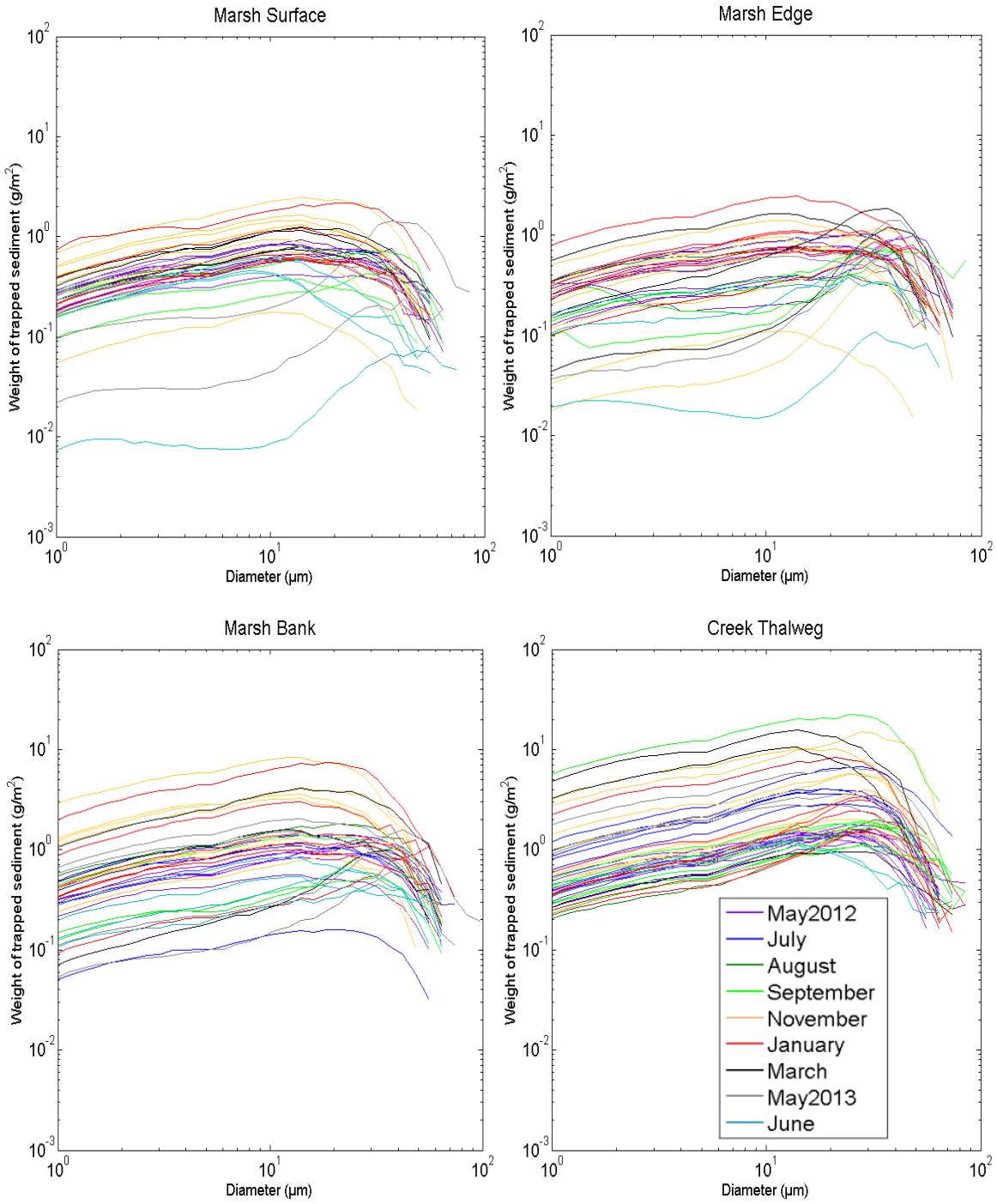

Figure 26: Disaggregated inorganic grain size of sediment deposited on traps represented by the weight of the sediment trapped, at each station. Each distribution is an individual tidal cycle.

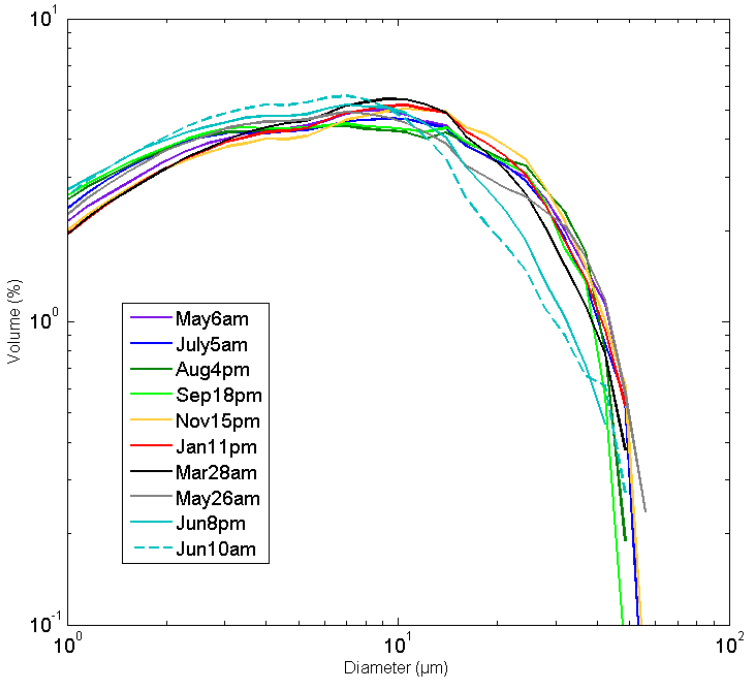

Figure 27: Mean disaggregated inorganic grain size per tide of the suspended sediment captured by the ISCO water sampler at the marsh bank.

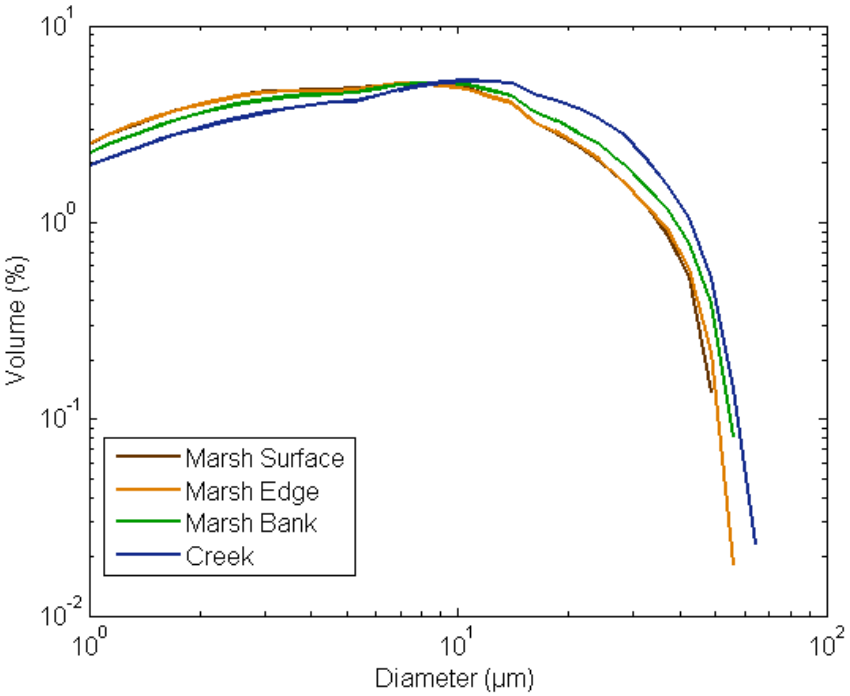

Figure 28: Mean disaggregated inorganic grain size per station of the suspended sediment from the rising stage bottles at 20 cm above the bed.

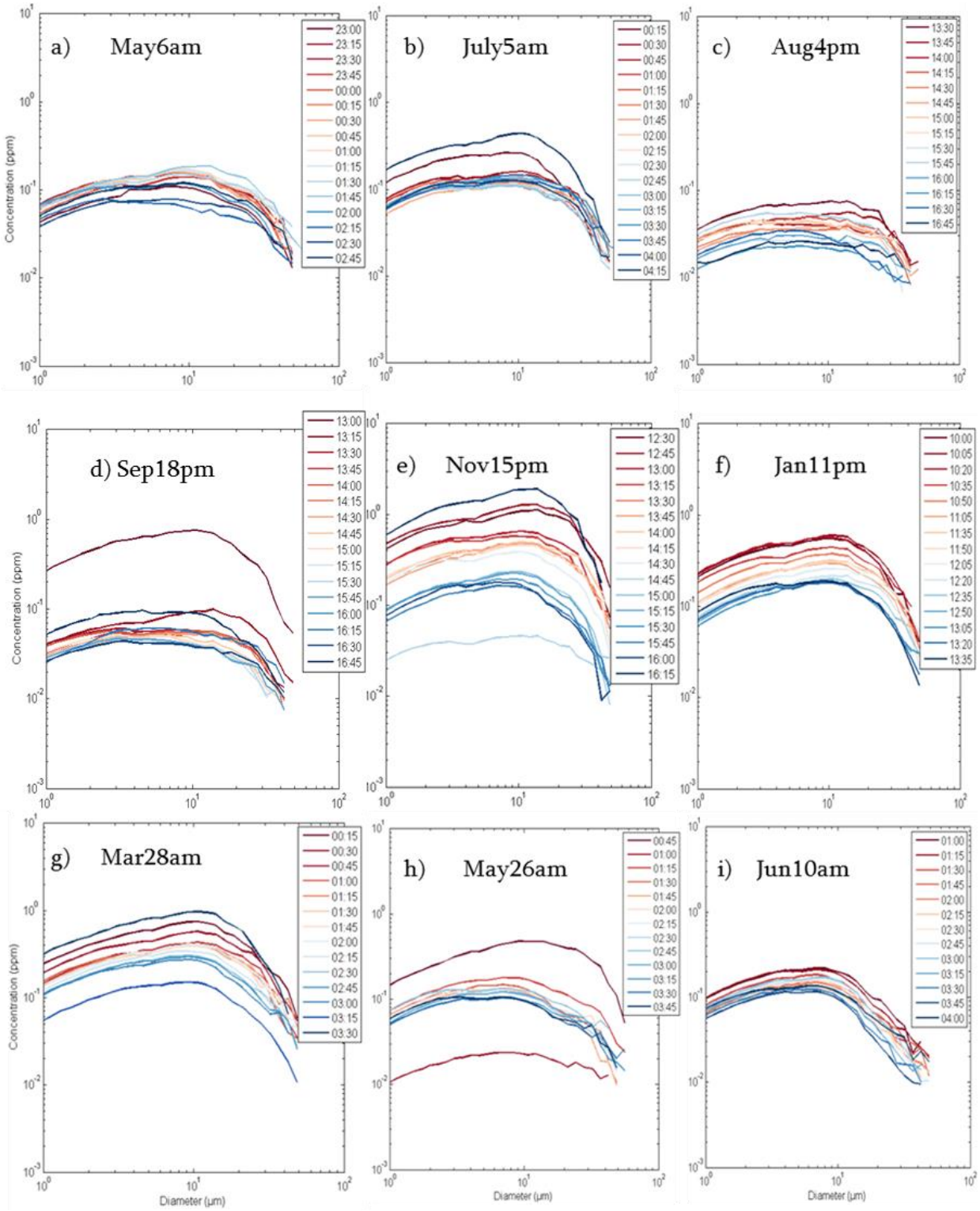

Figure 29: Grain size concentrations (ppm) of one tidal cycle for each deployment including samples at 15 minute intervals from the ISCO water sampler at the marsh bank.

Seasonal Variations: Sediment Budget

With the reflectorless total station surveys, surface elevation change maps were generated for each time interval between surveys (Figure 30). From these surveys, the period with the largest net lowering of surface elevation is October 2012 to February 2013. The associated wind rose shows the strongest winds as well as winds aligned into the channel, creating the possibility for potential wave re-suspension. The period with the largest net positive elevation change is February to May 2013.

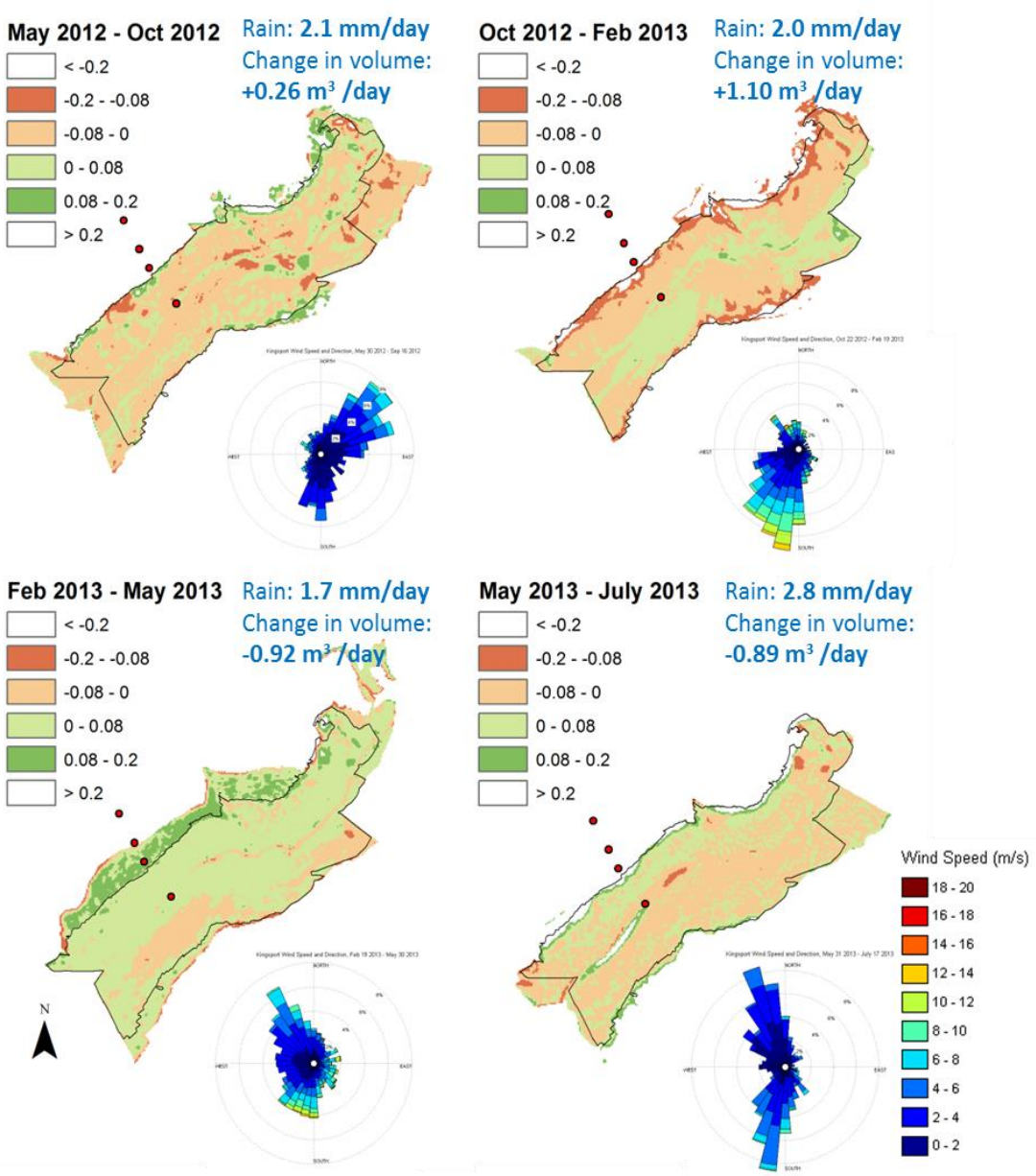

Figure 30: Change in elevation in meters between different surveying periods. The wind roses are representing the corresponding dates included in the change maps. The black outline represents the area that is common between all surveys and was used for the volume calculations. The noted change in volume represents the change in volume of water fitting in the channel below bankfull level.

A rough mass balance of sediment budget, suspended sediment flux in the channel was calculated using $Q_{st} = Q_{wt} \cdot SSC_t$ where $Q_{wt} = \bar{U}_t \cdot A(h_t)$ (Murphy and Voulgaris 2006). $A(h_t)$ is the cross sectional area occupied by the water, calculated with an ArcGIS hydraulic toolbox developed by Graham (2012). Flux values in November and January are by far the highest, with the March values also being among the highest (Figure 31). Integrated over the tidal cycle (Equation 8) and taking the difference between the flood and ebb, a rough mass balance of imported sediment can be calculated (Table 1). This method introduces two assumptions. Firstly, the suspended sediment concentration values are taken at 10 cm above the bed and are assumed to be the same throughout the channel cross section. Secondly, the flood is assumed to be an import period and ebb to be an export period. Figure 31 and Table 1 should therefore only be taken as estimates as kg values are overestimated but patterns are useful. This calculation of potential imported material leads to the period of October to February having the most sediment coming in the channel and being available for deposition. This was also period in Figure 31 with the largest export in material, meaning that although there is an abundance of sediment available, there is ample movement of this sediment during this period. The high import value for October to February in Table 1 can be explained by the tides for which field data were collected not having the same wind conditions as had the majority of tides between these two survey dates.

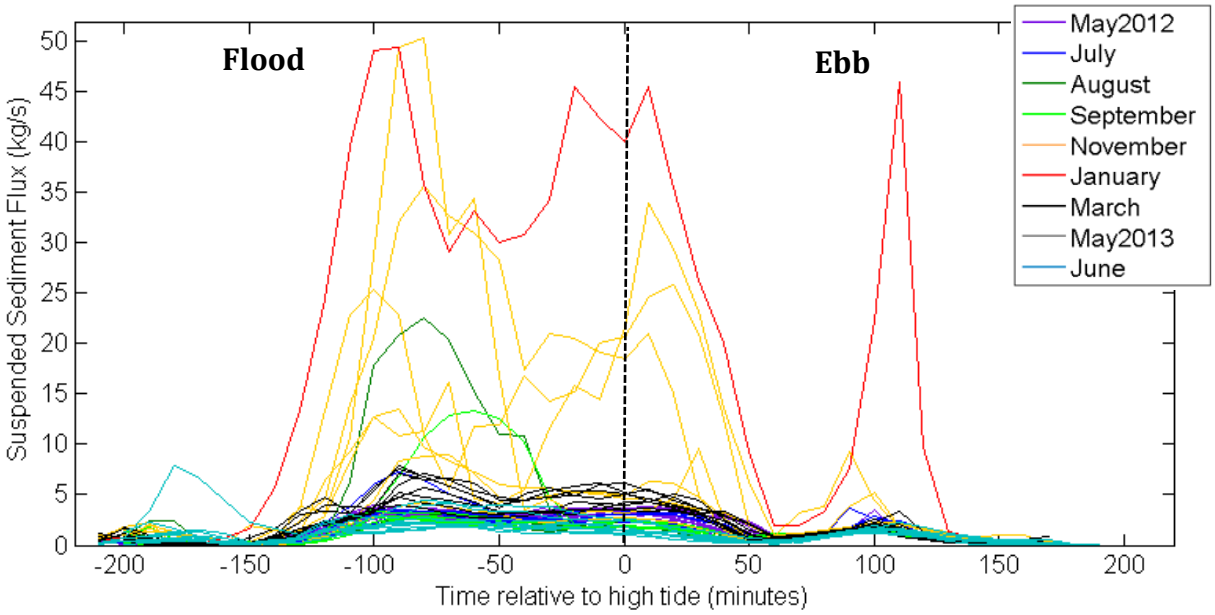

Figure 31: Suspended Sediment Flux in the channel per tide.

Interval (between surveys)	Mean residual flux per tide (kg)	Days	Total import (kg) based on tides collected	Surface area at bankfull (m^2)	Imported sediment covering channel banks ($kg \cdot m^{-2}$)	Estimated depth of sediment layer (cm)
May 2012 to Oct 2012	16882	145	4895763	76124	64	2.3
Oct 2012 to Feb 2013	76091	120	18261888		240	8.6
Feb 2013 to May 2013	21404	100	4280764		56	2.0
May 2013 to July 2013	14259	47	1340356		18	0.6

Table 1: Rough mass balance of imported sediment extrapolated to cover channel banks. Bankfull elevation 5.75 m CGVD28. Estimated depth of sediment layer deposited based on particle density of silt of 2.798 $g \cdot cm^3$.

Time interval used for GIS budget determination	Estimated depth of sediment layer (cm)
May 2012 to Oct 2012	-0.78
Oct 2012 to Feb 2013	-2.74
Feb 2013 to May 2013	1.91
May 2013 to July 2013	0.87

Table 2: Estimated depth of sediment layer based on GIS budget analysis. Surface area for polygon used = 4812 m² and volume differences illustrated in Figure 30 used for analysis. A negative sign indicates surface lowering.

Comparison of the estimated depth of sediment deposited within the tidal creek shows marked differences in pattern and magnitude (Table 1 and Table 2). This however is not surprising as it reflects differences in processes and measurement technique. The estimate based on sediment flux results in overall net increases in surface elevation since it is based on an extrapolation of conditions during single tides. The GIS survey budget calculation represents a net surface that includes a wider range in natural variability, including rainfall. However, it is also susceptible to the date of the survey and meteorological conditions immediately preceding it. Interestingly the Feb-May and May-July, 2013 estimations are quite similar between techniques (Table 1, Table 2). One might infer that conditions in late fall and early winter are the most variable and exhibit the most precipitation events. Exceptions however may occur during the passage of strong post tropical storms or hurricanes.

Figure 32 illustrates the impact of heavy rainfall during the rising tide on suspended sediment concentration measured at the ADCP during post-tropical storm Andrea on June 8th within the tidal creek. Two days later, signals are back to base level (Figure 33).

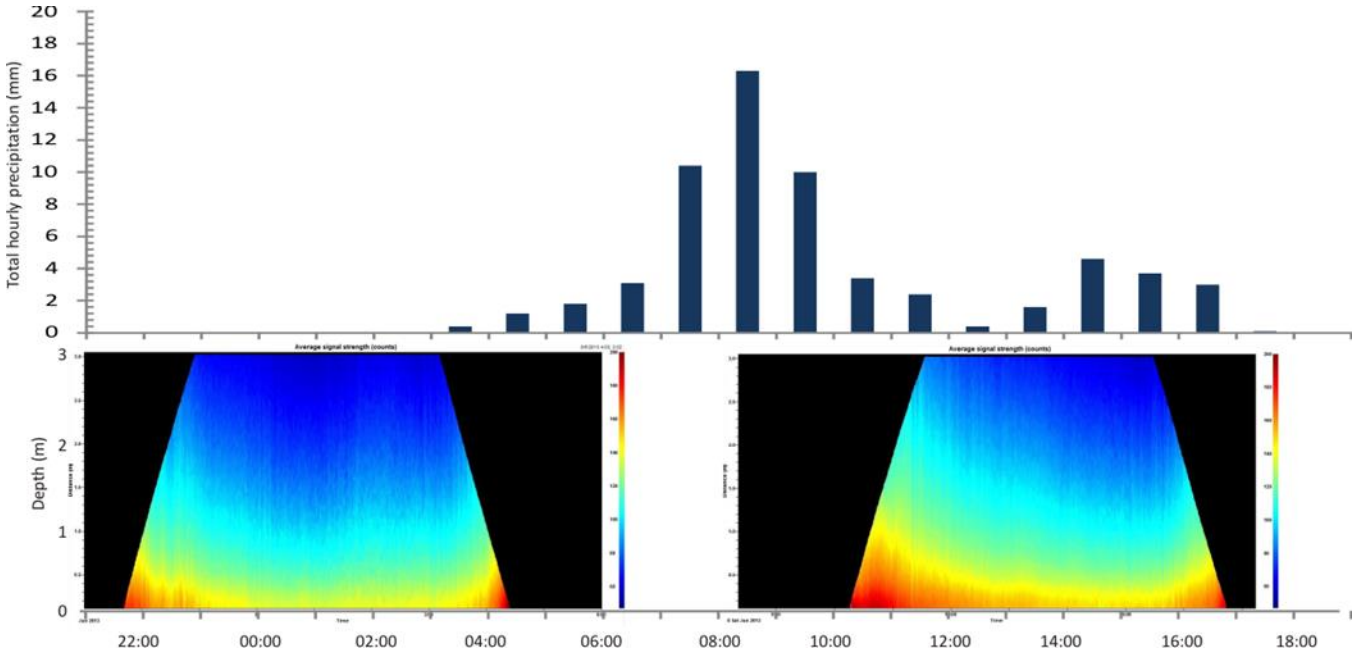

Figure 32 : : Influence of precipitation on suspended sediment concentration (represented as backscatter intensity from the ADCP) from 21:00 June 7 to 19:00 June 8th during Post-tropical storm Andrea.

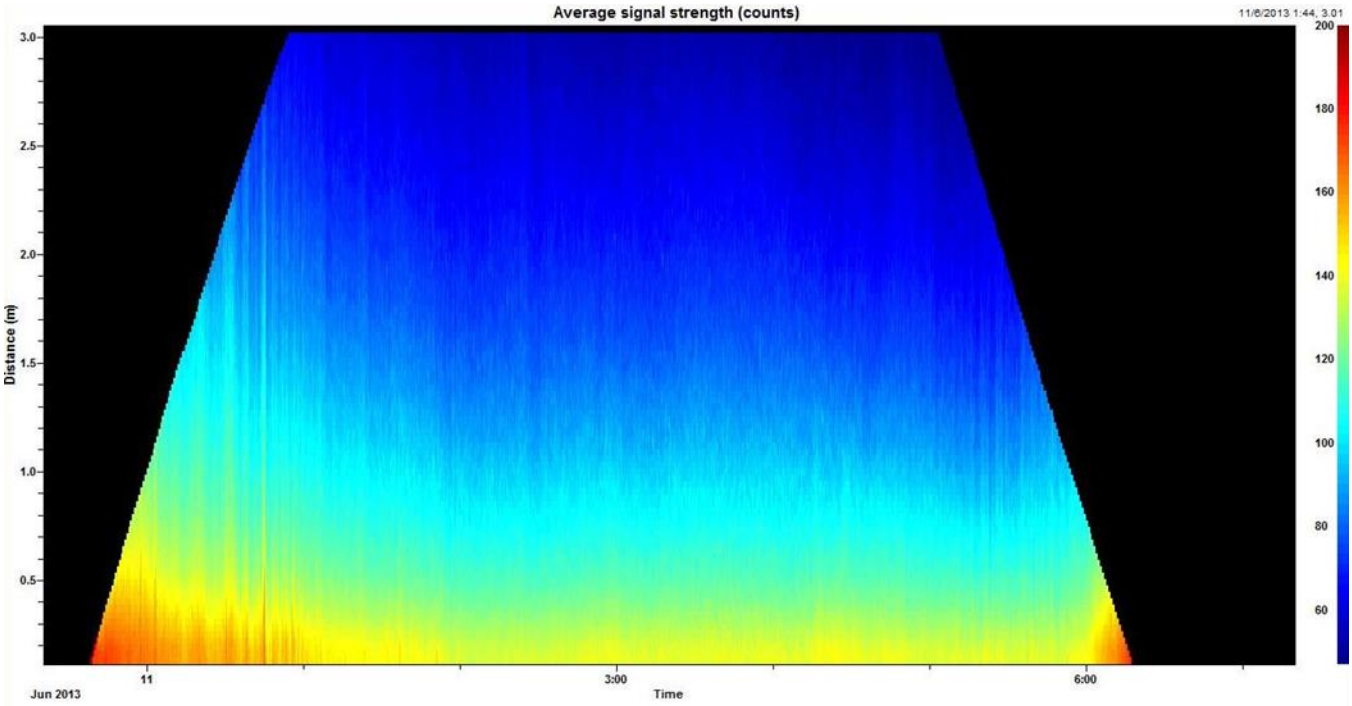

Figure 33: ADCP acoustic backscatter signal strength on June 11, 2013.

Seasonal Patterns

A seasonal pattern was more pronounced in the creek and on the marsh bank than on the marsh surface, as more deposition was found in the three colder temperature deployments at these stations. A major cause to this increased sediment deposition was an increase in incoming suspended sediment concentration in the creek. The processes occurring in the creek are therefore controlling what is subsequently happening on the marsh bank.

Sediment characteristics (grain size, floc fraction) varied more spatially than temporally. There was a clear fining trend into the channel and over the bank, with evidence of single grains settling first in the creek and the sediment in the most flocculated form depositing on the marsh bank with less material left for the marsh surface. While sediment in the creek had a different seasonal pattern than sediments on the marsh, the three marsh stations all had a coarsening of sediment in March which was continued on to the subsequent deployments in May 2013 and June.

A change in grain size was seen with episodic meteorological impacts, such as with rain on June 8th, with the passing of tropical storm Andrea, which remobilized an abundance of sediment which lead to fine sediment incoming on the following tides.

Numerical Modelling

Two main modelling scenarios are presented. In the first, a high-resolution numerical model was used to examine the tidal flooding and draining of channels and vegetated salt marsh flats in Kingsport NS by comparison with acoustic observations of tidal currents. This work indicates the importance vegetation in controlling the hydrodynamics of salt marshes. The second scenario considered the effects of tidal currents and surface waves on sediment re-suspension and transport in a macrotidal environment with expansive mud flats.

Model Scenario One: Influence of vegetation on hydrodynamics and implications of tidal energy extraction

Model

The Delft3D hydrodynamic modelling suite (Lesser et al, 2004) has been successfully applied to intertidal areas to understand the hydrodynamics within saltmarshes (Temmerman et al, 2005; Kusters et al, 2003, Hu et al, 2011). Delft3D is a hydrodynamic and sediment transport model which calculates non-steady flow and transport phenomena that result from tidal and meteorological forcing on a curvilinear, boundary fitted grid. It is well-suited to simulating flows in intertidal areas because it utilizes the Navier-Stokes momentum equations for fluid flow, can flood/dry grid cells due to changes in water level elevation, and uses an advection diffusion equation for calculating sediment transport.

The model area covers a significant portion of the Bay of Fundy and encompasses the entire Minas Basin, which is approximately 110km by 40km.The model domain is composed of three grids shown in Figure 34 with increasingly higher resolution from the Bay of Fundy to the Kingsport marsh, and the grids are connected using a 2-way nesting technique called domain decomposition. Simulations on each grid are run in parallel with the other connected grids, which reduces on the computational needs as compared to a single high resolution grid and enhances the resolution in areas of interest. The largest grid is the outer grid with 200m resolution, which decreases to 33m for the middle grid, and to a resolution of 8m for the inner grid (Figure 34). The model uses eighteen vertical topographically-following ϱ-layers each representing 5.5% of the water depth. The model time step is 3 s to maintain a stable Courant condition for the highest resolution grid.

The model is forced by tides at the entrance to the Minas Basin at Cape Chignecto as shown by the red line in Figure 34. The boundary conditions are generated by the Webtide tidal prediction model (Dupont et al., 2005). Five main tidal constituents (M2, S2, N2, K1, O1) are used to predict the tidal water level elevations at the entrance to Minas Basin, which are input as a time series into the model.

The model bathymetry was defined by combining data from historical charts (Canadian Hydrographic Service), and recent observations from a multibeam echosounder (Bedford Institute of Oceanography) and local airborne laser altimetry (LIDAR) data. The LIDAR data, after correction for laser reflection on the marsh, was used to determine the topography in the intertidal area of Kingsport Marsh with a resolution of

1m over an 8km by 8km area. The bathymetric data sets were merged after being referenced to Canadian Geodetic Vertical Datum 28 (CGVD28), yielding a grid that resolves the intricate tidal marsh topography (Figure 34f).

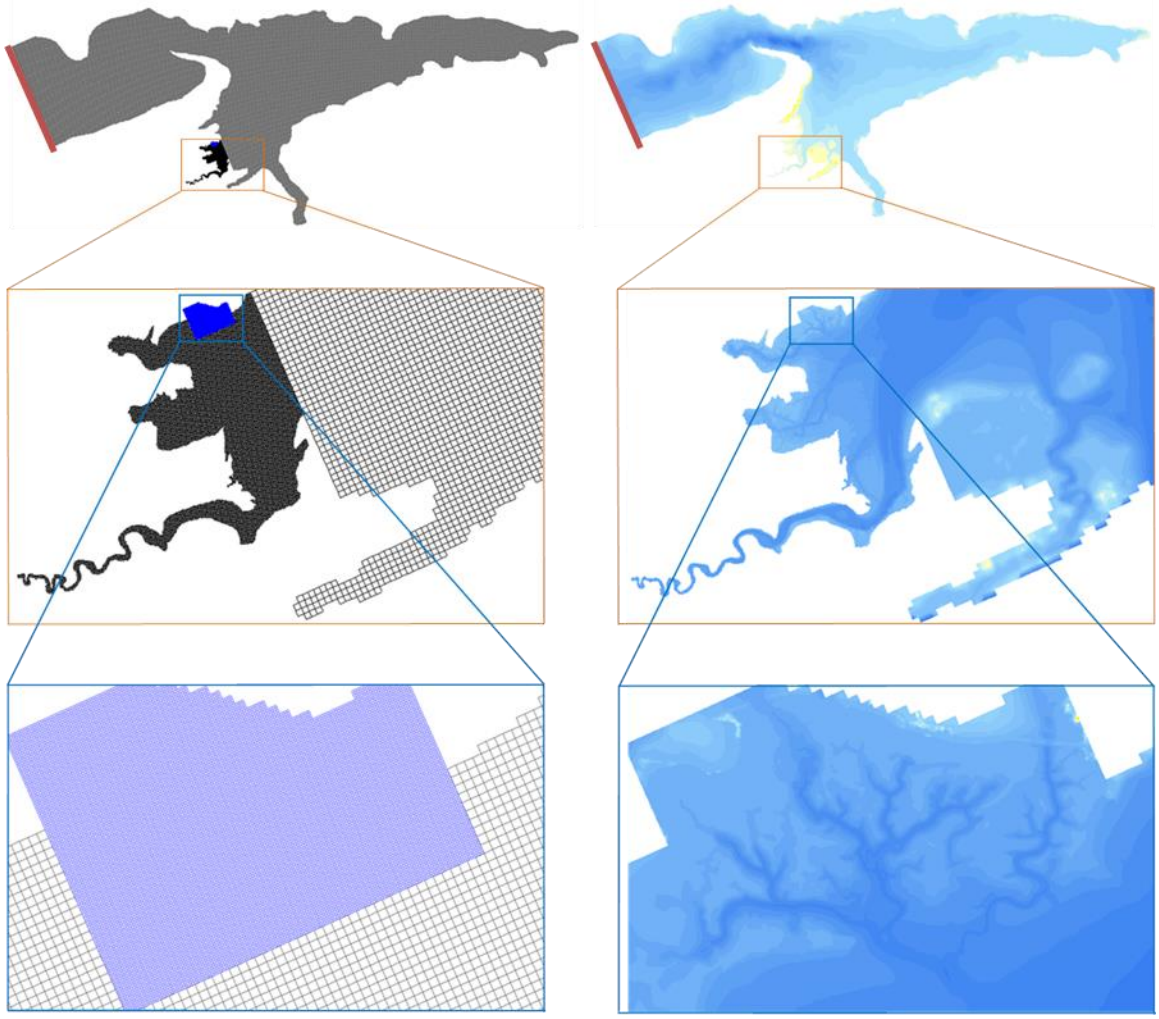

Figure 34: Model grids, boundaries and bathymetry: a)-c) outer (200 m) Minas Basin grid, middle (33 m) Southern Bight grid and inner (8 m) Kingsport Marsh grid. The location of the tidal boundary condition is indicated by the redline in a); bathymetry for each grid with low water depth ranging d) to 100 m; e) to 12 m; and f) to 3 m.

Bottom Roughness

The bottom drag coefficient is a key parameter in hydrodynamic models since it has a significant influence on the calculation of velocity, shear stress, stratification in the near bottom layer, and thus the sediment transport properties (Wu, 2011). To model intertidal velocities, a spatially varying bottom drag coefficient map was developed from the seabed characterization map of the Kingsport Marsh and surrounding area (Figure 2). The map provides the location of 180 polygons describing four different bottom roughness types: low marsh vegetation (*Spartina alterniflora*), high marsh vegetation (*Spartina patens*), intertidal mud, and intertidal sand. Values for the bottom drag coefficient, listed in Table 3, for intertidal sand and

intertidal mud were taken from previous studies (Augustin, 2008). Values for bottom drag coefficients for low marsh and high marsh were determined from the idealized experiments of Pope (2006).

Inner & Middle Grid	Optimal Model Values	Minimum Values Tested	Maximum values Tested
C_d (low marsh -Manning)	0.0309	0.007725	1.545
C_d (high marsh -Manning)	0.0269	0.006725	1.345
C_d (intertidal mud -Manning)	0.002	0.0005	0.1
C_d (intertidal sand -Manning)	0.0023	0.000575	0.115
Vegetation density (low marsh)	4000	1200	4800
Vegetation density (high marsh)	2500	600	2500
Inner grid size (m)	8	3	30
Middle grid size (m)	33	10	50
Outer Grid	**Optimal Model Values**	**Minimum Values Tested**	**Maximum values Tested**
C_d (Minas Basin - Chezy)	65	40	65
Horizontal eddy viscosity (m^2/s)	1	1	100
Tidal boundary resolution (min)	5	5	60
Grid size (m)	200	50	400

Table 3: Key model parameters for the four model scenarios for each grid.

		Constant bottom roughness	Variable bottom roughness	Vegetation model	Vegetation model, variable bottom
M1	η	N/A	N/A	N/A	N/A
	u_{along}	0.11	0.12	0.45	0.46
	u_{across}	0.10	0.17	0.42	0.47
M2	η	N/A	N/A	N/A	N/A
	u_{along}	0.29	0.31	0.49	0.54
	u_{across}	0.35	0.39	0.60	0.69
M3	η	0.99	0.99	0.99	0.99
	u_{along}	0.22	0.27	0.37	0.43
	u_{across}	0.41	0.44	0.45	0.44
C4	η	0.99	0.99	0.99	0.99
	u_{along}	0.85	0.85	0.85	0.84
	u_{across}	0.41	0.39	0.43	0.44

Table 4: Correlation coefficients for water level and velocity components at each instrument site for model run.

Vegetation Model

The use of high roughness coefficients for vegetated surfaces does not account for the influence of vegetation over the whole water depth, and can result in an overestimation of sediment erosion rates (Temmerman et al, 2005). The vegetation model, which parameterizes the plants according to the stem diameter, stem height and plant density can better characterize intertidal flows over different marsh grass types. The vegetation model, described by Dijkstra et al (2010), consists of two parts: a 1DV k-ε turbulence model that simulates the flow and a model that simulates the bending of plant stems, based on a force balance that takes account of both vegetation position and buoyancy as indicated in Figure 35. The vegetation module requires inputs including the average plant stem diameter φ (z), the number n(z) of cylindrical plant structures per unit area in the horizontal plane, the height of the plants z above the bottom. Vegetation samples were taken of the local Kingsport low marsh at instrument site M3 and high marsh (*Spartina patens*) at instrument deployment site M1 during each monthly deployment. The variation of φ(z), and n(z) within the model was assigned by utilizing the satellite imagery and assigning vegetation types to each grid cell depending on their location. The vegetation types consist of two dominant plant species (Table 4). For each of these two species, φ (z), and n (z) were determined by harvesting a representative area the above ground plant material with a 20 cm diameter ring at each instrument location, which are located in both high marsh and low marsh. The harvested vegetation rings were processed for the number of species accounted for. The results for the local observed plant height and density for are given in Table 5 and 6. Four model runs were developed to evaluate the influence of bottom roughness and vegetation, conceptually shown in Figure 36, include:

- constant bottom roughness;
- variable bottom roughness;
- vegetation model with constant bottom roughness; and
- vegetation module with variable bottom roughness.

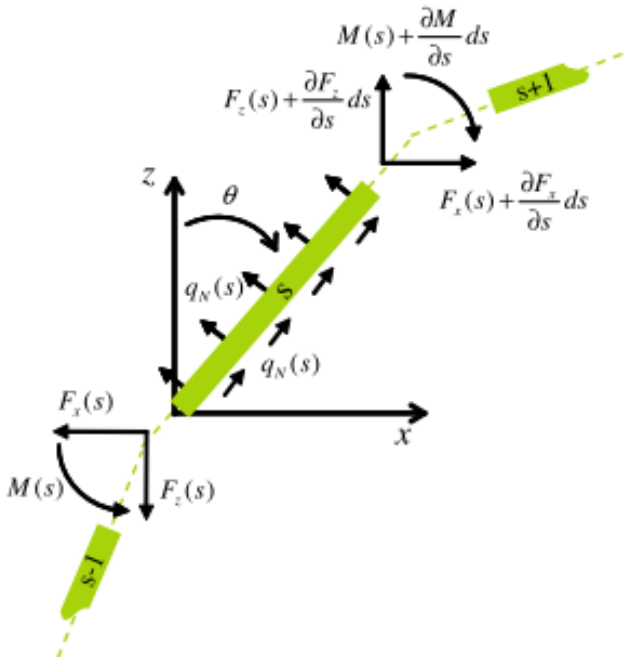

Figure 35: The force balance on one vegetation element s, with adjacent elements s–1 and s+1 (Djikstra, 2010).

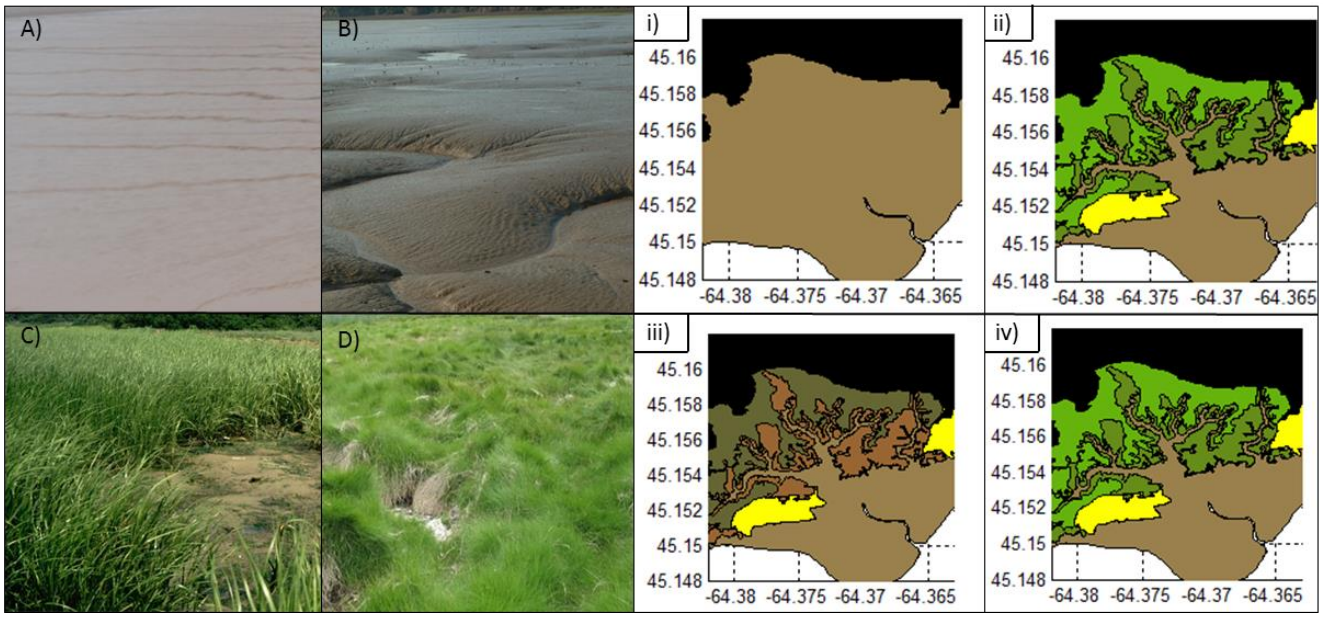

Figure 36: The four different dominant regions within the Cornwallis Estuary: A) intertidal sand; B) intertidal mud; C) low marsh vegetation (Spartina alterniflora); and D) high marsh vegetation (Spartina patens). The four model scenarios are illustrated for the inner grid: i) constant roughness, ii) varying roughness, iii) vegetation model, iv) vegetation model with varying roughness.

Vegetation Density (plant/m²)						
	M1		**M2**		**M3**	
	Alive	Dead	Alive	Dead	Alive	Dead
May 4 2012	828	1846	2515	382	573	1687
May 9 2012	1814	1273	1337	891	1337	859
June 2012	3119	2069	4584	1783	1050	1210
July 2012	5539	3342	2960	1337	1019	255
August 2012	1560	2005	2069	2419	923	1464
Sept 2012	3788	3661	955	1496	1178	859
Nov 2012	286	2928	0	1464	0	573
Jan 2013	0	1974	0	923	0	732
March 2013	N/A	N/A	0	2610	0	509
May 2013	668	2674	N/A	N/A	N/A	N/A
June 2013	1305	4265	2992	764	3024	0

Table 5: Vegetation densities determined from individual stem counts within a 0.2 m diameter circle.

Max Vegetation Height (cm)			
	M1	**M2**	**M3**
May 4 2012	32.5	30	42.5
May 9 2012	35	42.5	35
June 2012	47.5	25	70
July 2012	35	35	65
August 2012	40	40	70
Sept 2012	45	42.5	82.5
Nov 2012	45	32.5	47.5
Jan 2013	37.5	30	30
March 2013	40	40	40
May 2013	47.5	40	17.5
June 2013	40	20	27.5
Average	40	34	48

Table 6: Vegetation heights measured at each instrument on the low and high marsh

Model Results

The model output was compared against hydrodynamic data collected over several spring tidal cycles from May 5-9 2012, May 25-28 2013, and June 8-13 2013. Hydrodynamic data were measured at two different locations in the Bay of Fundy. The first site is a bottom moored array of instruments located at the northern tip of the Southern Bight in Minas Basin deployed by Bedford Institute of Oceanography. The instrument array contains an Optical Backscatter Sensor (OBS), and upward facing and downward facing acoustic Doppler current profiler (ADCP) measuring at 1 m above the bottom. The second study site is located in a 2nd order creek in the Kingsport Marsh near the Cornwallis Estuary deployed by Saint Mary's University. The study site contains an upward facing Nortek Aquadopp on the bottom in the thalweg of the creek, and three single-point Nortek Vectors (Acoustic Doppler Velocimeters) that measure flow 10cm above the bed located at increasing distances away from the thalweg of the creek.

Minas Basin ADCP at A5

Preliminary analysis of the model output was completed using data from the A5 site deployed by Bedford Institute of Oceanography, located in the Southern Bight of Minas Basin (Figure 37). The model was run for a period of nine days, from June 5 -13 2013. This period was modelled to validate the model output against the bottom-mounted upward facing ADCP in the model's coarsest grid to determine model accuracy in modelling the hydrodynamics within Minas Basin. The water levels and flow velocities were compared to the model output. The resulting correlation coefficients for the comparison between modelled and observed are 0.99, 0.82, and 0.92 for water levels (η, u- and v-components of velocity respectively).

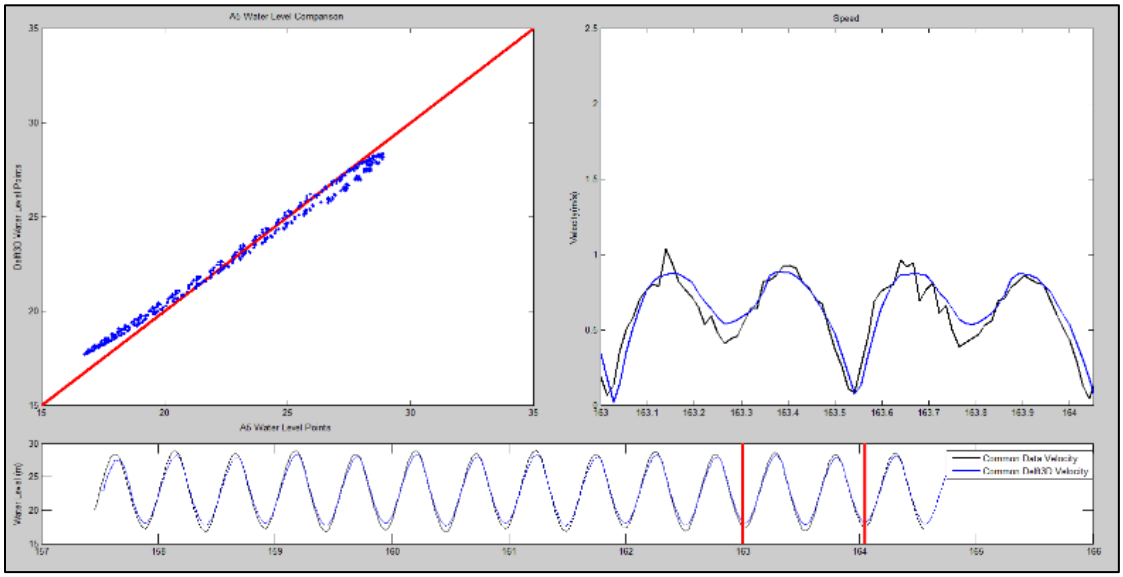

Figure 37: Preliminary analysis of the model output of June 5th to 13th 2013, using study site M1 located in the Southern Bight of Minas Basin. Modelled vs observed water levels are plotted in the top left with an r2 value of .99. Modelled vs observed water levels are plotted as a function of time in bottom. The red lines highlight a time period with two tidal cycles and plots the relative speed of modelled and observed (top right).

Kingsport Creek Aquadopp at C4

The model was run for a period of nine days, from May 25-28 2013 to validate the hydrodynamics against the bottom-mounted upward-facing Nortek Aquadopp (Adop) at site C4 in the Kingsport Marsh tidal creek. The water levels and flow velocities and directions were compared to the model, resulting in correlation coefficients of 0.99, 0.82, and 0.92 for □, u and v respectively (Figure 38).

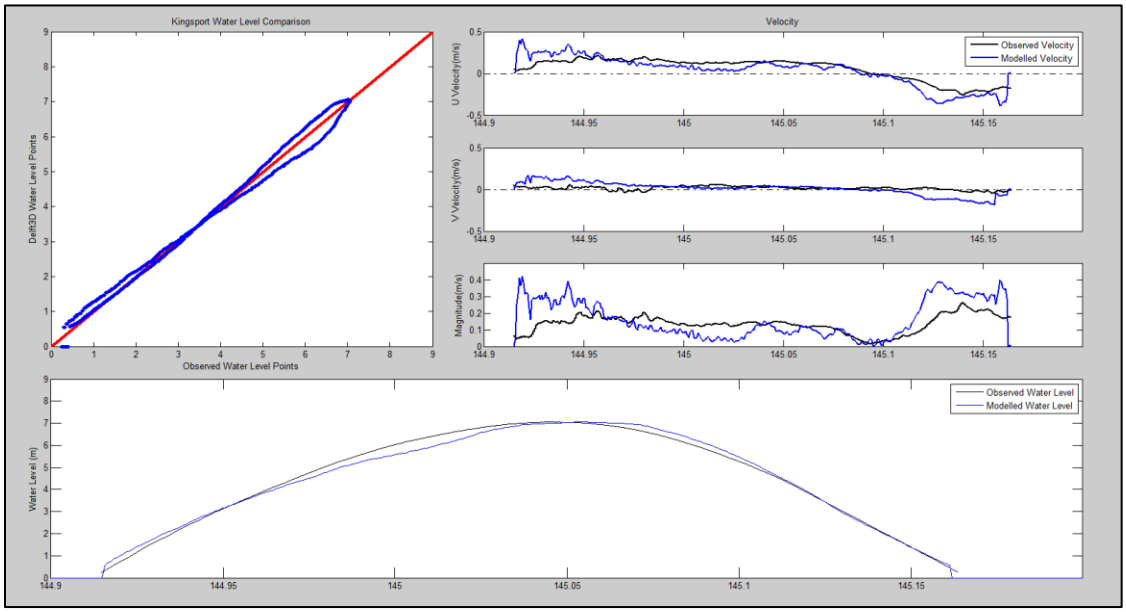

Figure 38: Preliminary analysis of the model using study site C4 located in the creek of Kingsport Marsh. Modelled vs observed water levels are plotted in the top left with an r2 value of .98. Modelled vs observed water levels are plotted as a function of time in bottom. Modelled vs Observed U, V velocities and magnitude of velocities are compared in the top right.

The Aquadop located in the creek at Kingsport Marsh was configured differently for different deployments. The sensor has two settings that control the vertical bin size resolutions that obtain a profile of the water column above the instrument. The HR setting has a vertical bin size resolution has 97 bins at a 3cm resolution over a maximum range of 3m (Figure 39). The standard setting has a vertical bin size resolution has 18 bins at 50 cm spacing over a maximum range of 9m (Figure 40). The horizontal velocity structure in the creek was compared between the instrument and the model for horizontal velocities in each vertical layer as a function of time and water depth. The HR setting provides valuable and detailed information of the velocities (i.e. signal to noise ratio, correlation, backscatter amplitude data) for 3m above the instrument but does not yield viable results that can be compared to the model. This is due to highly turbid water and the very small bin size of the HR Aquadopp setting. The normal setting attain the high vertical resolution of the HR setting but the range extends over the entire water column above the instrument. Observing the velocity profile over the full water column provides a better understanding of the creek hydrodynamics for comparison to model outputs (Figure 40).

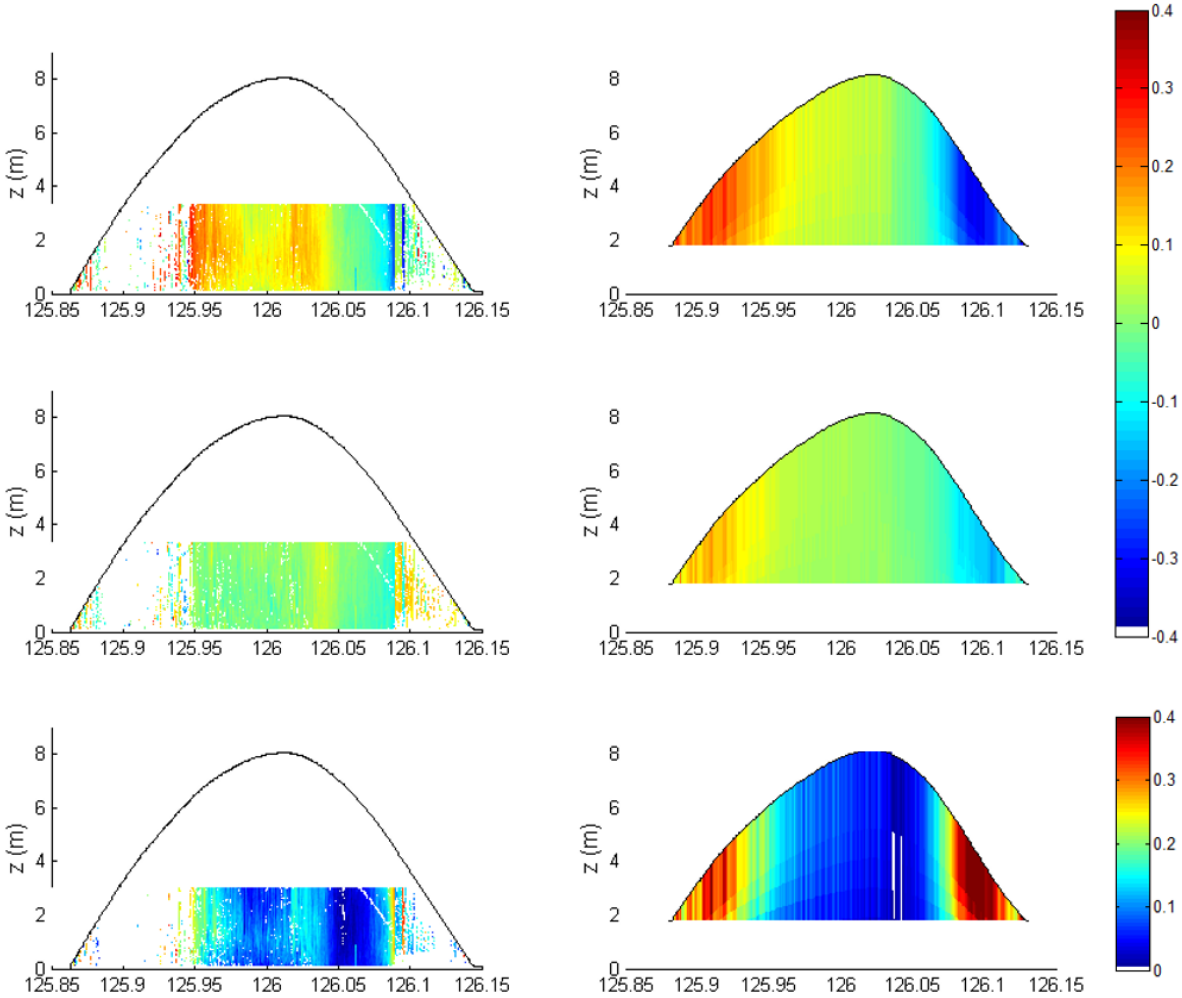

Figure 39: Time evolution of vertical current profiles (m/s) over a tidal cycle on May 5, 2012, at the Kingsport Aquadopp: a) observed along-channel component; b) observed cross- channel component; c) observed magnitude; d)-f) corresponding model results using 6 vertical layers. The Aquadopp was operating in HR (high resolution) mode and observed the velocity profile over a range of 3 m.

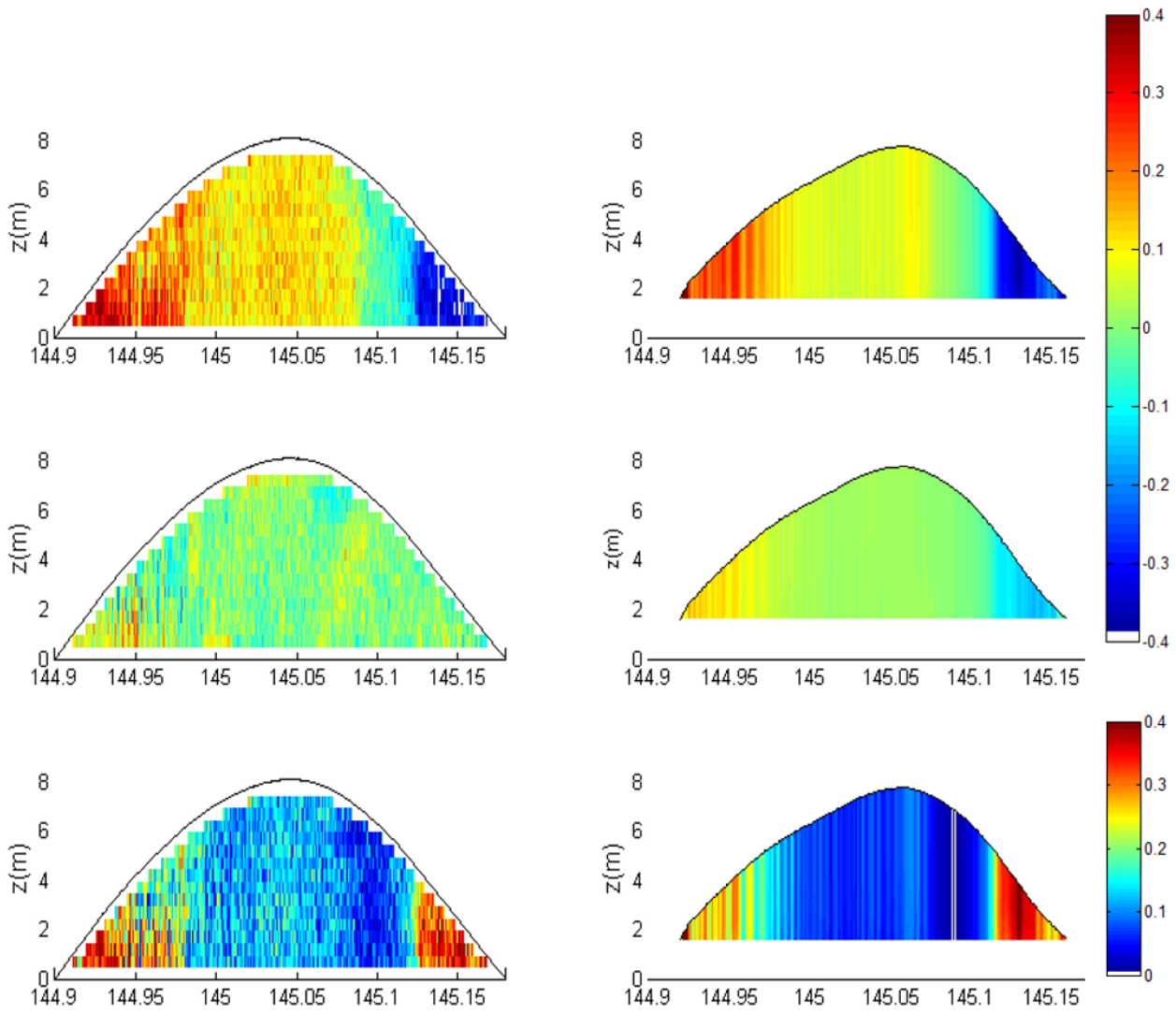

Figure 40: Time evolution of vertical current profiles (m/s) over a tidal cycle on May 25, 2013, at the Kingsport Aquadopp: a) observed along-channel component; b) observed cross- channel component; c) observed magnitude; d)-f) corresponding model results using 18 vertical layers. The Aquadopp was operating in standard resolution mode and observed the velocity profile over a range of 9 m.

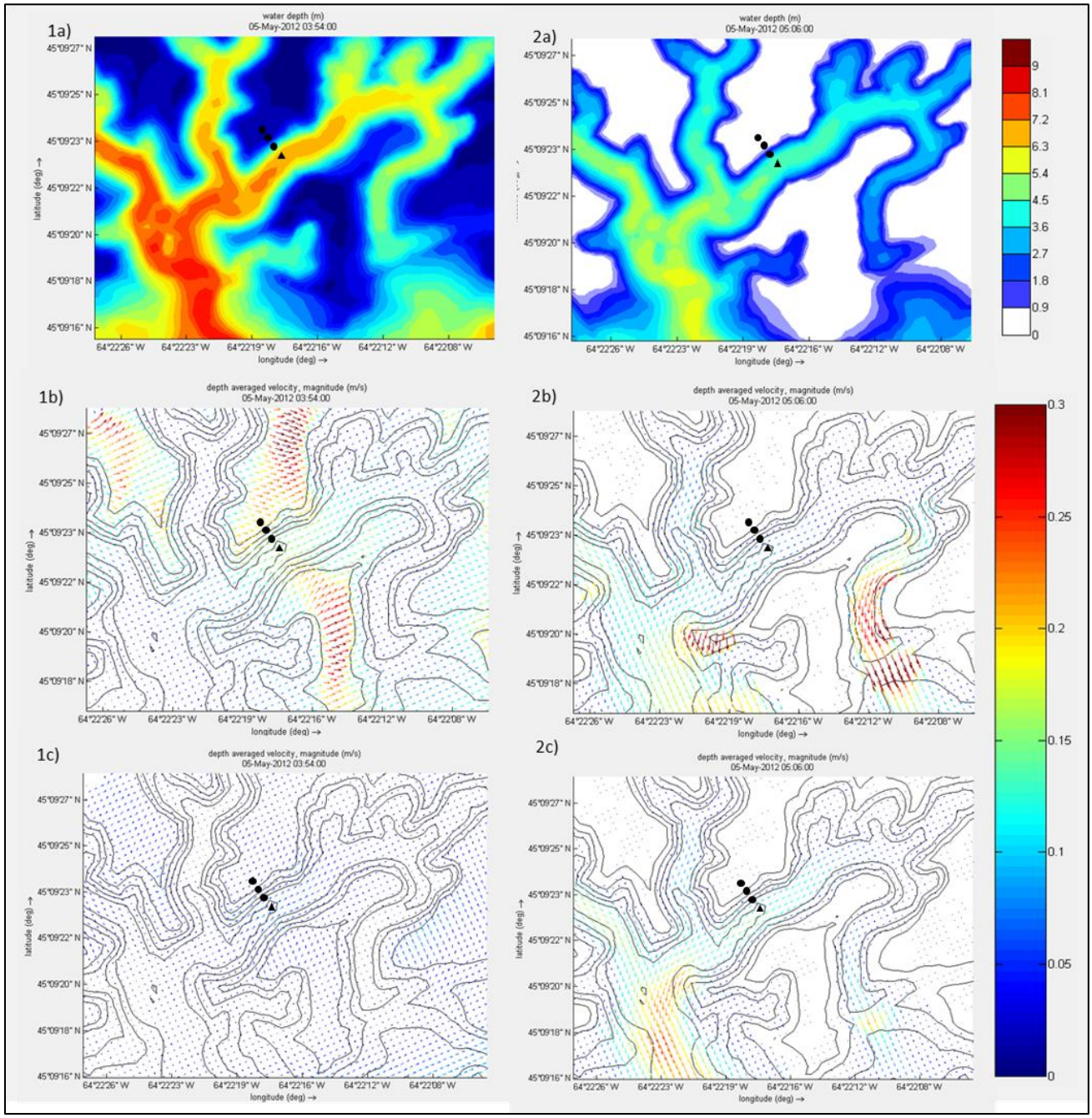

Figure 41: Water depth in the Kingsport Marsh (1a and 2a) and velocity vector maps for constant bottom model scenario (1b and 2b) and the vegetation module model scenario (1c and 2c) for two time periods: 1) flood tide (May 5 2012 3:54am), and 2) ebb tide (May 55:06am). The black symbols indicate instrument locations; the ADVs are indicated by circles and the Aquadop by the triangle.

Sensitivity Analysis

The four model scenarios were calibrated by adjusting key parameters within the ranges listed in Table 3, to assess sensitivity of the model. Key parameters in the outer grid were adjusted to understand the sensitivity to predicting water levels and currents in the Minas Basin, particularly related to the strong tidal currents in Minas Channel (grid size, bottom friction, horizontal eddy viscosity, tidal boundary conditions). Parameters for the inner and middle grid were adjusted to understand the importance of flow controlling factors had on the hydrodynamics within the Kingsport tidal creek and marsh surface (grid size, bottom friction, and vegetation parameters).

Vegetation Model Results

To determine the relative influence of the simulated vegetation, velocity maps for the constant bottom roughness and vegetation model runs are shown in Figure 41. The two simulations were conducted for a tidal cycle (May 5, 2012) with high frequency (30 s) output. Two areas were selected from the two models near the data collection study site to illustrate the difference between a constant bottom roughness and a vegetated surface. The constant bottom roughness run allows water to flow freely over the low and high marsh surfaces. The vegetation model run significantly dampens the flow over the marsh and re-directs it into the channels, demonstrating that the vegetation model more accurately represents flows over salt marshes.

The model results were evaluated by comparing the water levels and velocity components with observations. The correlation coefficient (R) for each model is given in Table 4. The vegetation model increases the correlation between modelled and observed velocities especially higher on the marsh surface. The vegetation model clearly results in better representation of flows over the salt marsh as indicated by the results in Figures 42 and 43 and the correlation coefficients listed in Table 4.

Salt Marsh and Tidal Channel Drainage

The instruments in Kingsport Marsh were arranged in a linear array with increasing elevation from the thalweg of the creek in a different local roughness from mud in the creek (C4), low marsh vegetation (M3) and high marsh vegetation (M2, M1). The sensors, which include a Nortek Aquadopp (Adop) at C4 and three Nortek Vectors (Acoustic Doppler Velocimeters, ADVs) at sites M1, M2, M3 were oriented 72.4° from North to be aligned with the channel. This resulted in the primary axis oriented along-channel and the secondary axis oriented across-channel. Three different model scenarios were compared to the four instruments located in the Kingsport marsh shown in Figure 40 and 41.

The model results indicate strong shallow flows at the onset of flooding and at the end of ebb. This may be due to the flooding and drying of the model cells, influenced by a threshold depth (presently set to 10 cm) above which hydrodynamic calculations are performed in each 8 m wide model grid cell. In reality, the v-shaped channel would be deeper in some areas and therefore there may be a need to use a more computationally demanding higher resolution grid of 3 or 4 m.

The vegetation model scenarios were able to replicate similar flows observed over the marsh while the model scenarios without vegetation produced currents that were much stronger than observations, particularly at the two high marsh instruments, M1 and M2. More testing and sensitivity analysis will be completed to investigate the appropriate model settings. Depth-averaged current velocities at C4 for flood and ebb (e.g. Figure 44) indicate fairly good agreement between model and observations, and little influence of vegetation on flows in the creek. The time series of tidal currents in the channel (Figures 39, 40, 42) hysteresis of tidal currents (Figure 44) indicate a significant time lag between the time of high tide and reversal of flow (with flood currents of up to 0.1 m/s, up to 2 hours after high tide). This time lag suggests that considerable momentum is needed to decelerate the water mass and will be investigated further.

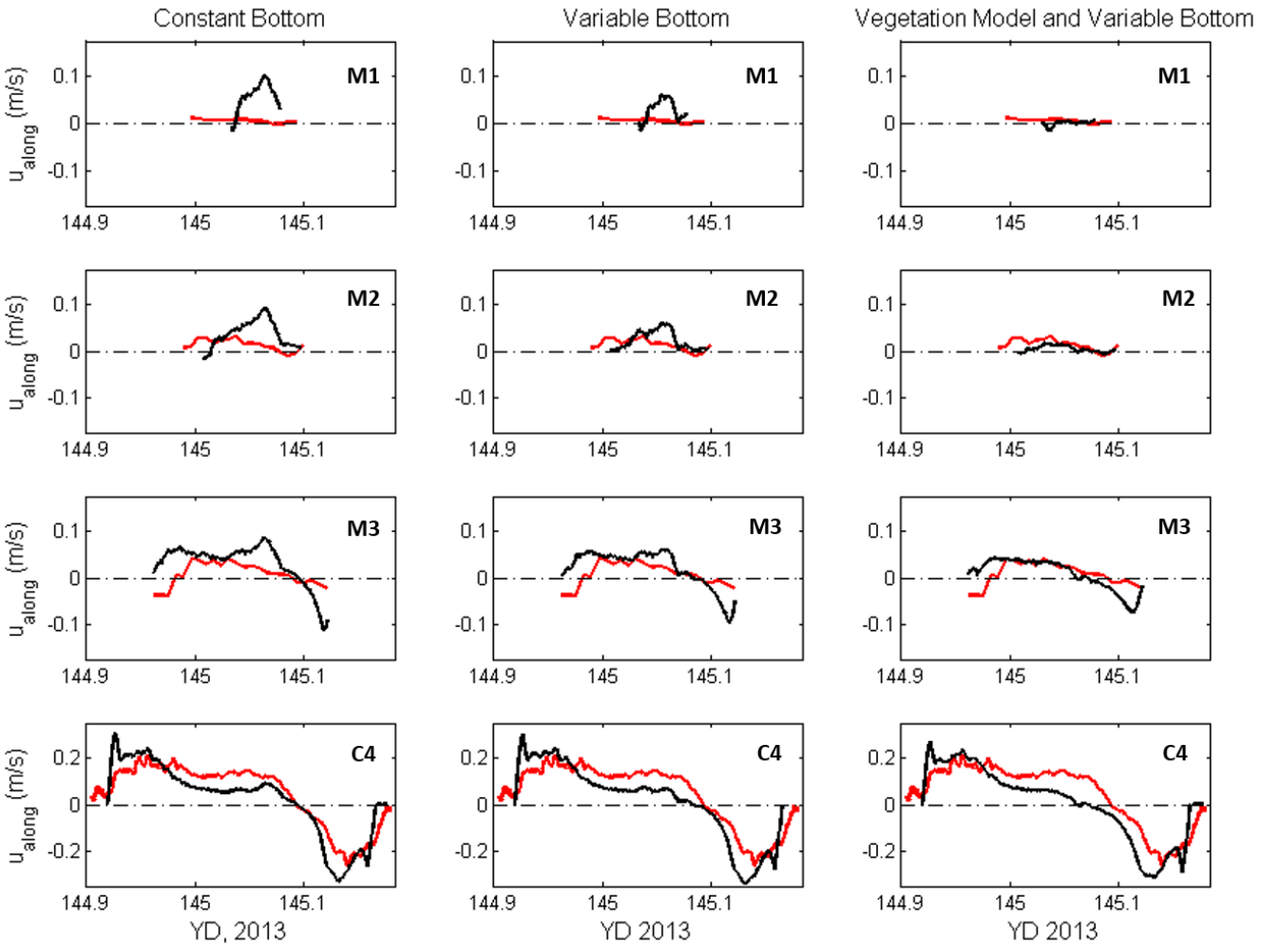

Figure 42: Along-channel velocity component and inundation times on May 25, 2013, for three model scenarios at the four instrument locations, observations (red) and model results (black). Model results are averaged over a period of 5 minutes to match the 5-minute match the 5-minute burst averages of the observations.

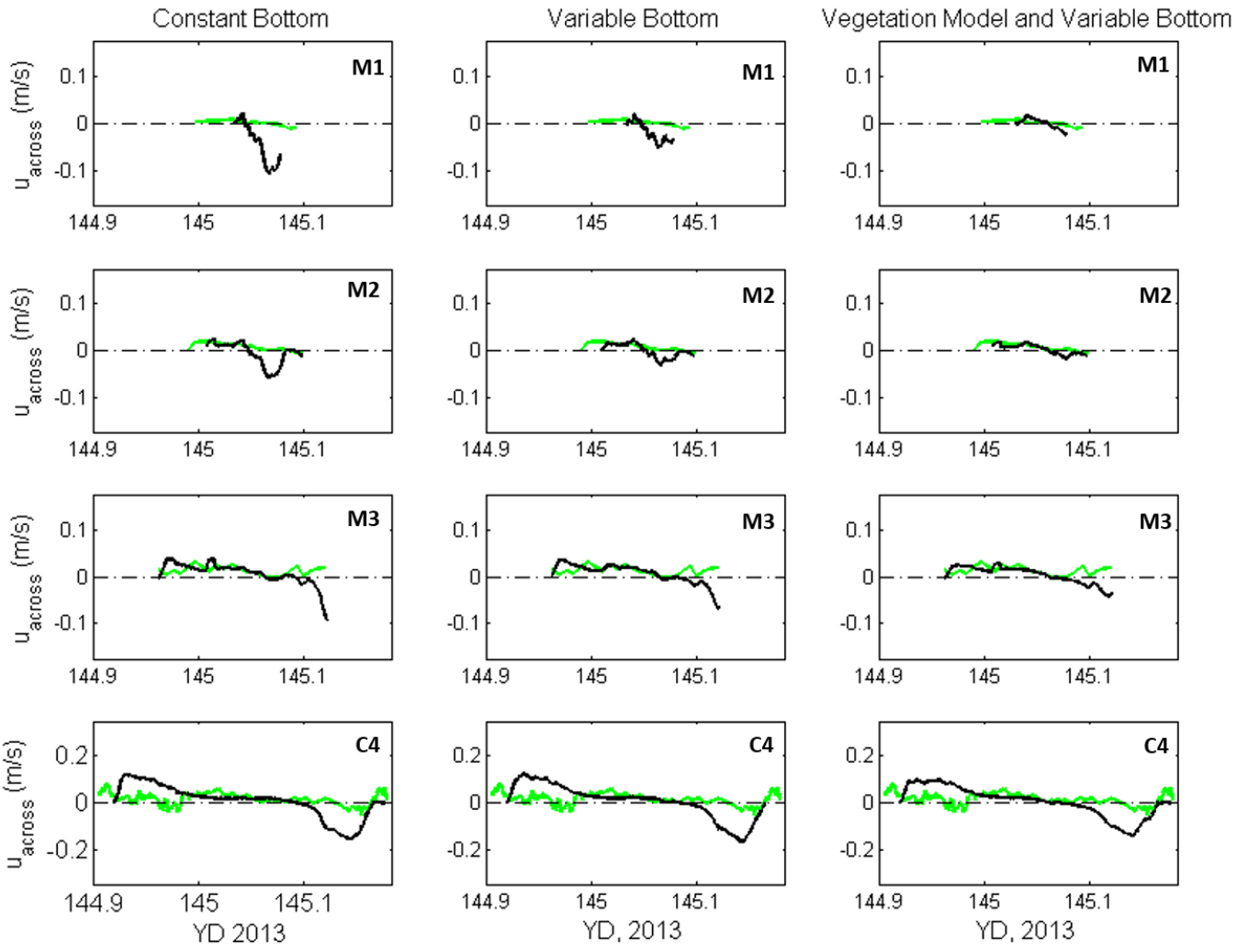

Figure 43: Cross-channel velocity component and inundation times on May 25, 2013, for three model scenarios at the four instrument locations, observations (black) and model results (green). Model results are averaged over a period of 5 minutes to match the 5-minute burst averages of the observations.

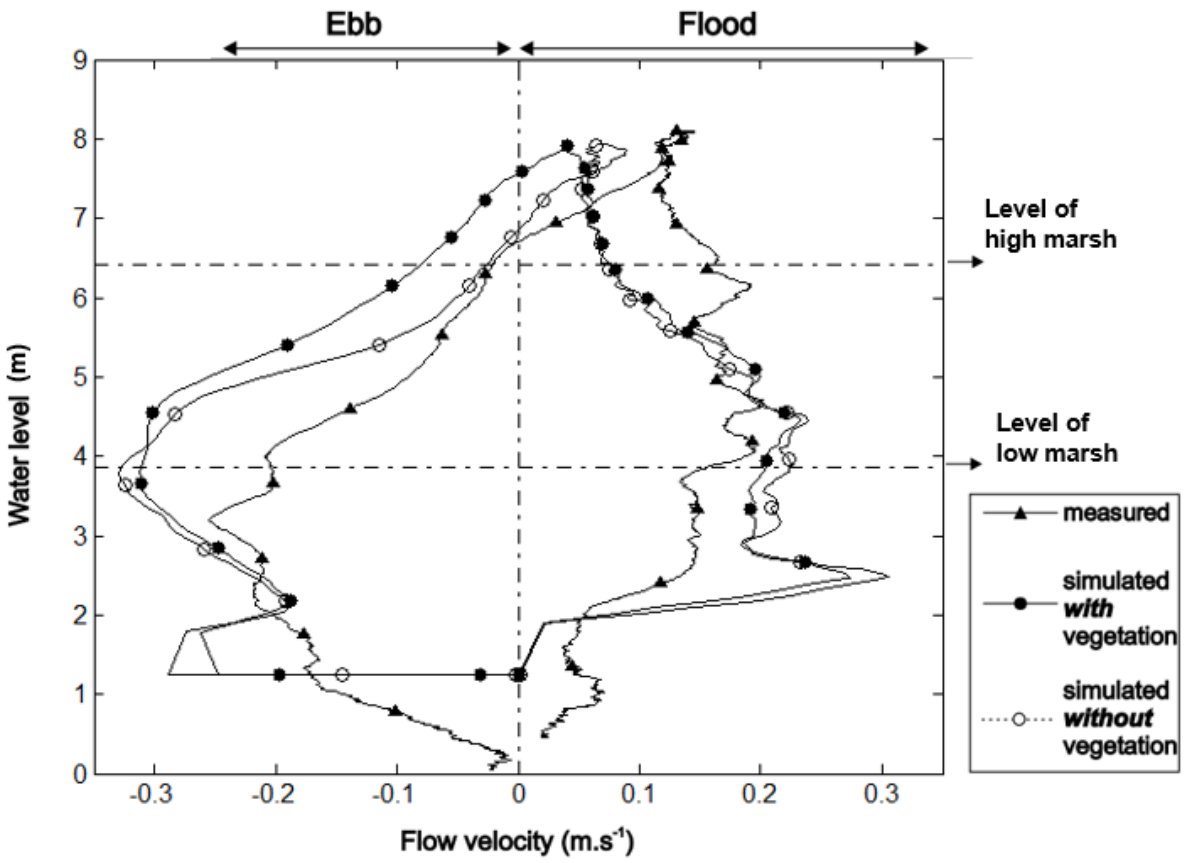

Figure 44: Along-channel velocity profiles for flood and ebb tide at C4 for the tidal cycle on May 25th from 01:00-04:00. Model results are shown for the constant bottom roughness case and the vegetation model with variable bottom roughness (8 m horizontal grid, 18 vertical layers, 3 s timestep). The data are from the Aquadop.

Tidal Power Extraction Case

To determine the far field effects of tidal power extraction a model case study was developed replicate an array of 15 turbines (

Figure 45). The turbines are simulated as semi-porous grid plates that influence the flow in the bottom vertical half of the water column. The model duration was May 24-28, 2013, and the vegetation model was implemented to examine the far-field impacts on the intertidal zone at Kingsport. At the Kingsport Marsh this simulation results in a 0.2 m (3.5%) reduction in the water level (Figure 46), suggesting that turbines will change salt marsh water level elevations and inundation times. According to Karsten et al. (2008) a 3.5% reduction in water level in the Minas Basin represents a 2.0GW tidal power extraction in the Minas Passage. The results help to understand the far field effects of tidal power extraction in the Minas Passage on intertidal areas like the Kingsport marsh, and provide groundwork for additional modelling work to be done.

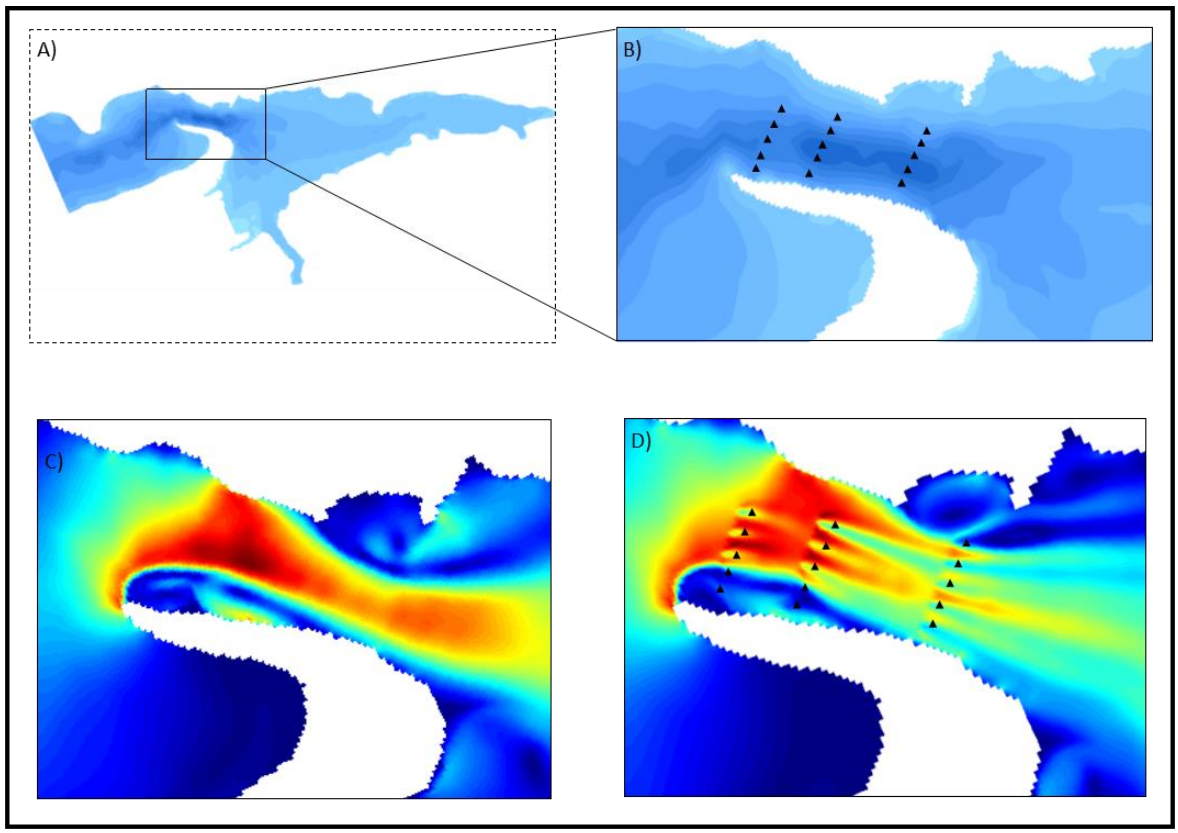

Figure 45: Results from preliminary model tests for an array of turbines in Minas Passage: A) outer grid model domain; B) 15 turbine sites implemented by semi-porous plates in the lower half of the water column; C) flood tide velocity contours (up to 5 m/s) without turbines; D) flood tide velocity contours with turbines.

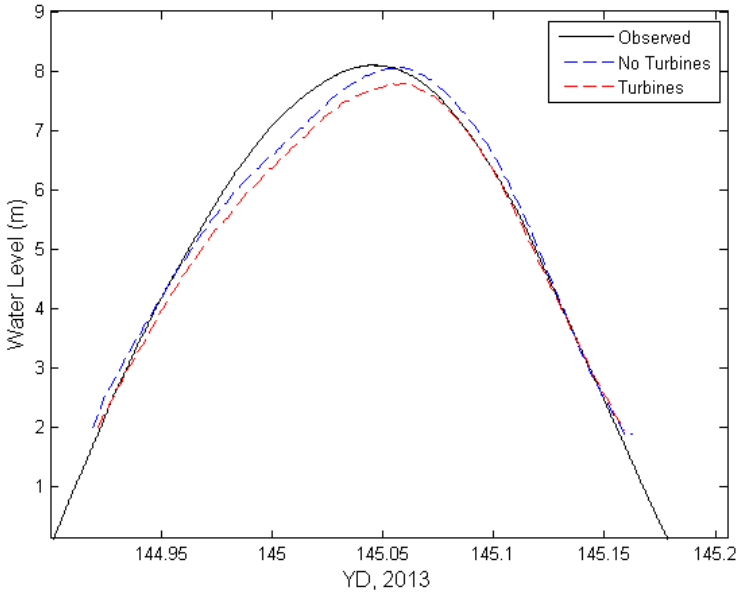

Figure 46: Water levels at Kingsport (C4), indicating a 0.2 m (3.5%) reduction in water levels for the case of an array of turbines in Minas Passage.

Future Work

The 3-grid high-resolution Delft3D model results are well correlated with hydrodynamic observations in the Kingsport Marsh but more work is needed to fine tune the model. The sensitivity analysis varied a wide range of parameters for different degrees of variability in the model, but optimal values for these parameters have not yet been determined. Future work will include additional sensitivity testing and optimization of the model hydrodynamics.

The next phase of work will be detailed wave, current and sediment modelling of the period in June 2013, corresponding to the CCGS Hudson research cruise in Minas Basin. Data obtained from the cruise will used to validate the sediment and wave simulations in Minas Basin (ADCP moorings, ship-based ADCP transects, suspended sediment concentration grab samples, bed surface sediment grab samples from the Kingsport mud flats).

Model Scenario 2: Tidal current and wind-wave controls on suspended sediment concentrations

This scenario considers the effects of tidal currents and surface waves on sediment resuspension and transport in a macrotidal environment with expansive mud flats. Observations of tidal currents from bottom-mounted Acoustic Doppler Current Profilers (ADCPs) and satellite-derived surface suspended sediment concentrations are presented. The data are used to validate the predictions of a coupled hydrodynamic-wave-sediment model for study periods in the winter and summer of 2009 and 2013, and to assess changes to suspended sediment concentrations on tidal flats induced by wave-orbital and tidal current induced bed shear stresses. This work indicates the importance of waves in combination with tidal currents on inducing re-suspension in macrotidal estuaries.

Observations

Field Observations

Field observations were collected during two periods in 2009, in winter (January-February) and summer (July-August). The field data are a subset of the multi-year current meter observations collected in the upper Bay of Fundy by the Bedford Institute of Oceanography. Current profiles were collected at eight sites (Figure 1 and 47), with instruments deployed at five sites in the winter period and at four sites in the summer period. During each deployment some sensors were located in Minas Passage (A1, A2, A3, A4, A7, A8) and some were located in Minas Basin (A5, A6). In this work we focus on tidal currents to validate the model in Minas Passage and in Minas Basin. The sensors were RDI ADCPs that were deployed in an upward-looking orientation and operated at 300 kHz to collect hourly-averaged current data in 2 m vertical bins. The velocity data indicate strong tidal currents that are modulated over daily and spring-neap tidal cycles. In Minas Passage, speeds can be up to 5 ms^{-1} (at A8) and recirculation can occur along the southern shore near Cape Split (at A7). In the central area of Minas Basin the flows can reach 1.5 ms^{-1} (at A5, A6).

Sediment concentrations and current velocities were measured at Starr's Point, an intertidal channel in a salt marsh in the Cornwallis River Estuary (CE, Figure 47), in the Southern Bight of Minas Basin in the summer. The currents were measured using a Nortek Vector single-point acoustic current meter at this site, which undergoes flooding/drying over every tidal cycle. Current speeds were typically very low at 0.01-0.05 ms^{-1}. Suspended sediment concentration (SSC) was measured using an optical backscatter sensor (OBS) that was calibrated against water samples with known sediment concentrations, and the observations indicate very high SSC of up to 200-400 gm^{-3} with high variability over tidal cycles.

Satellite Observations

Remote sensing of ocean colour from space has allowed sediment properties to be observed over large spatial scales. The MEdium Resolution Imaging Spectrometer (MERIS, Doerffer (1999)) was a scientific instrument on board the European Space Agency (ESA) Envisat Earth-orbiting satellite that operated from 2002-2012. From the near daily synoptic data at 300 m resolution, the total suspended matter (TSM) concentration is derived from empirical relationships and is equivalent to the suspended sediment concentration (SSC) referred to hereafter. Data from this sensor have elucidated cyclical variation in SSC in Minas Basin over seasonal timescales, with concentrations ranging from 10-30 gm^{-3} in the winter to less than 1-10 gm^{-3}in the summer in the central part of the basin (Tao, 2013).

There were no sensors deployed in Minas Basin that were capable of measuring the surface waves during the study periods in 2009. The ADCPs were located below the wave base, in water depths where the relatively high frequency (>0.2 Hz) wave fluctuations in pressure and velocity were negligible. A very limited amount of wave validation data were available in Minas Basin from the Jason-1 (Ménard, 2003) satellite altimeter, from which the significant wave height is estimated to an accuracy of 0.04 m on every 10.9 day global cycle along its track (

Figure 47).

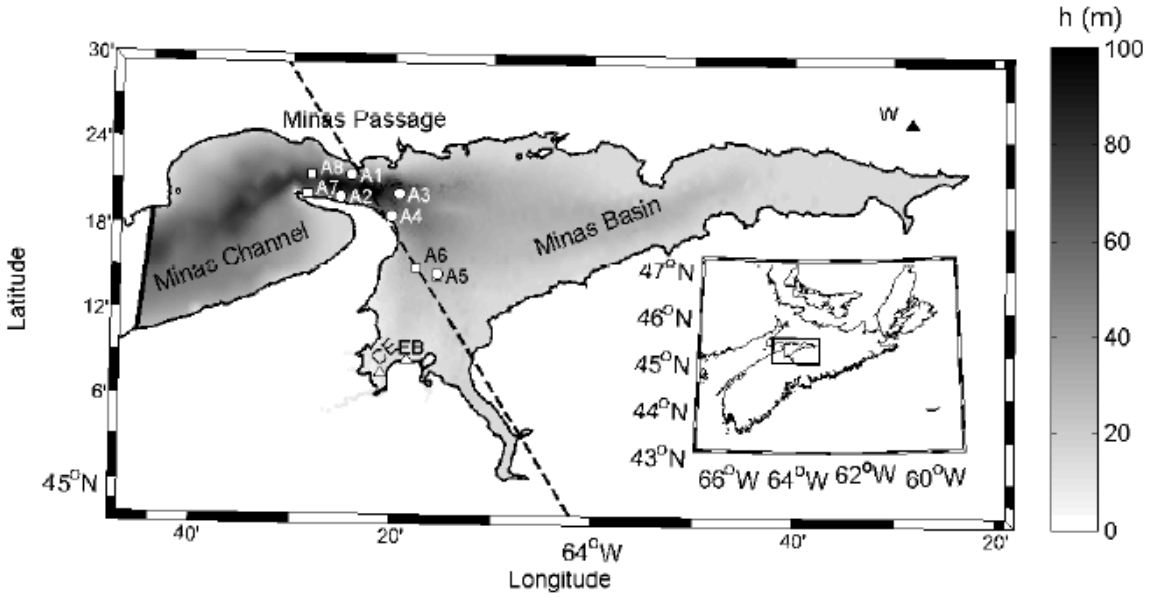

Figure 47: Location map of Nova Scotia (inset) and bathymetry of Minas Channel and Minas Basin covering the model domain. Sensor locations in 2009 are indicated (ADCPs at A1-A8; OBS at CE in the Cornwallis Estuary; winds at W). The dashed line indicates the path of the Jason-1 satellite and EB denotes tidal flats at Evangeline Beach.

Numerical Model

The Delft3D hydrodynamic model (Lesser, 2004) uses a finite difference scheme to solve the full horizontal momentum equations, numerically simulating water-levels and currents driven by atmospheric (e.g., wind and pressure) and boundary forcing (e.g., currents, tides, river flows). Delft3D uses a k-epsilon turbulence closure scheme. Surface waves and wave-current interactions are computed by coupling the hydrodynamic model to the spectral wave model SWAN (Booij, 1999) that predicts wave generation, propagation, transformation and dissipation in shallow water. The sediment component includes parameterizations of hydrodynamic roughness in the bottom boundary layer, bedload and suspended-load transport, cohesive and non-cohesive sediment types, and deposition, erosion, and evolution of bed morphology. Delft3D has recently been used to estimate the dynamics and transport rates of sediments (e.g., Hu, 2009), fresh/salt water (e.g., Elias, 2012), and dissolved organic materials (e.g., Brown, 2013) and to simulate a range of shallow coastal environments including beaches (e.g., Reniers, 2004; Hartog, 2008), estuaries (e.g., Leorri, 2011), tidal marshes (e.g., Temmerman, 2005),) and river deltas (e.g., Mulligan, 2010; Nardin, 2012).

Tidal Hydrodynamics

For the Minas Basin model, the bathymetric grid was constructed by combining existing hydrographic survey charts with high-resolution multi-beam bathymetry (Shaw, 2012) in the Bay of Fundy. The data were interpolated onto a spherical structured grid covering the domain shown in
Figure 47 that extends 105 km in the east-west (x) direction and 45 km in the north-south (y) direction, with horizontal resolution of 170 m in the x-direction by 200 m in the y-direction. The vertical grid has 10-layers in topography-following σ-coordinates, and the model was run in three-dimensional mode using a time step of 30 s with the open boundary placed at the western end of Minas Channel. A water-level boundary condition was developed from tidal predictions from WebTide (Dupont, 2002) with the 5 primary tidal constituents (M2, N2, S2, K1, O1) shown in Figure 48. Default parameter settings for the hydrodynamics gave the best agreement with observations, including a bottom friction coefficient of C_D = 0.0023 and a horizontal eddy viscosity of A_H = 1 m^2s^{-1}. The model was run for four 35-day simulations: two in each of winter and summer in 2009 over the time periods that correspond to ADCP observations, for the two cases of forcing by tides-only and forcing by tides+waves.

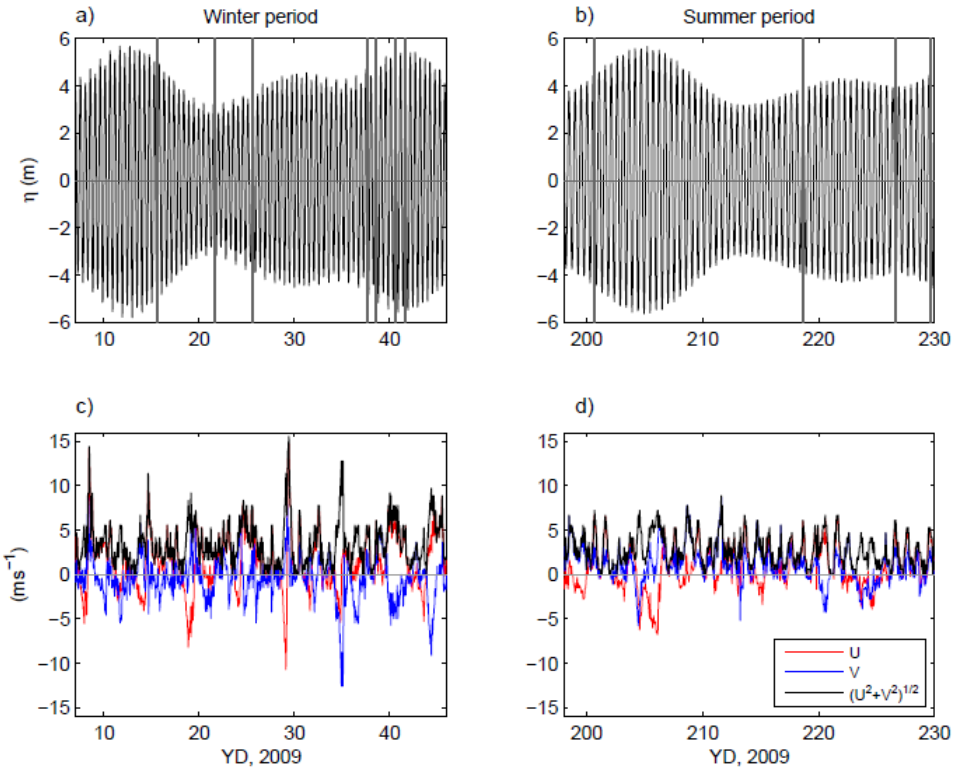

Figure 48: Tidal water level elevations at the model boundary in Minas Channel for the a) winter, and b) summer periods, with vertical lines indicating times of MERIS satellite observations; wind components observations for c) winter, and d) summer 2009.

Waves

Wind observations obtained from Environment Canada (climate.weatheroffice.gc.ca) Stn. No. 8201380 at Debert (see location in Figure 47and data in Figure 48) were used to force both wind-driven hydrodynamics and wind-generated surface waves within the model domain. The wave computations were performed on the same grid as the hydrodynamic computations, using 24 logarithmic frequency bins from 0.05-1.00 Hz and 36 directional bins with 10° resolution. Dissipation by wave breaking used the Battjes (1978) expression with γ = 0.73, and bottom friction was prescribed using the JONSWAP (Hasselmann, 1973) formulation with C_j = 0.067 m^2s^{-3}. By solving the action balance equation (Booij, 1999), stationary spectral wave computations were made at hourly intervals, and the results were communicated between the hydrodynamic and wave models every 60 minutes in simulation time.

Sediments

The concentration of suspended sediment throughout the model domain was initialized at zero therefore requiring sediment to be eroded from the bed. The initial bed conditions were developed from bottom texture observations of Amos (1980) where most sediments in the central part of Minas Basin are (i) non-cohesive sands to gravels with relatively high settling velocities, and (ii) fine cohesive muds in shallow

areas around the rim of the basin (namely the Cornwallis River estuary, the Avon River channel, near Economy Point, and Cobequid Bay). A simple bi-modal distribution map that resembles the Amos (1980) observations was developed to describe the initial bed conditions, consisting of fine mud in water depths of 10 m and less (relative to the mean sea level datum) and sand in depths greater than 10 m. A series of sensitivity tests for varying sediment properties (e.g. grain size, settling velocity, critical shear stress) was completed to determine the summer and winter sediment conditions, after comparison with satellite imagery (Tao, 2013). For the sand layer, a mean grain diameter (d_{50}) of 2 mm was used with the non-cohesive sediment formulation of Van Rijn (2007). For the cohesive intertidal mud layer a settling velocity w_s = 0.1 mms^{-1} was used, corresponding to a grain size of less than 100 μm, and the critical shear stress for erosion (τ_{cr}) was varied based on values determined by Amos (1992) for bed sediment samples on the tidal flat of the Cornwallis river estuary. Across the 2.5 km wide mudflat they measured a range of in situ critical bed shear stresses: 0.1-7.5 Nm^{-2} (July and August, 1989-1990). For the results presented here, we used a critical bed shear stress of erosion τ_{cr} = 2 Nm^{-2}. Although this value may vary seasonally due to biofilm growth increasing particle cohesion in summer (Borsje, 2008; Tao, 2013), we hold the sediment properties constant for the present study to evaluate the effects of tides and wind-waves on re-suspension.

Bed Shear Stress

The total shear stress acting at the bed is predicted from the combination of stresses from waves and currents. The magnitude of the wave-driven shear stress at the bed is given by:

$$\tau_w = \frac{1}{2}\,\rho_o f_w u_w^2 \qquad \text{Equation (9)}$$

where ρ_o is a reference water density, u_w is the wave orbital velocity and f_w is the wave friction factor (a function of u_w, the wave frequency, and the roughness length, see Soulsby (1993)). The magnitude of the tidal current stress is:

$$\tau_c = \rho_o C_D u_c^2 \qquad \text{Equation (10)}$$

where C_D is the flow drag coefficient, and u_c is the tidal current velocity. The mean bed shear τ_m at timescales longer than individual waves is expressed as a combination of the stress contributions from waves and currents according to Soulsby (1993) as:

$$\tau_m = \tau_c \left(1 + 1.2\left(\frac{\tau_w}{\tau_w + \tau_c}\right)^{\frac{3}{2}}\right) \qquad \text{Equation (11)}$$

with the stress direction oriented in the current direction. The driving mechanism for sediment re-suspension from the bed is the maximum shear stress, which is significantly higher than the mean shear stress over the timescale of individual waves. The maximum shear stress is related to the shear stress from the wave-orbital velocity and the increased current shear stress and depends on the angle α between wave and current directions:

$$\tau_{max} = ((\tau_m + \tau_w \cos\alpha)^2 + (\tau_w \sin\alpha)^2)^{\frac{1}{2}} \qquad \text{Equation (12)}$$

Erosion from the bed occurs when the τ_{max} exceeds the critical threshold τ_{cr}, at a rate dependent on excess shear stress ($\tau_{max} / \tau_{cr} > 1$), the particle settling velocity and the sediment concentration in the near-bed fluid layer (Lesser, 2004). This expression, combined with defining the critical shear stress of erosion for the sediment, controls the process of sediment transfer from deposits on the bed to in suspension in the water column.

Results

Tidal Current Predictions

The tidal hydrodynamics were validated for both the winter and the summer simulations. For the winter period, the observed near-surface currents in Minas Passage (A1) and in Minas Basin (A5) are shown in Figure 49. The mean water depths at these sites are 53 m (at A1) and 28 m (at A5), and the near-surface acoustic bin location varies in depth from 2 m below the water surface at low tide to 18 m below the water surface at high tide. In the model the surface layer thickness, which varies with water depth, is 4.5 to 5.8 m thick (at A1) and 2.1 m to 3.6 m thick (at A5). The semi-diurnal signal has magnitudes at A1 up to 4.6 ms^{-1} over this time, with most of the flow in the east-west direction (u-component) and flood-tidal currents that are stronger than ebb-tidal currents. At A5 the current speeds can be up to 1.4 $m \cdot s^{-1}$, oriented predominantly in the north-south (v-component) direction. The predicted currents agree well with the magnitude and phase of the observations at both sites. The correlation coefficient (R) between observations and predictions was very high (>0.94) at zero lag for both u and v current components at the instrument sites in Minas Passage and Minas Basin.

For the summer period, the observed near-surface currents in Minas Passage (A8) and in Minas Basin (A5) are shown in Figure 50. The mean water depth at A8 is 68 m, and the model surface layer thickness varies with water depth from 4.5 to 5.8 m (at A1). The current speeds can be up to 5.2 ms^{-1} at A8 and up to 1.4 ms^{-1} at A5. The predicted currents agree well with the magnitude and phase of the observations at these sites, although the model over-predicted the currents in Minas Passage at A8 by up to 9 percent for the fastest flows that occur during spring tides. R between observed and predicted currents was very high (>0.94) at A5 in Minas Basin, an encouraging result on which the sediment predictions depend.

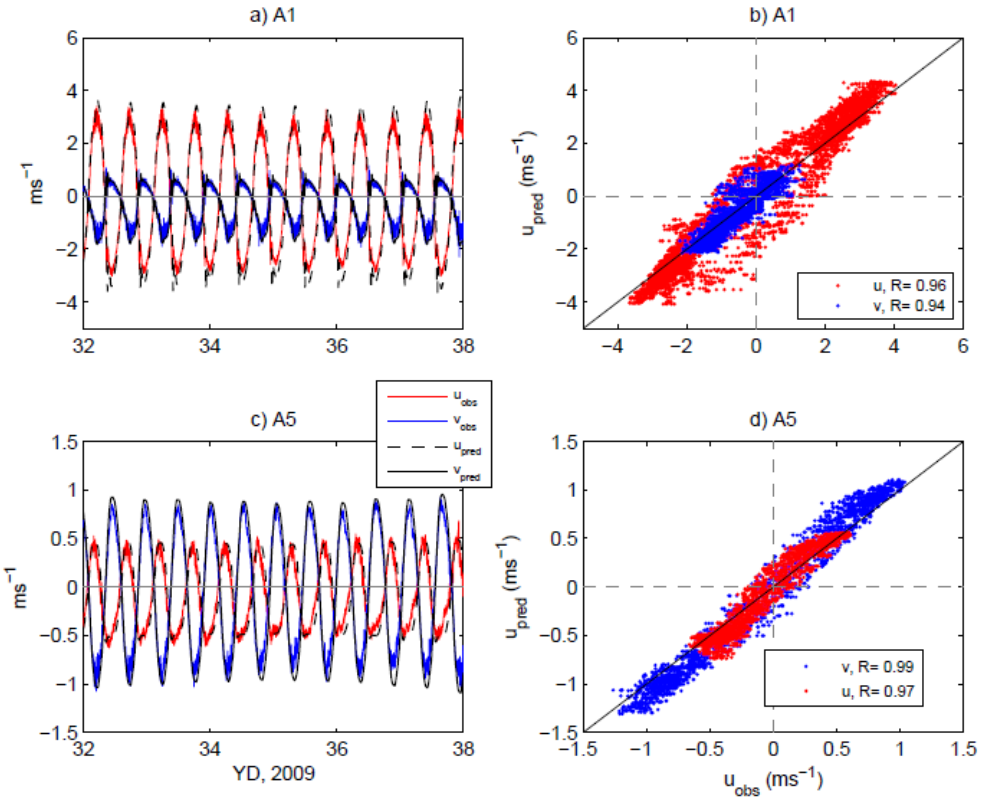

Figure 49: Winter validation: time-series for a selected 6-day period and scatter plots for a 35-day period indicating the correlation coefficient R between observations and predictions of current velocity components: a)-b) at A1 in Minas Passage; c)-d) at A5 in Minas Basin.

Surface Suspended Sediment Predictions

Model results for SSC indicate that sand particles are transported as bedload and suspended load during ebb and flood phases of the tide, with highest concentrations in Minas Passage where currents are strongest. However the coarse particles have a high settling velocity and sink out of suspension with slackening of the tidal currents, and therefore do not remain in suspension for timescales longer than a few hours. The finer material, eroded from the tidal flats that surround the basin, can remain in suspension in the water for timescales longer than a tidal cycle after they are re-suspended. This material alters the optical properties of the water column enough to be visible by satellites. The MERIS observations and model predictions of SSC (including waves) are shown in Figure 51 for dates in winter (YD 15) and summer (YD 226), both at times corresponding to ebb-tidal flow. The results suggest that the model adequately simulates some important sediment transport phenomena, including higher surface SSC in the source areas (the tidal flats in Cobequid Bay to the east and in the Southern Bight of Minas Basin), and lower SSC in the central part of Minas Basin and in Minas Passage. The results also suggest that for sediments to exist in suspension at the surface over deeper (e.g., h >10 m) areas of the basin, they must be re-suspended in the shallow intertidal areas and be advected. The MERIS imagery also indicates that in general the SSC is significantly larger in winter than in summer. The model results, in general agreement with the satellite

observations, suggest that this strong seasonal dependence is a function of both the tidal currents and wind-generated waves in the basin.

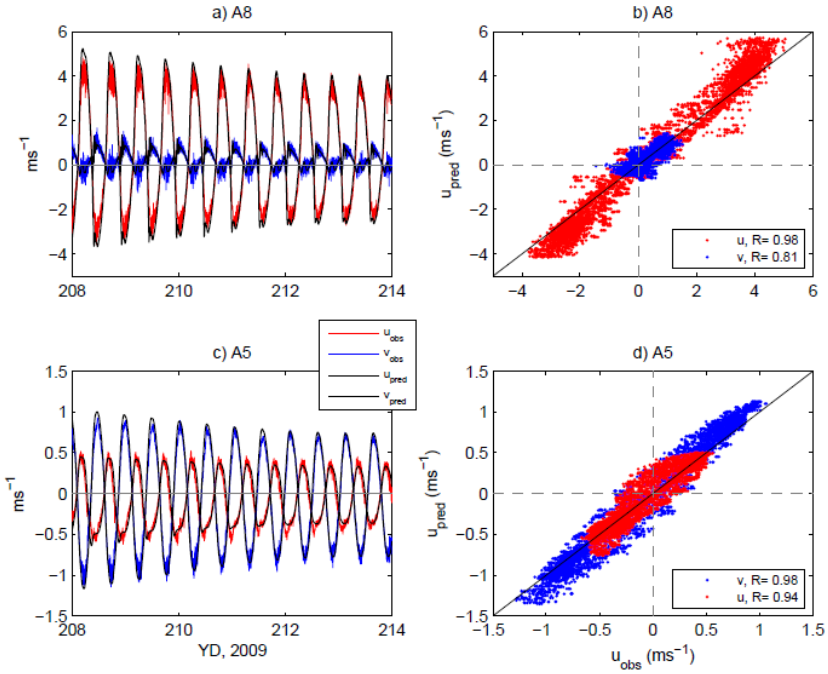

Figure 50: Summer validation: time-series for a selected 6-day period and scatter plots for a 35-day period indicating the correlation coefficient R between observations and predictions of current velocity components: a)-b) at A8 in Minas Passage; c)-d) at A5 in Minas Basin.

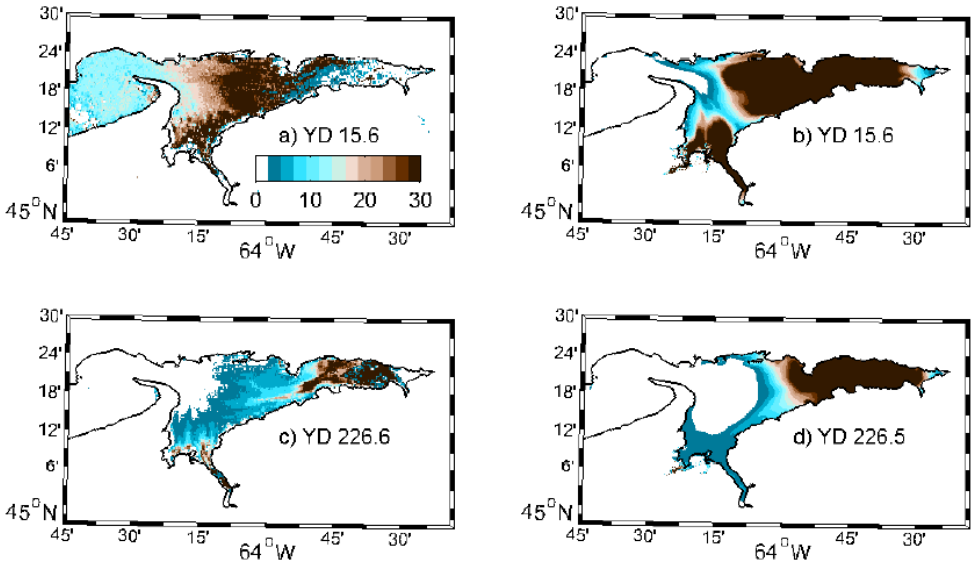

Figure 51: Selected satellite observations and model predictions of SSC (gm⁻3) at the ocean surface: a) MERIS observation in winter, and b) model prediction in winter; c) MERIS observation in summer, and d) model prediction in summer.

Waves and Current Effects on Suspended Sediment Concentration

The largest waves in Minas Basin over the two study periods occurred on YD 35, due to the strong 15 ms^{-1} winds blowing from north to south. This resulted in significant wave heights up to 1.5 m (Figure 52a) and wave orbital velocities up to 0.7 ms^{-1} that were highest on the tidal flats (Figure 52c). Although the tidal current speeds can greatly exceed this in deeper parts of the basin (Figure 52b), the tidal currents near the bed in the intertidal areas are typically much weaker (Figure 52d), around 0.1 ms^{-1}or less. The model was used to determine the excess bed shear stress due to waves ($\Delta\tau_b$) by taking the difference between the results for the two cases of forcing by tides+waves and forcing by tides-only. The results, shown in Fig 3.6e indicate a large region across the intertidal zone in the Southern Bight of Minas Basin where waves have contributed around 1 Nm^{-2} to the bed shear stress above the amount induced by the tidal currents. This value represents the instantaneous effect of waves in causing re-suspension. The difference in SSC (ΔSSC) represents the cumulative effect of waves causing re-suspension over time (Figure 52), with advection of sediment-laden water into the basin by the tidal currents. The increased sediment in suspension due to waves is over 25 gm^{-3} in some areas, particularly over and near the tidal flats at this time.

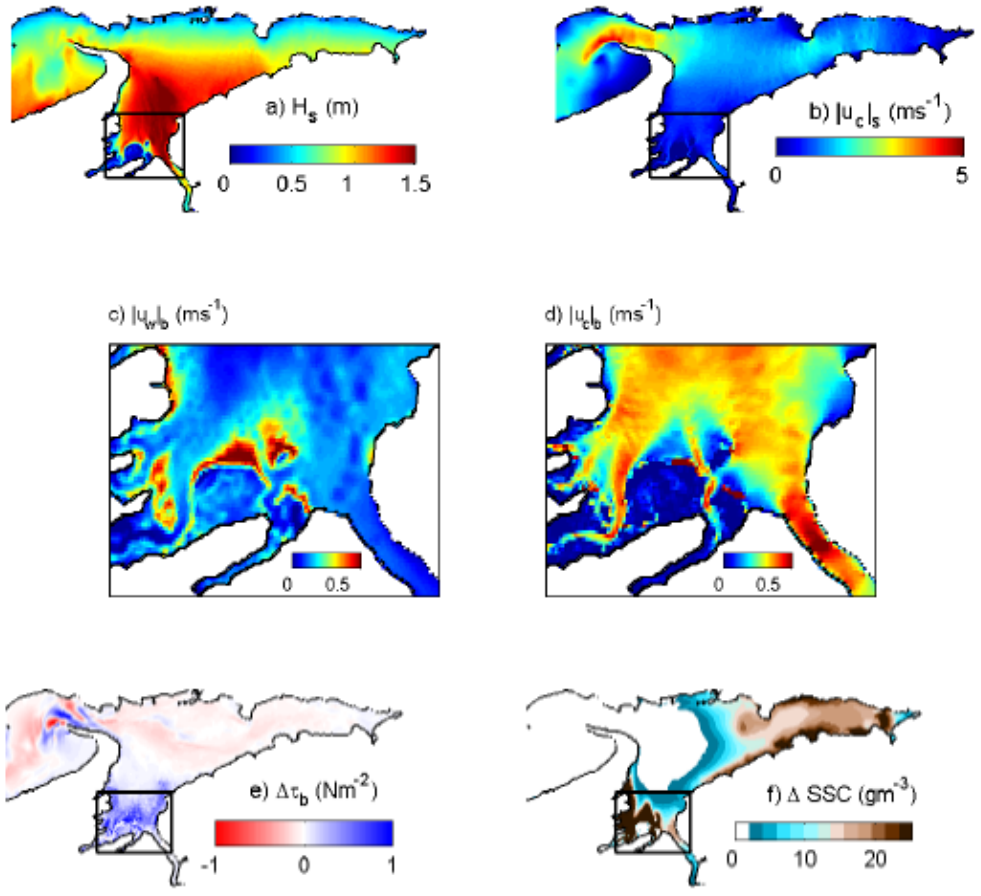

Figure 52: Model results in Minas Basin during a wind event (12.8 ms-1 from 350o) at ebb tide in winter (YD 35.1) with box identifying the Southern Bight (SB): a) significant wave height; b) surface current magnitude; c) near-bed wave orbital velocity magnitude in the SB; d) near-bed current magnitude in the SB; e) difference in maximum bed shear stress between tide+wave and tide-only cases; f) difference in surface SSC between tide+wave and tide-only cases.

To illustrate the effects of waves over longer time periods, the time-series of H_s and SSC in Minas Basin (A5) and in an intertidal area (CE) are presented in Figure 53. The significant wave height averaged over the winter period is 0.32 m at A5 and 0.13 m at CE and the effects of tidal modulation of the wave height are apparent at both sites. However, there is a 3-hour offset in H_s peaks that corresponds to the tidal cycle, since waves at A5 are modulated by the strong currents in the basin and waves at CE are dependent on the changing water depth on the tidal flats. The SSC values are an order-of-magnitude higher on the tidal flats than in the basin, suggesting that re-suspension from the bed occurs in the intertidal zone. There is also a time lag of 3-4 days in the peak SSC values between sites, indicating that the transport of suspended material from tidal flats to the central part of the basin occurs over 6-8 tidal cycles. The surface waves increase the SSC at both sites, compared to the SSC re-suspended only by tidal currents, but especially when combined with the highest tides of the spring/neap cycle. MERIS observations at A5 range from 10.1-18.2 gm^{-3} for the seven observation times during this winter period. The model is in general agreement with this satellite data near the end of the run (YD 38-42) but the model underpredicts SSC in the first part of the run (YD 16-26). This could be due to the fact that the model was initialized at 0 gm^{-3} SSC, and takes a longer time period of 15-20 days to advect sediment from the source areas to A5.

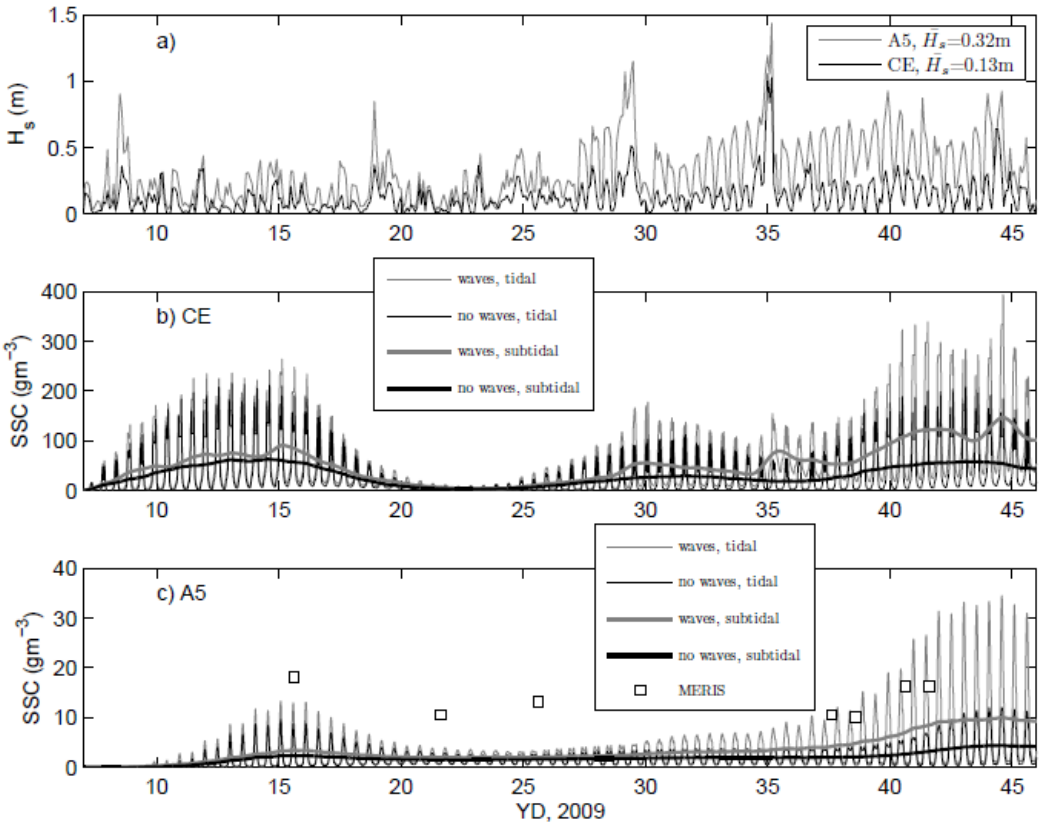

Figure 53: Significant wave height and surface suspended sediment concentration in the winter period in Minas Basin (A5) and the Cornwallis Estuary (CE): a) Hs; b) SSC at CE for the tide+wave and tide-only cases, with the lower frequency subtidal signals shown as thicker lines; c) SSC at A5 for both cases, and MERIS observations.

The time-series of H_s and SSC at A5 and CE for the summer period are presented in Figure 54. The effects of re-suspension by tidal currents alone are similar in summer and winter, by comparing YD 10-20 with YD 200-210. But the lighter winds in summer result in waves that are smaller than in winter, with average H_s of 0.14 m at A5 and 0.06 m at CE over the summer period. The predicted SSC is in general agreement with the SSC observed by the OBS sensor at CE from YD 224-226 but is lower than the SSC observed from YD 220-223. With approximately 200 m horizontal resolution, the present model grid does not adequately resolve the intertidal channels and refining the grid may lead to better predictions of SSC on the tidal flats. The model is in agreement with MERIS observations at A5, which range from 0.1-2.5 gm^{-3} at four times during this summer period. Overall, the model results from the winter and summer periods support the observation that the SSC is considerably lower in summer with the seasonal difference caused by greater wave re-suspension in winter.

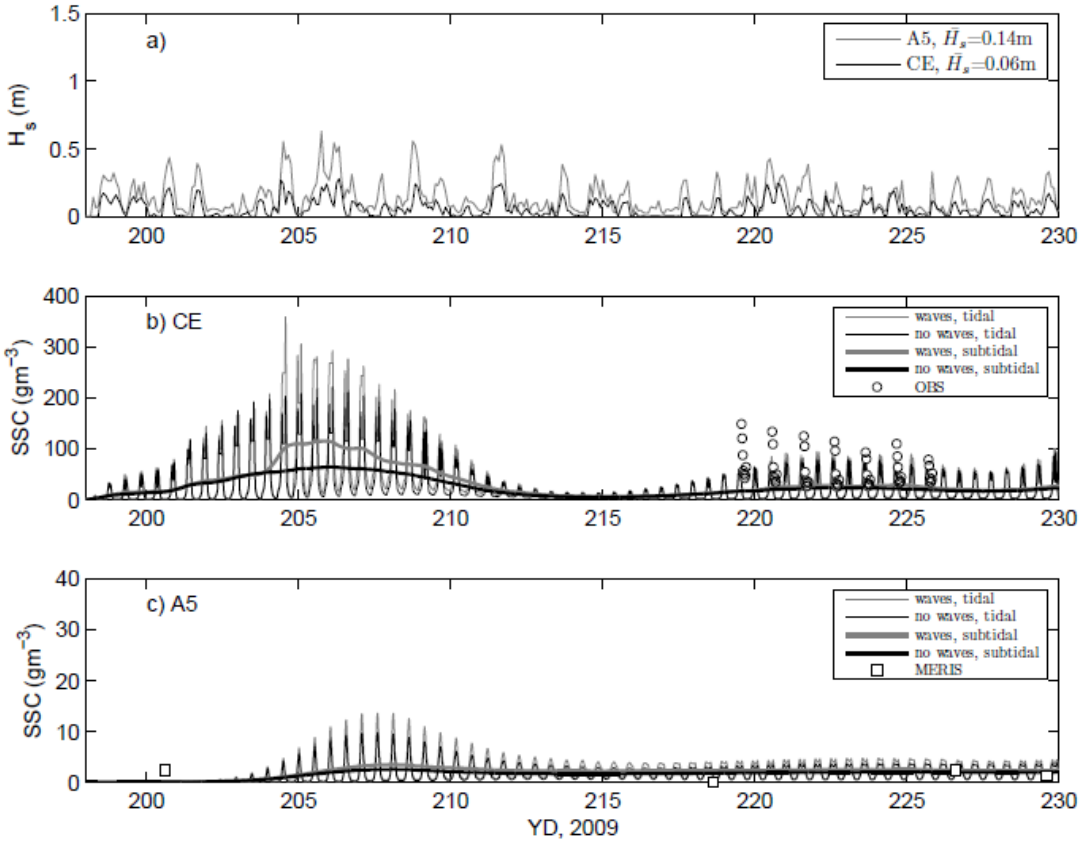

Figure 54: Significant wave height and surface suspended sediment concentration in the summer period in Minas Basin (A5) and the Cornwallis Estuary (CE): a) Hs; b) SSC at CE for the tide+wave and tide-only cases, with the lower frequency subtidal signals shown as thicker lines and with OBS observations; c) SSC at A5 for both cases, and MERIS observations.

Discussion

Winds and surface wave conditions in the Bay of Fundy have strong seasonal variability, according to climatological summaries described by Eid (1991) The wind and wave climate statistics were derived from ship-of-opportunity wind data, real-time buoy and rig data sets covering a time period from 1957-1988. Seasonal wind differences can be compared by defining U_{50} as the 50% wind speed exceedence values at the most frequent direction for each month. For winter conditions in the month of January U_{50} = 12.9 ms^{-1} from 315^o (blowing across Minas Basin from the NW). For summer conditions in by the month of July U_{50} = 7.7 ms^{-1} from 225^o (blowing along Minas Basin from the SW). This indicates that over longer timescales than the two periods evaluated in the present study, there is a significant seasonal change in mean wind speed and direction. As suggested by the results of the present study, the winter wind conditions generate significantly higher wave heights and suspended sediment concentrations in Minas Basin.

Since wave validation data were not available in Minas Basin, wave observations from satellite sensors were explored. In February, 2009, the Jason-1 satellite changed orbit such that the new orbit passed over Minas Basin (Figure 47). As an example, the altimeter recorded H_s values of 0.45 m near A5/A6 and 0.25 m on the tidal flats to the east of EB under 7-8 ms^{-1} westerly wind conditions on July 15 (YD 196.8). Since these data are limited to a few points in Minas Basin every 10.9 days, more detailed wave measurements from sensors deployed across the tidal flats would be ideal for future studies in macrotidal estuaries.

To investigate the role of waves further, we examined the model predictions from the winter period on the tidal flats at Evangeline Beach (EB) (see Figure 47), a wide tidal flat that is exposed to waves. The residuals between model predictions for the tide+wave and the tide-only cases are shown in Figure 55, indicating the difference by including the wave forcing on the sediment re-suspension response both on the tidal flats (EB) and in the deeper basin (A5). The waves increase the bed shear stress on the tidal flats by up to 5 Nm^{-2} during the YD 35 storm and have almost no influence on the bed in deeper areas. The increased shear stress due to waves on the flats increases the SSC both over short timescales of 1-2 days by up to 300 gm^{-3} and although some material settles following a storm, some remains in suspension and is transported by the tidal currents. This results in a net increase in concentration over time both on the flats up to 100-200 gm^{-3} and into the basin where, following a lag of several tidal cycles, the increase in SSC is up to 10-20 gm^{-3}. These results indicate the important influence of waves in combination with tidal currents on inducing re-suspension on the tidal flats, and the importance of tidal currents on transport of suspended materials to the deeper parts of the basin.

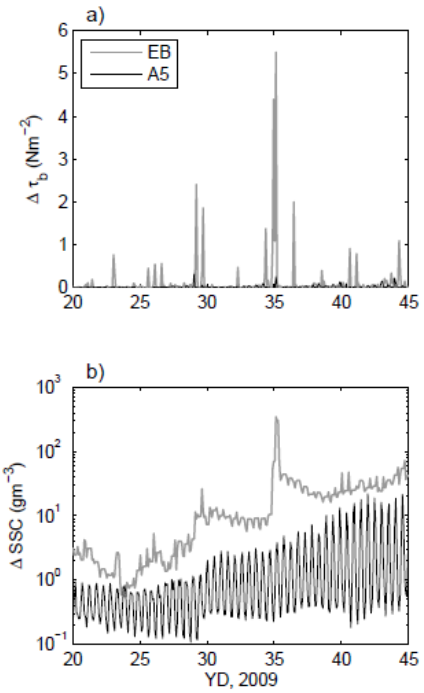

Figure 55: Differences between model predictions for the tide+wave and tide-only cases in winter at the Evangeline Beach tidal flats (EB) and central Minas Basin (A5) for: a) maximum bed shear stress, and b) surface suspended sediment concentration.

To validate the wave model, we have started further work to simulate the wave conditions during two periods in different seasons when a Nortek Aquadopp was deployed at Kingsport by BIO (data courtesy of Brent Law) and field measurements were being conducted within the tidal creek and on the marsh surface concurrently. These times, January and June 2013, are shown in Figure 56 and Figure 57. Additional model runs and data analyses will be completed in upcoming months. All simulations will be re-run using local wind observations at Kingsport. It is anticipated that these results will be submitted to the Journal of Geophysical Research Oceans in summer 2014.

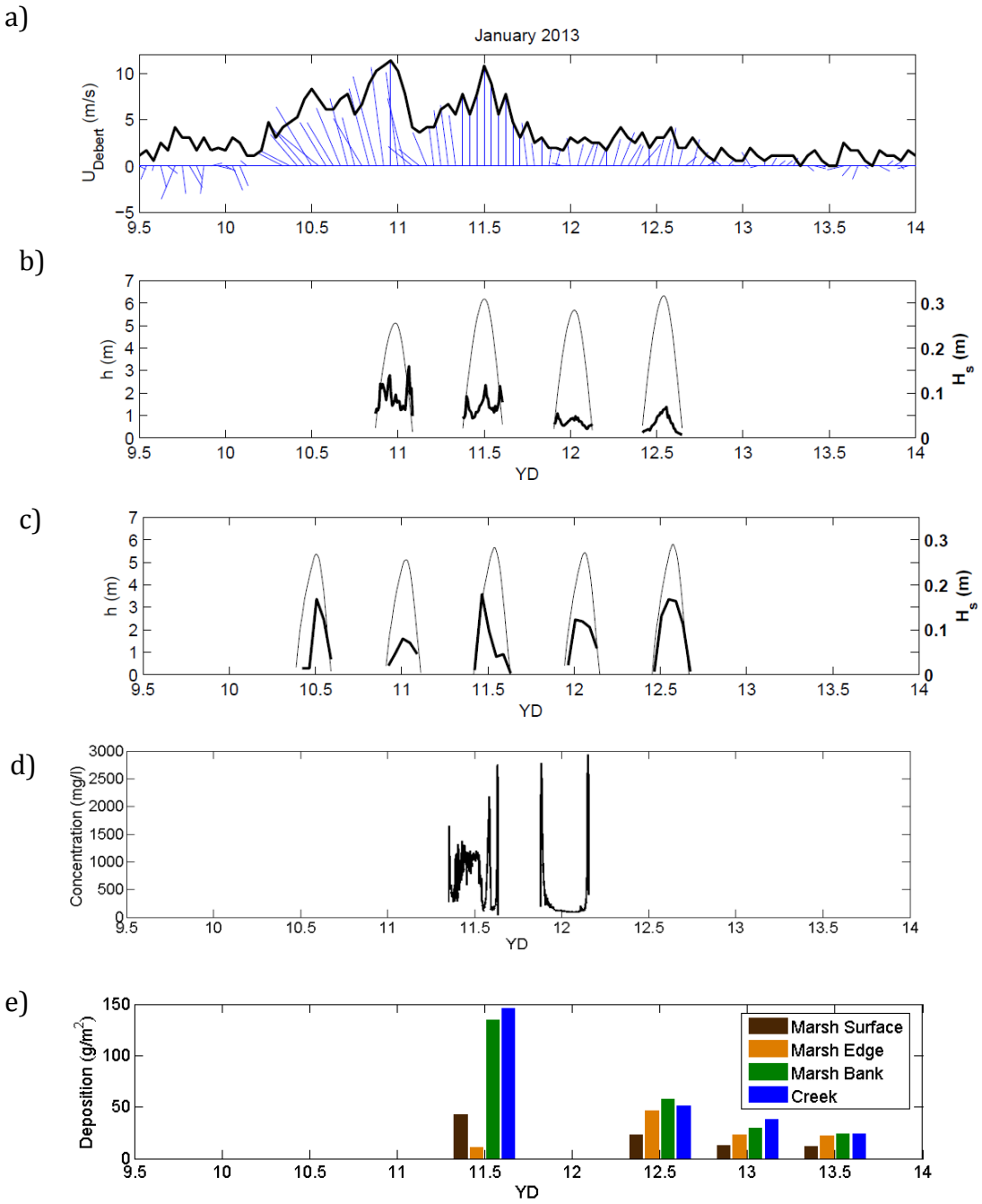

Figure 56: Water level and significant wave height observations and model predictions at Kingsport in January 2013, a) winds observed at Debert; b) observations; c) predictions; d) suspended sediment concentration from the RBR positioned in the creek (10 cm above the bed) and e) deposition from the traps during January deployment.

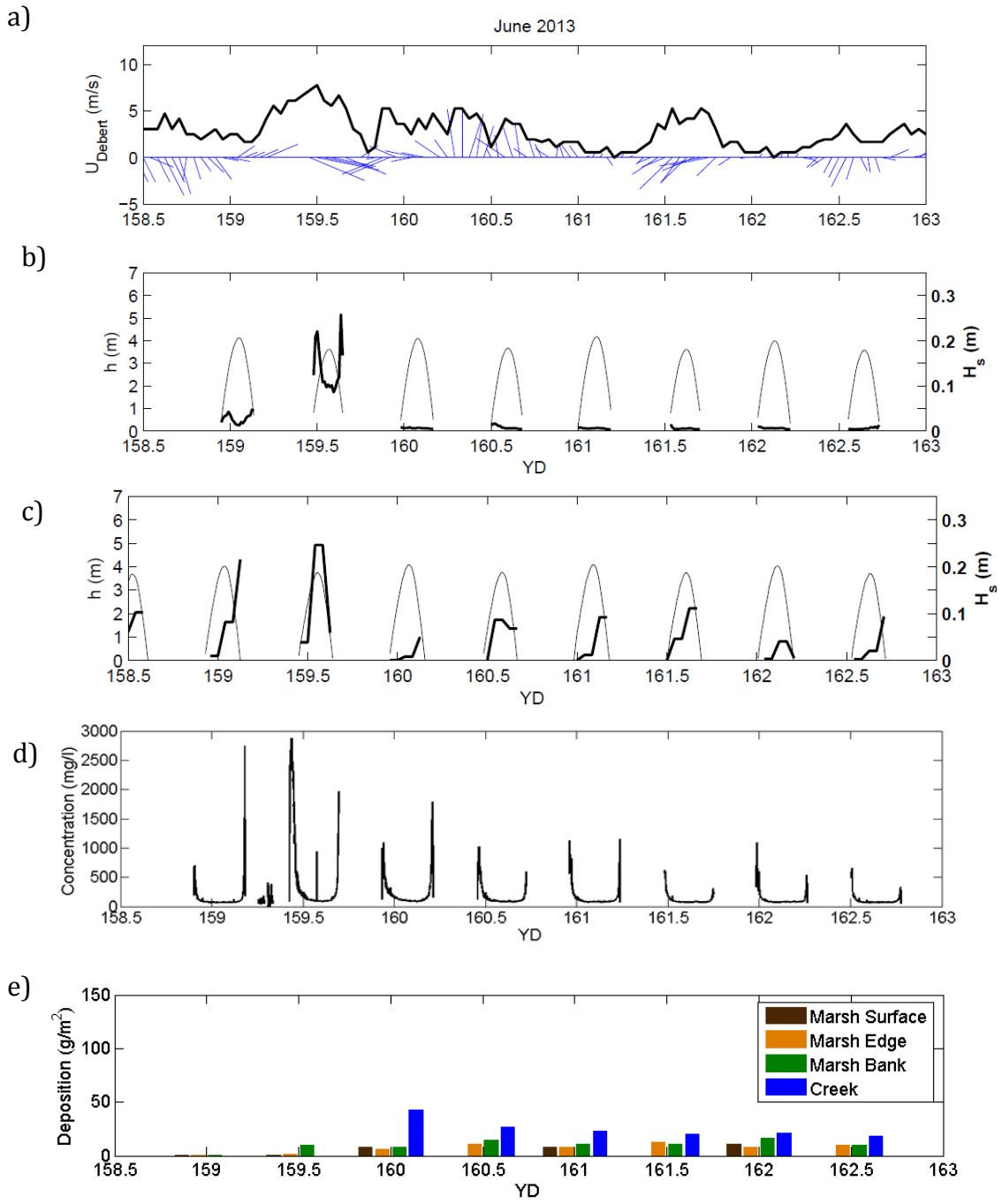

Figure 57: Water level and significant wave height observations and model predictions at Kingsport in June 2013, a) winds observed at Debert; b) observations; c) predictions; d) suspended sediment concentration from the RBR positioned in the creek (10 cm above the creek bed) and e) sediment deposition within the tidal creek and marsh surface. Passage of post tropical storm Andrea on June 8, 2013 included at YD 159 to 159.5.

CONCLUSIONS and RECOMMENDATIONS

This study significantly advances our understanding of the seasonal variability in intertidal ecomorphodynamics: the interaction and adjustment of topography, vegetation, fluid and hydrodynamic processes, morphologies and sequence of change dynamics involving the movement of sediment. In addition, it provides the first numerical model in the Bay of Fundy that effectively integrates near and far field hydrodynamic processes and serves as an important step towards three-dimensional modelling the full impacts of tidal energy extraction in these important ecosystems.

The three-dimensional high-resolution hydrodynamic model was used to simulate tidal currents and water levels in Minas Basin, calibrated using acoustic observations over multiple tidal cycles in the intertidal zone at Kingsport. The vegetation model scenarios were able to replicate similar flows observed over the marsh while the model scenarios without vegetation produced currents that were much stronger than observations, particularly at the two high marsh instruments. Currents during flood and ebb indicate good agreement between model and observations, and little influence of vegetation on flows in the creek with time series of tidal currents in the channel indicate a significant time lag between the time of high tide and reversal of flow with flood currents of up to 0.1 m/s, up to 2 hours after high tide. A simulation with turbines in Minas Passage was developed, representing the 2.5 GW of tidal power extraction which resulted in a 3.5% (0.2 m) tidal amplitude decrease within the Kingsport marsh, suggesting that turbines may have impacts on intertidal water level elevations and inundation times. This can have a potentially significant effect intertidal community structure (O'Laughlin et al., 2012). Future work will address sediment dynamics, tidal currents and surface waves in June 2013, corresponding to the dataset collected during the CCGS Hudson research cruise in Minas Basin.

In the field study, the seasonal control on deposition was strongest in the channel, seen at the creek and marsh bank stations. At these two stations, deposition and suspended sediment concentration were higher and this occurred in the winter, because of rapid deposition from high sediment supply. On the high marsh, the amount of sediment in floc form decreased and the seasonal control was less prominent. The period of October to February was the most active period in terms of high suspended sediment concentrations and sediment re-suspension. Episodic events with strong winds and heavy rainfall were effective at changing the grain size distribution of deposited sediment, this re-suspension also changing the characteristics of the sediment in suspension and therefore the incoming sediment on following tidal cycles. In addition, these episodic events appear to play an important role in maintaining equilibrium and a balanced annual sediment budget within the salt marsh tidal creek channel. However, this study also demonstrates that using only one scale of data (e.g. tidal cycle versus seasonal GIS digital elevation models) may lead to an inaccurate estimation of the sediment budget, and more accurate sediment budgets should be developed by integrating over broad spatial and temporal scales.

Minas Basin is protected from ocean swell and is regularly exposed to wind forcing in addition to strong tidal currents. Storm events may have major impacts on sediment transport, with winds that generate fetch-limited surface waves. The waves are important for re-suspension over the shallow tidal flats in the basin, by inducing wave orbital velocities at the seabed that in addition to tidal currents, create strong shear stresses on the bed. Surface waves are known to be important in causing re-suspension of bottom

sediments in other tidal estuaries (e.g., Ward, 1984), but previous modelling studies in the Bay of Fundy have not considered the effect of surface waves on sediment dynamics. The present work has focused on developing a coupled hydrodynamic-wave-sediment model to identify the roles of the surface waves and tidal currents that cause re-suspension and transport of suspended materials in Minas Basin. The results indicate that locally generated wind waves, can vary significantly over seasonal timescales, contributing up to 1-5 Nm^{-2} to the bottom shear stresses on tidal flats. The added shear stress due to waves leads to increased erosion of the tidal flats around the rim of the basin and increases the suspended sediment concentrations by 100-200 gm^{-3} in intertidal areas and by 10-20 gm^{-3} in deeper areas of the basin, representing a doubling in concentration in these areas. Predicting sediment transport processes in macrotidal environments is therefore dependant on accurate simulation of the combined tidal flow and surface wave field properties.

The results of this project add tremendous value to industry and government partners involved in the Fundy FORCE initiative, but also build on two successful OERA projects led by Danika van Proosdij in collaboration with Peter Smith (Bedford Institute of Oceanography) and Ryan Mulligan (Queen's University). In addition, it contributes directly to building local capacity in environmental effects monitoring and modelling by enriching our baseline data sets, adopting leading edge technologies and, providing "real world" training grounds for young scientists in Canada. This project was the foundation for training two bright young scholars at the Masters level: Emma Poirier at Saint Mary's University and Logan Ashall at Queen's University. An additional three undergraduate research assistants were trained in the field within the In_CoaST research unit. All team members have presented at regional, national and international conferences, disseminating our research widely and numerous papers will be submitted to referred journals in the near future. We have demonstrated that our team has taken full advantage of OERA's funding opportunity. By building on previous project investments and acquiring new data at key sites, we have developed a high resolution hydrodynamic model allowing us to integrate the field and model results that will help simulate anticipated TISEC installations while minimizing environmental impacts. Continuing work will develop a combined wave/current/sediment transport model that can be used to investigate the impacts of turbines on ecologically sensitive intertidal areas. Finally, the project results will benefit Nova Scotians by serving as a baseline that can be used to understand whether or not future changes associated with commercial scale tidal power generating structures in the Minas Passage are outside the range of natural variability of stressors that intertidal ecosystems have adequate resilience to respond.

DISSEMINATION and TECHNOLOGY TRANSFER

During this reporting period, sixteen papers were presented by both PIs and students at local, national and international conferences and five more are to be presented by June 2014. Two full papers, based on our previous OERA grant, were published in peer reviewed journals and an additional five should be submitted within the next six months. These new papers combine elements of all three OERA grants to van Proosdij and Mulligan, collectively and individually and will also draw upon knowledge gained from the companion field campaigns of Law (BIO) and Hill (Dal).

OERA[1] – van Proosdij
OERA[2] – Smith and Mulligan
OERA[3] – van Proosdij and Mulligan

Referred Journal Articles

- O'Laughlin, C., van Proosdij, D and Milligan, T. 2014. Flocculation and sediment deposition in a hypertidal creek. *Continental Shelf Research*. http://dx.doi.org/10.1016/j.csr.2014.02.012 [OERA[1]]

- O'Laughlin, C. and van Proosdij, D. 2012. Influence of varying tidal prism on hydrodynamics and sedimentary processes in a hypertidal salt marsh creek. *Earth Surface Processes and Landforms*, 38(5): 534-546. [OERA[1]]

Articles in Preparation for Submission

- Ashall, L.M, Mulligan, R.P., van Proosdij, D. and Poirier, E. Intertidal flows over a vegetated salt marsh surface and drainage channel network. In preparation for submission to *Estuarine, Coastal and Shelf Science, 2014.* [OERA[3]]

- Mulligan, R.P., Smith, P.C., Hill, P.S., and Tao, J. Tidal current and wind-wave controls on suspended sediment concentrations in a macrotidal basin. In preparation for submission to the *Journal of Geophysical Research Oceans, 2014*. [OERA[2,3]]

- Tao, J., Hill, P.S., and Mulligan, R.P. Seasonal variability of total suspended matter in Minas Basin, Bay of Fundy. In preparation for submission to *Estuarine, Coastal and Shelf Science, 2014.* [OERA[2]]

- Poirier, E., van Proosdij, D., Mulligan, R.P., and Ashall, L.M. Seasonal variability in the ecomorphodynamics of a macro-tidal salt marsh and tidal creek channel. In preparation for submission to *Geomorphology, 2014.* [OERA[3]]

- Poirier, E., van Proosdij, D., and Milligan, T. Seasonal sediment characteristics and flocculation in a tidal creek and salt marsh ecosystem. In preparation for submission to *Estuarine, Coastal and Shelf Science, 2014.* [OERA[3]]

Conference Proceedings

- Mulligan, R.P., Smith. P.C., Hill., P.S., Tao, J., and van Proosdij, D. Effects of tidal power generation on hydrodynamics and sediment processes in the upper Bay of Fundy. *Proc. Canadian Society for Civil Engineering Annual Conference*, Montreal, QC, May 2013. [OERA[2,3]]

Conference Presentations

- van Proosdij, D. ; Poirier, E; Milligan,T.; Mulligan,R.; O'Laughlin, C. and L. Ashall. Spatial Variability in Sediment Transport Processes in the Minas Basin: Implications for Modelling the Potential Effects of Tidal Energy Extraction. To be presented at Coastal Zone Canada, Halifax, NS, June 2014. [OERA [1,3]]

- Poirier, E., van Proosdij, D. and Milligan, T. Seasonal variability in sediment dynamics in a Bay of Fundy tidal channel and salt marsh. To be presented at Coastal Zone Canada, Halifax, NS, June 2014. [OERA[3]]

- Ashall, L.M., Mulligan, R.P., van Proosdij, D., and Law, B. Intertidal flows over vegetated salt marsh surface and drainage channel networks in a macro-tidal basin. To be presented to the Nova Scotia Energy R&D Conference, May 2014. [OERA[3]]

- van Proosdij, D., Mulligan, R.P., Poirier, E., Ashall, L., and Law, B. Bridging Spatial Gaps: Modelling the Relative Influence of Tidal Currents and Waves on Suspended Sediment Dynamics and Seasonal Sedimentation in Intertidal Ecosystems . To be presented at the Nova Scotia Energy R&D Conference, Halifax, NS, May 2014. [OERA[3]]

- Poirier, E., van Proosdij, D., Mulligan, R. and Milligan, T. Seasonal influences on sediment deposition and characteristics in a hypertidal salt marsh and tidal creek system. To be presented at the Nova Scotia Energy R&D Conference, Halifax, NS, May 2014. [OERA[3]]

- Ashall, L.M., Mulligan, R.P., van Proosdij, D., and Law, B. February 2014. Intertidal flows over vegetated salt marsh surface and drainage channel networks with cohesive sediments in a macro-tidal basin. Ocean Science Meeting 2014. Honolulu, HI. [OERA[3]]

- Poirier, E. and van Proosdij, D. November 2013. Seasonal variability in sedimentation and hydrodynamics within a hypertidal salt marsh creek. 22nd Biennial Conference of the Coastal and Estuarine Research Federation. San Diego, CA, USA. [OERA[3]]

- Poirier, E., van Proosdij, D. and Milligan, T. August 2013. Sedimentation and hydrodynamics in a Bay of Fundy tidal creek and salt marsh system. Canadian Association of Geographers. St. John's, NL. [OERA[3]]

- Mulligan, R.P., Smith, P.C., Hill, P.S., Toa, J., and van Proosdij, D. May - June 2013. Effects of tidal power generation on hydrodynamics and sediment processes in the Upper Bay of Fundy. 4th Speciality Conference on Coastal, Estuary and Offshore Engineering, Montreal, Que. [OERA[2,3]]

- Poirier, E., van Proosdij, D. and Milligan, T. May 2013. Seasonal sedimentation and hydrodynamics in a Bay of Fundy tidal creek and salt marsh system. Nova Scotia Tidal Energy Research Symposium and Forum, Wolfville, NS. [OERA[3]]

- van Proosdi, D., O'Laughlin, C., Poirier, E., Mulligan, R. and Ashall, L. May 2013. *Intertidal Sediment Dynamics: Challenges, Lessons Learned and Potential Impacts of Tidal Power Development*. Nova Scotia Energy Research and Development Forum, Wolfville, NS. [OERA[3]]

- Tao, J., Hill, P.S., and Mulligan, R.P. May 2013. Seasonal Variability of Total Suspended Matter in Minas Basin, Bay of Fundy. Proceedings on the Nova Scotia Tidal Energy Research Symposium, Wolfville, NS. [OERA[2]]

- Ashall, L.M., Mulligan, R.P., and van Proosdij, D. December 2012. A High Resolution Sediment Model of an Intertidal Estuary in the Bay of Fundy. American Geophysical Union (AGU) Fall Meeting, San Francisco, CA. [OERA[3]]

- Poirier, E., van Proosdij, D., and Mulligan, R.P. December 2012. The Influence of Tidal Flow and Channel Order on Sedimentation and Hydrodynamics in Two Macrotidal Creeks in the Bay of Fundy. American Geophysical Union (AGU) Fall Meeting, San Francisco, CA. [OERA [1,3]]

- Poirier, E., van Proosdij, D. and Mulligan, R.P. October 2012. A comparison of two Bay of Fundy tidal creeks: the effect of channel form on their sedimentation rates and hydrodynamics. Atlantic Division of the Canadian Association of Geographers. Halifax, NS. [OERA[1.3]]

- Tao, J., Hill, P.S., and Mulligan, R.P. May 2012. Seasonal variability of total suspended matter in Minas Basin, the Bay of Fundy. Canadian Meteorological and Oceanographic Society (CMOS) Annual Congress, Montreal, QC [OERA[2]]

- Mulligan, R.P., Smith, P.C., Hill, P.S., Tao, J., Wu, Y., Bugden, G., van Proosdij, D. February 2012. Suspended sediment processes in Minas Basin, the Bay of Fundy. Ocean Sciences 2012 Meeting, Salt Lake City, UT. [OERA[2,3]]

- van Proosdij, D., O'Laughlin, C., Milligan, T. and Mulligan, R.P. November 2011. Potential far field effects of tidal energy extraction on intertidal ecosystems of the Bay of Fundy. Conference of the Coastal and Estuarine Research Federation, Daytona Beach, FL. [OERA[1,2,3]]

- van Proosdij, D., O'Laughlin, C., Milligan, T. and Mulligan, R.P. September 2011. Far field effects of tidal energy extraction on intertidal ecosystems of the Bay of Fundy, 9th Bay of Fundy Science Workshop, Bay of Fundy Ecosystem Partnership, Saint John, NB. [OERA[1,2,3]]

Student Presentations

- Ashall, L.M. December 2012. Tidal flows in the Bay of Fundy, Queen's U-U Ottawa Hydrotechnical conference, Kingston, ON. [OERA[3]]

- Ashall. L.M. May 2013. Tidal currents in Minas Basin, Environmental Hydraulics Seminars, Queen's University, Kinston ON. [OERA[3]]

- Ashall, L.M. December 2013. A High Resolution Model of the Bay of Fundy, Queen's U-U Ottawa Hydrotechnical conference, Ottawa, ON. [OERA[3]]

- Ashall, L.M., Tidal flows over vegetation and drainage channel networks in a macro-tidal basin, To be

REFERENCES

Amos, C., and Long, B. 1980. The sedimentary character of the Minas Basin, Bay of Fundy, in Proc. Coastlines Canada Conf., Halifax, NS, edited by S. McCann, GSC 80-10.

Amos, C., G. Daborn, H. Christian, Atkinson, A., and Robertson, A. 1992. In situ erosion measurements on fine-grained sediments from the Bay of Fundy. *Marine Geology,* 108: 175–196.

Augustin, L.N., Irish, J.L., and Lynett, P. 2008. Laboratory and Numerical Studies of Wave Damping by Emergent and Near-Emergent Wetland Vegetation. *Journal of Coastal Engineering*, 56: 332-340.

Battjes, J., and Janssen, J. 1978. Energy loss and set-up due to breaking of random waves. ASCE, Proc. Intl. Conf. on Coastal Eng. Hamburg, Germany: 569-587.

Biron, P.M., Robson, C. Lapointe, M.F. and Gaskin, S.J. 2004. Comparing different methods of bed shear stress estimates in simple and complex flow fields. *Earth Surface Processes and Landforms*, 29: 1403-1415.

Blott, S.J. and Pye, K. 2001. GRADISTAT: a grain size distribution and statistics package for the analysis of unconsolidated sediments. *Earth Surface Processes and Landforms*, 26: 1237-1248.

Booij, N., Ris, R., and Holthuijsen, L. 1999. A third-generation wave model for coastal regions, 1. model description and validation. *Journal of Geophysical Research*, 104 (4): 7649–7666.

Borsje, B., de Vries, M.B., Hulscher, S., and de Boer, G. 2008. Modeling large-scale cohesive sediment transport affected by small-scale biological activity. *Estuarine, Coastal and Shelf Science*, *78*: 468–480.

Brown, M., Mulligan, R., and Miller, R. Modeling the transport of freshwater and dissolved organic carbon in the Neuse River Estuary, NC, USA following Hurricane Irene (2011). *Estuarine, Coastal and Shelf Sci.*, *submitted*, 2013.

Coco, G., Zhou, Z., van Maanen, B., Olabarrieta, M., Tinoco, R. and Townend, L. 2013. Morphodynamics of tidal networks: Advances and challenges. *Marine Geology*, 346: 1-16.

Curran, K.J., Hill, P.S., Schell, T.M., Milligan, T.G. and Piper, D.J.W. 2004. Inferring the mass fraction of floc-deposited mud: application to fine-grained turbidites. *Sedimentology*, 51: 927-944.

deGelleke, L. Hill, P.S., Keinast, M. and Piper, D.J.W. 2013. Sediment dynamics during Heinrich event H1 inferred from grain size. *Marine Geology*, 336:160-169.

Dijkstra, J. T., and Uittenbogaard, R.E. 2010. Modeling the interaction between flow and highly flexible aquatic vegetation. *Water Resources Research*, 46, W12547, doi: 10.1029/2010WR009246.

Doerffer, R., Sorensen, K., and Aiken, J. 1999. MERIS potential for coastal zone applications, *International Journal of Remote Sensing*, *20* (9): 1809–1818.

Dupont, F., Hannah, C., Greenberg, D., Cherniawsky, J., and Naimie, C. 2002. Modelling system for tides, *Tech. Rep. 221(vii)*, Can. Tech. Rep. Hydrogr. Ocean Sci.

Dupont, F., Hannah, C., Greenberg, D. 2005. Modelling the Sea Level in the Upper Bay of Fundy. *Atmosphere-Ocean,* 43(1): 33-47.

Eid, B., Dunlap, E., Henschel, M., and Trask, J. 1991. Wind and wave climate atlas, volume 1: the east coast of Canada. *Tech. Rep.* TP 10820E, Transport Canada.

Elias, E., Gelfenbaum, G., and Van der Westhuysen, A. 2012. Validation of a coupled wave-flow model in a high-energy setting: The mouth of the Columbia River. *Journal of Geophysical Research*, 117 (C9).

Fagherazzi, S., Palermo, C., Rulli, M., Carniello, L., and Defina, A. 2007. Wind waves in shallow microtidal basins and the dynamic equilibrium of tidal flats. *Journal of Geophysical Research,* 112 (F2).

Graham, J. 2012. Consideration for salt marsh restoration design in a hypertidal estuary. Master's thesis, Saint Mary's University. 120pp.

Hartog, W.. Benedet, M.L., Walstra, D.-J.R., Koningsveld, M.v., Stive, M.J.F., and Finkl, C.W. 2008. Mechanisms that influence the performance of beach nourishment: A case study in Delray Beach, Florida, U.S.A. *Journal of Coastal Research*, 24 (5): 1304–1319.

Hasselmann, K., Barnett, T.P., Bouws, E., Carlson, H., Cartwright, D.E., Enke, K., Ewing, J.A., Gienapp, H., Hasselmann, D.E., Kruseman, P., Meerburg, A., Muller, P., Olbers, D.J., Ritcher, K., Sell, W., and Walden, H. 1973. Measurements of wind-wave growth and swell decay during the Joint North Sea Wave Project (JONSWAP). *Tech. Rep*. A(8)12, Dtsch. Hydrogr. Z.

Hu, K., Ding, P., Wang, Z., and Yang, S. 2009. A 2D/3D hydrodynamic and sediment transport model for the Yangtze Estuary, China. *Journal of Marine Systems*, 77 (1): 114–136.

Karsten, R., McMillian, J., and Lickley, M. 2008. Assessment of tidal current energy in Minas Passage, Bay of Fundy, Proc. IMechE, Part A: J Power Energy, 222, 493507.

Kim, S.-C., Friedrichs, C.T., Maa, J.P.-Y. and Wright, L.D. 2000. Estimating bottom stress in tidal boundary layer from acoustic Doppler velocimeter data. *Journal of Hydraulic Engineering*, 126(6): 399-406.

Kranck, K. and Milligan, T.G. 1991. Grain size in oceanography. In Syvitski, J.P.M.(ed) Principles, Methods and Application of Particle Size Analysis, Cambridge University Press, New York, 322-345.

Kranck, K., Smith, P.C. and Milligan, T.G. 1996a. Grain-size characteristics of fine-grained unflocculated sediments I: 'one-round' distributions. *Sedimentology*, 43: 589-596.

Kranck, K., Smith, P.C. and Milligan, T.G. 1996b. Grain-size characteristics of fine-grained unflocculated sediment II: 'multi-round' distributions. *Sedimentology*, 43: 597-606.

Kusters, L.E.M., 2003. Paulina vegetation model:current attenuation by salt marsh vegetation. TU Delft, Civil Engineering and Geosciences, MSc Thesis, 148 p.

Lane, S.N., Biron, P.M., Bradbrook, K.F., Butler, J.B., Chandler, J.H., Crowell, M.D., McLelland, S.J., Richards, K.S., and Roy, A.G. 1998. Three dimensional measurement of river channel flow processes using acoustic Doppler velocimetry. *Earth Surface Processes and Landforms*, 23: 1247-1267.

Leonard, L.A. and Luther, M.E. 1995. Flow hydrodynamics in tidal marsh canopies. *Limnology and Oceanography,* 40(8): 1474-1484.

Leorri, E., Mulligan, R., Mallinson, D., and Cearret, A. 2011. Sea-level rise and local tidal range changes in coastal embayments: An added complexity in developing reliable sea-level index points. *Journal of Integrated Coastal Zone Management*, 11 (3): 307–314.

Lesser, G., Roelvink, J., van Kester, J., and Stelling, G. 2004. Development and validation of a three-dimensional morphological model. *Coastal Engineering*, 51: 883–915.

Ménard, Y., Fu, L.-L., Escudier, P., Parisot, F., Perbos, J., Vincent, P., Desai, S., Haines, B., and Kunstmann, G. 2003. The Jason-1 Mission Special Issue: Jason-1 calibration/validation. *Marine Geodesy,* 26 (3-4): 131–146.

Milligan, T.G., Hill, P.S. and Law, B.A. 2007. Flocculation and the loss of sediment from the Po River plume. *Continental Shelf Research*, 27: 309-321.

Mulligan, R., W. Perrie, and Solomon, S. 2010. Dynamics of the Mackenzie River plume on the inner Beaufort shelf during an open water period in summer. *Estuarine, Coastal and Shelf Science*, 89 (3): 214–220.

Mulligan, R., Smith, P., Hill, P., Tao, J., and van Proosdij, D. 2013. Effects of tidal power generation on hydrodynamics and sediment processes in the upper Bay of Fundy, in Proc. Can. Soc. Civil. Eng., Montreal, QC.

Murphy, S. and Voulgaris, G. 2006. Identifying the role of tides, rainfall and seasonality in marsh sedimentation using long-term suspended sediment concentration data. *Marine Geology*, 227: 31-50.

Nardin, W., and Fagherazzi, S. 2012. The effect of wind waves on the development of river mouth bars. *Geophysical Research Letters,* 39 (12).

Neumeier, U., and Amos, C.L. 2006. The influence of vegetation on turbulence and flow velocities in European salt-marshes. *Sedimentology,* 53: 259-277.

Pope, N.D., Widdows, J., and Brinsley, M.D. 2006. Estimation of Bed Shear Stress using the Turbulent Kinetic Energy Approach – A Comparison of Annular Flume and Field Data. *Continental Shelf Research*, 26: 959-970.

Reniers, A. J. H. M., Roelvink, J.A., and Thornton, E.B. 2004. Morphodynamic modeling of an embayed beach under wave group forcing. *Journal of Geophysical Research*, 109 (C1).

Roy, A.G., Biron, P., and de Serres, B. 1996. On the necessity of applying a rotation to instantaneous velocity measurements in river flows. *Earth Surface Processes and Landforms*, 21: 817-827.

Shaw, J., Todd, B., Li, M., and Wu, Y. 2012. Anatomy of the tidal scour system at Minas Passage, Bay of Fundy, Canada. *Marine Geology,* 323-325: 123–134.

Sheldon, R.W. 1972. Size separation of marine seston by membrane and glass-fiber filters. *Limnology and Oceanography*, 17: 464-498.

Sheldon, R.W. and Sutcliffe, W.H. 1969. Retention of marine particles by screens and filters. *Limnology and Oceanography*, 14(3):441-444.

Smith, P and Mulligan, R. 2010. Impacts of Tidal Energy Extraction on Sediment Dynamics in Minas Basin, Bay of Fundy, NS. Interim Report III prepared for OEER.

Soulsby, R.L., 1983. The bottom boundary layer of shelf seas. *Elsevier Oceanography Series,* 35:189-266.

Soulsby, R., Hamm, L., Klopman, G., Myrhaug, D., Simons, R., and Thomas, G. 1993. Wave-current interaction within and outside the bottom boundary layer. *Coastal Engineering*, 21 (1-3): 41-69.

Tao, J. 2103. Temporal autocorrelation analysis to identify the dominant time scales of suspended sediment variability in Minas Basin, MSc Thesis, Dalhousie University.

Temmerman, S., Bouma, T., Govers, G., Wang, Z., De Vries, M., and Herman, P. 2005. Impact of vegetation on flow routing and sedimentation patterns: Three-dimensional modeling for a tidal marsh. *Journal of Geophysical Research, 110* (F4).

van Proosdij, D. 2001. Spatial and temporal controls on the sediment budget of a macrotidal saltmarsh. PhD Thesis. Faculty of Graduate Studies, University of Guelph.

van Proosdij, D., Lundholm, J., Neatt, N., Bowron, T., and Graham, J. 2010. Ecological Re-engineering of a Freshwater Impoundment for a Salt Marsh Restoration in a Hypertidal System. *Journal of Ecological Engineering,* 36(10):1314-1332. DOI:10.1016/j.ecoleng.2010.06.008

Voulgaris, G., and Meyers, S.T. 2004. Temporal variability of hydrodynamics, sediment concentration and sediment settling velocity in a tidal creek. *Continental Shelf Research*, 24: 1659-1683.

van Rijn, L.C., 2007. Unified view of sediment transport by currents and waves. ii: Suspended transport. *Journal of Hydraulic Engineering*, *133* (6): 668–689.

Ward, L., Kemp, W., and Boynton, W. 1984. The influence of waves and seagrass communities on suspended particulates in an estuarine embayment, *Marine Geology*, *59*: 85–103.

Whitford, J. 2008. Background Report for the Fundy Tidal Energy Strategic Environmental Assessment. OEER Project #1028476, 21pp.

Wu, Y., Chaffey, J., Greenberg, D.A., Colbo, K., and Smith, P.C. 2011. Tidally-induced sediment transport patterns in the upper Bay of Fundy: a numerical study. *Continental Shelf Research,* 31 (19): 2041–2053.

Yang, S.L., Li, H., Ysebaert, T., Bouma, T.J., Zhang, W.X., Wang, Y.Y., Li, P., Li, M. and Ding, P.X. 2008. Spatial and temporal variations in sediment grain size in tidal wetlands, Yangtze Delta: On the role of physical and biotic controls. *Estuarine, Coastal and Shelf Science*, 77: 657-671.

APPENDIX A

Geographical Coordinates of Sampling Stations

Station	Latitude	Longitude	Z (CGVD28)	Instruments Deployed
Marsh Surface	45.156545	-64.371856	5.888	ADV, OBS, traps, bottles
Marsh Edge	45.156452	-64.371781	5.473	ADV, traps, bottles
Marsh Bank	45.156390	-64.371732	3.672	ADV, OBS, ISCO, traps, bottles
Creek Thalweg	45.156276	-64.371601	-0.507	ADCP, RBR, traps, bottles

APPENDIX B
Seasonal Divisions of Deployments

Spring category tides

Tide	CHS Height (ft)	ADCP Max Height (m)	V1	V2	V3	ISCO	ADCP	RBR	Level Logger	M1 Traps	M2 Traps	M3 Traps	C4 Traps	Daily Scrapes
May5am 2012	47.8	7.9	✓	✓	×	×	✓	✓	✓	✓	✓	✓	✓	✓
May5pm 2012	47.0	7.6	✓	✓	✓	✓	⊗	✓	✓	✓	✓	✓	✓	
May6am 2012	49.0	8.3	✓	✓	✓	✓	✓	✓	✓	✓	✓	✓	✓	✓
May6pm 2012	47.7	7.8	✓	✓	✓	✓	✓	✓	✓	✓	✓	✓	✓	
May7am 2012	49.5	8.4	✓	✓	✓	×	✓	✓	✓	⊗	⊗	⊗	⊗	✓
May7pm 2012	47.7	7.9	✓	✓	✓	✓	✓	✓	✓	✓	✓	✓	✓	
May8am 2012	49.4	8.4	✓	✓	✓	✓	✓	✓	✓	✓	✓	✓	✓	✓
May8pm 2012	47.2	7.8	✓	✓	✓	✓	✓	✓	✓	✓	✓	✓	✓	
May9am 2012	48.5	8.1	✓	✓	✓	✓	✓	✓	✓	⊗	⊗	⊗	⊗	✓
May25am 2013	48.5	8.0	✓	✓	✓	✓	✓	✓	✓	⊗	⊗	⊗	⊗	✓
May25pm 2013	46.9	7.5	✓	✓	✓	⊗	✓	✓	✓	✓	✓	✓	✓	
May26am 2013	49.2	8.3	✓	✓	✓	✓	✓	✓	✓	⊗	⊗	⊗	⊗	✓
May26pm 2013	47.3	7.7	✓	✓	✓	✓	✓	✓	✓	✓	✓	✓	✓	
May27am 2013	49.2		✓	✓	✓	✓	×	✓	✓	✓	✓	✓	✓	✓
May27pm 2013	47.1		✓	✓	✓	✓	×	✓	✓	✓	✓	✓	✓	
May28am 2013	48.6	8.1	✓	✓	✓	✓	✓	✓	✓	✓	✓	✓	✓	✓
Jun8am 2013	44.3	6.8	✓	✓	✓	✓	✓	✓	✓	⊗	⊗	⊗	⊗	✓
Jun8pm 2013	42.3	6.4	×	✓	✓	✓	✓	✓	×	⊗	⊗	⊗	⊗	
Jun9am 2013	44.6	6.8	✓	✓	✓	✓	✓	✓	✓	⊗	⊗	⊗	⊗	✓
Jun9pm 2013	42.3	6.3	×	✓	✓	✓	✓	✓	×	×	✓	✓	✓	
Jun10am 2013	44.3	6.9	✓	✓	✓	✓	✓	✓	✓	✓	✓	✓	✓	✓
Jun10pm 2013	42.3	6.3	×	✓	✓	✓	✓	✓	×	×	✓	✓	✓	
Jun11am 2013	44.0	6.7	✓	✓	✓	✓	✓	✓	✓	✓	✓	✓	✓	✓
Jun11pm 2013	42.0	6.3	×	✓	✓	✓	⊗	✓	×	×	✓	✓	✓	
Jun12am 2013	43.6	6.5	✓	✓	✓	✓	✓	✓	✓	⊗	⊗	⊗	⊗	✓

Summer Category Tides

Tide	CHS Height (ft)	ADCP Max Height (m)	V1	V2	V3	ISCO	ADCP	RBR	Level Logger	M1 Traps	M2 Traps	M3 Traps	C4 Traps	Daily Scrapes
July4am 2012	47.9	8.1	✓	✓	✓	✓	✓	✓	✓	✓	✓	✓	✓	✓
July4pm 2012	46.0	7.5	✓	✓	✓	✓	✓	✓	✓	✓	✓	✓	✓	✓
July5am 2012	48.1	8.1	✓	✓	✓	✓	✓	✓	✓	⊗	⊗	⊗	⊗	
July5pm 2012	46.2	7.5	✓	✓	✓	✓	✓	✓	✓	✓	✓	✓	✓	×
July6am 2012	47.7	7.8	✓	✓	✓	✓	✓	✓	✓	⊗	⊗	⊗	⊗	
Aug4am 2012	47.3	7.8	✓	×	✓	✓	✓	✓	✓	✓	✓	✓	✓	✓
Aug4pm 2012	46.2	7.4	✓	×	✓	✓	✓	✓	✓	✓	✓	✓	✓	✓
Aug5am 2012	46.7	7.5	✓	×	✓	✓	✓	✓	✓	✓	✓	✓	✓	
Sep17am 2012	47.6	7.6	×	✓	✓	✓	✓	✓	✓	✓	✓	✓	✓	✓
Sep17pm 2012	48.4	7.8	×	✓	✓	✓	✓	✓	✓	✓	✓	✓	✓	✓
Sep18am 2012	48.2		✓	✓	✓	✓	×	✓	✓	✓	✓	✓	✓	
Sep18pm 2012	49.0	8.0	✓	✓	✓	✓	✓	✓	✓	✓	✓	✓	✓	✓
Sep19am 2012	48.0	7.6	✓	✓	✓	✓	✓	✓	✓	✓	✓	✓	✓	
Sep19pm 2012	48.8	7.9	✓	✓	✓	✓	✓	✓	✓	⊗	⊗	⊗	⊗	✓

Sep20am 2012	47.2	7.4	✓	✓	✓	✓	✓	✓	✓	✓	✓	✓	✓	
Aug5am 2012	46.7	7.5	✓	×	✓	✓	✓	✓	✓	✓	✓	✓	✓	
Sep17am 2012	47.6	7.6	×	✓	✓	✓	✓	✓	✓	✓	✓	✓	✓	✓
Sep17pm 2012	48.4	7.8	×	✓	✓	✓	✓	✓	✓	✓	✓	✓	✓	✓
Sep18am 2012	48.2		✓	✓	✓	✓	×	✓	✓	✓	✓	✓	✓	
Sep18pm 2012	49.0	8.0	✓	✓	✓	✓	✓	✓	✓	✓	✓	✓	✓	✓
Sep19am 2012	48.0	7.6	✓	✓	✓	✓	✓	✓	✓	✓	✓	✓	✓	
Sep19pm 2012	48.8	7.9	✓	✓	✓	✓	✓	✓	✓	⊗	⊗	⊗	⊗	✓
Sep20am 2012	47.2	7.4	✓	✓	✓	✓	✓	✓	✓	✓	✓	✓	✓	

'Winter' Category Tides:

Tide	CHS Height (ft)	ADCP Max Height (m)	V1	V2	V3	ISCO	ADCP	RBR	Level Logger	M1 Traps	M2 Traps	M3 Traps	C4 Traps	Daily Scrapes
Nov14am 2012	46.9	7.6	✓	✓	✓	✓	✓	✓	×	⊗	⊗	⊗	⊗	✓
Nov14pm 2012	49.1	8.3	✓	✓	✓	×	✓	✓	×	⊗	⊗	⊗	⊗	
Nov15am 2012	47.3	7.8	✓	✓	✓	✓	✓	✓	×	✓	✓	✓	✓	✓
Nov15pm 2012	49.3	8.3	✓	✓	✓	✓	✓	✓	×	✓	✓	✓	✓	
Nov16am 2012	47.2	7.8	✓	✓	✓	✓	✓	✓	×	✓	✓	✓	✓	✓
Nov16pm 2012	48.9	8.2	✓	✓	✓	✓	✓	✓	×	✓	✓	✓	✓	
Nov17am 2012	46.6	7.6	✓	✓	✓	✓	✓	✓	×	✓	✓	✓	✓	✓
Jan11pm 2013	48.0	8.3	✓	✓	✓	✓	✓	✓	×	✓	✓	✓	✓	✓
Jan12pm 2013	48.5	8.4	✓	✓	✓	✓	✓	×	×	✓	✓	✓	✓	✓
Jan13am 2013	46.9	7.9	✓	✓	✓	×	✓	×	×	✓	✓	✓	✓	✓
Jan13pm 2013	48.5	8.3	✓	✓	✓	✓	✓	×	×	✓	✓	✓	✓	
Jan14am 2013	47.0	7.9	✓	✓	✓	×	✓	×	×	×	×	×	×	✓
Jan14pm 2013	48.1	8.1	✓	✓	✓	✓	✓	×	×	✓	✓	✓	✓	
Jan15am 2013	46.6	7.6	✓	✓	✓	✓	✓	×	×	✓	✓	✓	✓	✓
Mar27pm 2013	46.7	7.7	✓	✓	✓	✓	✓	✓	✓	✓	✓	✓	✓	✓
Mar28am 2013	47.7	7.9	✓	✓	✓	✓	✓	✓	✓	✓	✓	✓	✓	✓
Mar28pm 2013	47.6	7.9	✓	✓	✓	✓	✓	✓	✓	✓	✓	✓	✓	
Mar29am 2013	48.6	8.2	✓	✓	✓	✓	✓	✓	✓	✓	✓	✓	✓	✓
Mar29pm 2013	47.8	8.0	✓	✓	✓	✓	✓	✓	✓	✓	✓	✓	✓	
Mar30am 2013	48.8	8.3	✓	✓	✓	✓	✓	✓	✓	✓	✓	✓	✓	✓
Mar30pm 2013	47.3	7.8	✓	✓	✓	✓	✓	✓	✓	✓	✓	✓	✓	
Mar31am 2013	48.2	8.1	✓	✓	✓	✓	✓	✓	✓	✓	✓	✓	✓	✓

APPENDIX C

Sediment Characteristics of Daily Scrape Samples

	Folk & Ward Method (µm)						Inverse Floc Model Method			
	Mean	Sorting	Skewness	Kurtosis	d50 (µm)	d90 (µm)	Floc Fraction	Floc Limit (µm)	Source Slope	Roll-off diameter (µm)
May4-M1	7.902	2.758	-0.132	0.914	8.631	27.18	0.78	21	0.54	17
May4-M2	8.196	2.795	-0.139	0.899	8.973	28.56	0.72	18	0.52	16
May4-M3	6.451	2.606	-0.123	0.876	7.061	21.04	0.85	24	0.53	16
May4-C4	7.545	2.793	-0.164	0.910	8.570	26.34	0.79	21	0.53	17
May5-M1	8.811	2.910	-0.119	0.853	9.410	33.08	0.7	18	0.52	17
May5-M2	7.582	2.833	-0.150	0.902	8.529	27.09	0.71	16	0.52	14
May5-M3	8.946	2.845	-0.118	0.827	9.584	33.12	0.77	24	0.53	20
May5-C4	9.857	2.977	-0.205	0.840	11.62	36.09	0.78	28	0.44	27
May6-M1	10.84	3.346	-0.117	0.874	12.13	47.26	0.8	37	0.38	33
May6-M2	8.941	2.909	-0.086	0.858	9.514	33.79	0.74	21	0.55	18
May6-M3	10.92	3.055	-0.176	0.843	12.32	38.56	0.82	37	0.5	31
May6-C4	10.74	3.084	-0.178	0.837	12.17	38.60	0.82	37	0.46	31
May7-M1	8.895	2.941	-0.123	0.834	9.526	33.82	0.83	32	0.44	25
May7-M2	9.749	2.965	-0.176	0.834	11.17	35.98	0.84	37	0.45	29
May7-M3	10.80	3.074	-0.170	0.833	12.14	38.53	0.82	37	0.46	32
May7-C4	13.11	3.088	-0.245	0.874	15.69	47.61	0.77	37	0.49	37
May8-M1	6.453	2.803	-0.061	0.862	6.732	22.48	0.73	14	0.31	14
May8-M2	7.639	2.899	-0.140	0.899	8.590	28.35	0.84	28	0.44	21
May8-M3	6.855	2.739	-0.092	0.826	7.254	22.49	0.74	16	0.48	14
May8-C4	7.259	2.850	-0.160	0.829	8.271	26.18	0.76	18	0.37	18
May9-M1	8.332	2.795	-0.160	0.862	9.305	28.70	0.68	16	0.5	17
May9-M2	7.007	2.830	-0.065	0.858	7.392	26.09	0.76	18	0.48	15
May9-M3	7.527	2.847	-0.133	0.928	8.416	27.61	0.81	24	0.52	17
May9-C4	10.79	3.228	-0.183	0.867	12.26	44.22	0.67	21	0.37	25
July4-M1	8.642	2.924	-0.106	0.841	9.130	33.15	0.82	28	0.45	22
July4-M2	9.753	3.005	-0.165	0.829	11.12	36.69	0.84	37	0.43	29
July4-M3	10.27	2.933	-0.200	0.852	11.94	36.50	0.77	28	0.53	25
July4-C4	12.75	3.030	-0.274	0.849	15.42	45.73	0.71	28	0.44	34
July5-M1	8.678	2.938	-0.115	0.833	9.218	33.30	0.75	21	0.45	19
July5-M2	9.510	3.065	-0.170	0.850	10.83	36.13	0.87	42	0.41	30
July5-M3	9.534	2.899	-0.191	0.809	10.90	34.87	0.88	42	0.47	29
July5-C4	12.46	2.997	-0.272	0.846	15.04	44.32	0.72	28	0.46	32
July6-M1	8.755	2.952	-0.108	0.836	9.265	33.67	0.89	42	0.41	29
July6-M2	8.864	2.991	-0.097	0.865	9.422	34.16	0.86	37	0.44	27

July6-M3	9.021	2.924	-0.128	0.851	9.681	33.96	0.86	37	0.48	26
July6-C4	10.15	2.997	-0.204	0.839	11.88	37.14	0.83	37	0.44	32
Aug4-M1	8.653	2.949	-0.104	0.844	9.121	33.39	0.78	24	0.45	20
Aug4-M3	9.570	3.048	-0.200	0.841	11.13	35.48	0.82	32	0.38	30
Aug4-C4	13.63	3.069	-0.301	0.897	17.08	47.39	0.6	21	0.39	34
Aug5-M1	8.215	3.093	-0.118	0.815	8.953	33.93	0.71	18	0.34	18
Aug5-M2	9.082	3.063	-0.100	0.867	9.715	35.92	0.79	28	0.43	23
Aug5-M3	9.580	2.892	-0.202	0.812	11.05	34.79	0.85	37	0.47	28
Aug5-C4	15.69	3.150	-0.341	0.915	20.21	51.58	0.61	24	0.44	36
Sep17-M1	9.114	2.878	-0.119	0.827	9.787	34.17	0.66	16	0.52	16
Sep17-M2	15.42	3.284	-0.322	0.884	19.81	58.94	0.65	28	0.39	39
Sep17-M3	9.895	2.884	-0.214	0.863	11.47	35.30	0.81	32	0.48	28
Sep17-C4	12.01	3.226	-0.261	0.870	15.05	46.31	0.67	24	0.37	32
Sep18-M1	7.126	3.020	-0.028	0.833	7.304	29.65	0.56	9	0.19	13
Sep18-M2	8.145	3.022	-0.136	0.828	8.979	29.44	0.85	32	0.37	26
Sep18-M3	9.461	2.945	-0.210	0.835	10.91	34.68	0.85	37	0.45	28
Sep18-C4	11.20	3.111	-0.193	0.843	12.86	39.76	0.77	32	0.43	33
Sep19-M1	8.759	2.956	-0.111	0.842	9.299	34.01	0.7	18	0.46	17
Sep19-M2	9.124	2.940	-0.129	0.842	9.784	34.48	0.88	42	0.47	29
Sep19-M3	9.476	3.003	-0.185	0.862	10.86	35.18	0.82	32	0.45	26
Sep19-C4	10.64	3.099	-0.175	0.845	12.07	38.45	0.85	42	0.45	33
Sep20-M1	8.502	2.934	-0.104	0.850	8.998	29.88	0.82	28	0.44	22
Sep20-M2	7.977	3.234	-0.097	0.769	8.735	34.53	0.81	28	0.17	29
Sep20-M3	8.494	3.139	-0.119	0.835	9.377	34.74	0.86	37	0.34	30
Sep20-C4	13.16	3.155	-0.254	0.878	15.96	48.60	0.69	28	0.41	34
Oct22-M1	7.380	2.973	-0.131	0.812	8.282	28.31	0.84	28	0.28	24
Oct22-M2	7.039	2.919	-0.063	0.815	7.405	27.36	0.69	14	0.3	15
Oct22-M3	9.801	2.930	-0.186	0.899	11.29	35.38	0.85	37	0.5	28
Oct22-C4	13.61	3.233	-0.210	0.888	15.75	49.78	0.76	37	0.47	36
Nov14-M1	8.762	2.948	-0.107	0.839	9.244	33.56	0.74	21	0.47	18
Nov14-M2	7.509	2.945	-0.122	0.897	8.323	28.85	0.68	14	0.34	16
Nov14-M3	9.080	3.001	-0.113	0.853	9.747	34.82	0.83	32	0.43	26
Nov14-C4	10.72	3.091	-0.168	0.842	12.04	38.51	0.85	42	0.46	33
Nov15-M1	8.662	2.919	-0.112	0.853	9.196	29.91	0.78	24	0.48	20
Nov15-M2	7.341	2.847	-0.137	0.904	8.204	26.79	0.73	16	0.47	14
Nov15-M3	8.866	2.941	-0.123	0.838	9.500	33.81	0.81	28	0.45	23
Nov15-C4	10.18	3.189	-0.167	0.799	11.41	37.95	0.77	28	0.38	27
Nov16-M1	7.793	2.891	-0.144	0.898	8.742	28.69	0.79	18	0.49	16
Nov16-M2	7.993	2.778	-0.135	0.901	8.731	27.66	0.74	18	0.52	16
Nov16-M3	7.467	2.845	-0.146	0.894	8.389	26.88	0.75	18	0.47	16
Nov16-C4	9.639	2.982	-0.169	0.852	11.04	35.96	0.79	28	0.48	23

Nov17-M1	8.100	3.007	-0.119	0.833	8.827	29.51	0.85	32	0.4	24
Nov17-M2	6.866	2.741	-0.080	0.826	7.199	25.00	0.74	16	0.52	14
Nov17-M3	8.784	2.904	-0.128	0.849	9.443	29.86	0.78	24	0.49	21
Nov17-C4	8.265	2.774	-0.161	0.850	9.182	28.13	0.69	16	0.51	16
Jan11-M1	7.409	2.806	-0.148	0.905	8.322	26.25	0.72	16	0.52	14
Jan11-M2	8.173	2.963	-0.131	0.837	8.948	28.96	0.76	21	0.47	18
Jan11-M3	8.217	2.786	-0.146	0.907	9.055	28.47	0.83	28	0.51	21
Jan11-C4	15.09	3.234	-0.315	0.879	19.17	51.98	0.7	32	0.43	41
Jan12-M1	8.608	2.883	-0.122	0.838	9.182	29.08	0.72	18	0.5	17
Jan12-M2	8.988	2.863	-0.124	0.812	9.687	33.28	0.83	32	0.48	25
Jan12-M3	8.879	2.904	-0.131	0.842	9.552	30.04	0.84	32	0.48	25
Jan12-C4	10.67	3.070	-0.184	0.834	12.13	38.11	0.79	32	0.45	29
Jan13-M1	9.721	2.998	-0.166	0.841	11.10	36.89	0.81	32	0.46	26
Jan13-M2	8.799	2.961	-0.121	0.829	9.401	33.84	0.84	32	0.4	26
Jan13-M3	7.644	2.839	-0.158	0.902	8.664	27.31	0.81	24	0.49	19
Jan13-C4	10.95	3.144	-0.165	0.844	12.35	44.46	0.84	42	0.45	34
Jan14-M1	8.671	2.939	-0.106	0.845	9.174	33.28	0.78	24	0.45	21
Jan14-M2	9.568	2.866	-0.196	0.824	10.97	34.39	0.82	32	0.51	25
Jan14-M3	8.875	2.921	-0.131	0.838	9.558	33.46	0.84	32	0.45	25
Jan14-C4	11.68	3.162	-0.267	0.812	14.42	44.88	0.76	32	0.37	37
Jan15-M1	8.816	3.037	-0.085	0.861	9.304	34.84	0.88	42	0.4	28
Jan15-M2	8.843	2.975	-0.130	0.826	9.523	33.98	0.83	32	0.39	27
Jan15-M3	8.162	3.065	-0.158	0.803	9.208	29.99	0.78	24	0.28	26
Jan15-C4	10.50	3.153	-0.206	0.841	12.12	37.47	0.76	28	0.37	31
Mar27-M1	10.95	3.210	-0.135	0.869	12.22	45.23	0.86	49	0.44	35
Mar27-M2	11.06	3.226	-0.136	0.869	12.35	45.79	0.83	42	0.44	34
Mar27-M3	12.66	3.392	-0.177	0.878	14.59	51.03	0.86	56	0.43	42
Mar27-C4	10.31	2.951	-0.202	0.868	12.06	36.90	0.83	37	0.53	29
Mar28-M1	11.89	3.308	-0.210	0.868	14.33	48.86	0.84	49	0.41	40
Mar28-M2	9.533	3.027	-0.188	0.851	10.96	35.30	0.87	42	0.43	30
Mar28-M3	10.52	3.090	-0.175	0.840	11.92	38.05	0.9	56	0.46	35
Mar28-C4	11.04	3.093	-0.184	0.848	12.62	39.50	0.78	32	0.47	30
Mar29-M1	10.26	3.148	-0.124	0.803	11.24	39.04	0.88	49	0.41	33
Mar29-M2	10.64	3.108	-0.163	0.842	11.94	38.83	0.9	56	0.45	36
Mar29-M3	10.82	3.188	-0.148	0.833	12.06	45.51	0.83	42	0.41	34
Mar29-C4	12.47	2.986	-0.271	0.866	15.02	43.99	0.72	28	0.49	31
Mar30-M1	11.13	3.306	-0.130	0.867	12.47	47.34	0.85	49	0.4	37
Mar30-M2	9.681	3.080	-0.178	0.849	11.08	36.69	0.89	49	0.41	33
Mar30-M3	10.14	2.974	-0.187	0.905	11.73	36.92	0.83	37	0.49	29
Mar30-C4	14.37	3.184	-0.246	0.887	17.03	50.34	0.71	32	0.47	37
Mar31-M1	11.97	3.302	-0.224	0.855	14.57	48.24	0.91	74	0.43	44

Mar31-M2	10.54	3.154	-0.148	0.833	11.74	39.75	0.87	49	0.4	36
Mar31-M3	11.21	3.192	-0.152	0.873	12.66	45.76	0.88	56	0.46	38
Mar31-C4	13.31	3.062	-0.239	0.896	15.80	48.00	0.84	49	0.54	40
May25-M1	9.127	3.088	-0.086	0.862	9.639	36.83	0.87	42	0.39	30
May25-M2	9.799	2.974	-0.177	0.849	11.27	36.23	0.89	49	0.47	31
May25-M3	11.92	3.226	-0.219	0.875	14.38	47.40	0.85	49	0.46	37
May25-C4	12.35	3.089	-0.215	0.877	14.48	45.76	0.82	42	0.49	35
May26-M1	9.264	3.154	-0.076	0.851	9.732	39.18	0.83	37	0.36	29
May26-M2	9.862	3.007	-0.172	0.839	11.33	37.09	0.89	49	0.45	32
May26-M3	10.61	3.102	-0.145	0.862	11.77	39.15	0.85	42	0.47	31
May26-C4	11.05	3.253	-0.138	0.852	12.34	46.58	0.88	56	0.4	41
May27-M1	10.58	3.145	-0.161	0.836	11.92	39.12	0.87	49	0.42	35
May27-M2	9.765	2.987	-0.167	0.854	11.17	36.54	0.86	42	0.47	29
May27-M3	9.025	3.049	-0.091	0.861	9.586	35.87	0.82	32	0.43	25
May27-C4	13.57	3.287	-0.188	0.818	15.45	51.26	0.82	49	0.44	43
May28-M1	9.763	3.091	-0.169	0.848	11.08	37.82	0.89	49	0.41	33
May28-M2	9.678	3.084	-0.169	0.861	11.01	36.88	0.84	37	0.41	30
May28-M3	10.85	3.061	-0.181	0.840	12.29	38.16	0.82	37	0.47	32
May28-C4	12.85	3.102	-0.239	0.819	15.33	46.83	0.78	37	0.46	38
Jun8-M1	10.78	3.301	-0.107	0.861	11.80	46.76	0.71	24	0.43	22
Jun8-M2	9.733	2.969	-0.179	0.839	11.19	35.85	0.89	49	0.46	32
Jun8-M3	10.69	3.068	-0.151	0.859	11.86	38.48	0.9	56	0.49	34
Jun8-C4	13.30	3.001	-0.299	0.867	16.33	46.37	0.77	37	0.48	42
Jun9-M1	10.61	3.114	-0.164	0.844	11.95	38.41	0.85	42	0.45	32
Jun9-M2	11.06	3.131	-0.173	0.837	12.52	44.29	0.83	42	0.45	35
Jun9-M3	10.75	3.045	-0.159	0.860	11.99	38.34	0.88	49	0.53	32
Jun9-C4	10.99	3.075	-0.188	0.842	12.52	38.78	0.89	56	0.51	35
Jun10-M1	9.598	3.106	-0.175	0.859	11.00	37.30	0.92	64	0.37	38
Jun10-M2	10.95	3.145	-0.163	0.846	12.32	44.33	0.84	42	0.45	33
Jun10-M3	12.92	3.516	-0.158	0.881	15.03	59.24	0.82	49	0.45	37
Jun10-C4	11.98	3.200	-0.232	0.874	14.53	46.45	0.85	49	0.47	38
Jun11-M1	10.59	3.128	-0.153	0.838	11.83	39.27	0.85	42	0.44	33
Jun11-M2	11.15	3.281	-0.151	0.855	12.67	47.23	0.82	42	0.39	36
Jun11-M3	9.975	3.012	-0.181	0.836	11.51	37.30	0.83	37	0.44	30
Jun11-C4	12.86	3.043	-0.263	0.859	15.37	46.58	0.81	42	0.48	39
Jun12-M1	10.47	3.215	-0.175	0.807	11.83	39.09	0.9	56	0.4	38
Jun12-M2	11.15	3.178	-0.161	0.839	12.51	45.73	0.86	49	0.43	38
Jun12-M3	11.35	3.103	-0.189	0.851	12.97	44.59	0.86	49	0.49	36
Jun12-C4	15.01	3.196	-0.331	0.895	19.36	49.97	0.7	32	0.41	48

APPENDIX D

Summary of deposition and concentration from RBR and ISCO

Tide	Marsh Surface Deposition (g/m^2)	Marsh Edge Deposition (g/m^2)	Marsh Bank Deposition (g/m^2)	Creek Deposition (g/m^2)	RBR Mean Concentration (mg/l)	ISCO Mean Concentration (mg/l)
May5am	9.3	8.8	11.9	29.3	119	
May5pm	16.2	15.6	21.7	29.1	121	64
May6am	12.7	11.6	18.9	25.2	121	50
May6pm	17.7	11.2	19.5	24.9	138	59
May7am	12.7	10.7	17.6	20.4	129	
May7pm	14.9	11.4	14.5	31.7	136	61
May8am	10.7	18.9	20.2	26.0	134	49
May8pm	12.2	10.3	14.3	27.3	142	48
May9am	9.2	3.2	14.4	24.6	145	49
July4am	14.4	21.1	30.9	112.6	129	37
July4pm	15.4	12.2	23.2	51.9	116	42
July5am	3.1	3.8	3.2	64.4	139	42
July5pm	13.5	9.1	26.5	72.0	150	30
July6am	9.0	6.5	23.4	69.7	142	32
Aug4am	15.4	16.9	35.5	25.1	273	67
Aug4pm	20.7	16.5	19.8	53.1	101	65
Aug5am	14.0	16.8	22.8	31.0	123	
Sep17am	10.8	10.2	13.0	28.5	116	38
Sep17pm	10.6	10.4	20.0	21.2	105	37
Sep18am	11.9	11.5	10.5	34.1	120	36
Sep18pm	24.3	10.9	13.9	37.9	97	53
Sep19am	14.5	10.5	12.7	30.6	161	56
Sep19pm	7.4	6.8	9.4	410.3	154	42
Sep20am	7.7	8.5	27.4	19.7	235	50
Nov14am	3.1	2.0	21.3	224.7	532	37
Nov14pm	23.9	3.9	77.2	99.4	366	
Nov15am	30.2	10.5	19.2	190.6	655	74
Nov15pm	45.4	17.9	70.2	45.6	526	53
Nov16am	17.5	17.9	155.2	83.4	395	23
Nov16pm	27.1	26.7	61.8	38.1	483	16
Nov17am	12.8	16.3	23.4	32.2	294	26
Jan11pm	42.7	10.9	134.6	145.6	783	35
Jan12am					295	
Jan12pm	23.1	46.7	57.5	51.0		46
Jan13am	12.2	23.1	29.5	38.2		
Jan13pm	11.7	21.7	24.3	23.7		36
Jan14pm	13.5	16.0	11.1	20.3		37
Jan15am	11.8	16.5	20.8	35.2		33
Mar27pm	20.8	9.6	10.6	180.7	222	61
Mar28am	23.6	21.3	76.9	278.0	286	61

Mar28pm	21.6	39.2	106.6	301.8	256	62
Mar29am	16.9	22.6	17.2	109.3	213	53
Mar29pm	17.6	26.7	44.8	59.7	174	50
Mar30am	11.0	35.2	36.3	33.1	142	47
Mar30pm	11.0	22.4	32.9	41.7	130	46
Mar31am	14.9	31.6	30.0	19.3	116	46
May25am	2.1	2.3	6.3	25.6	197	95
May25pm	6.3	4.3	8.7	34.6	254	97
May26am	13.0	13.3	40.7	65.7	166	55
May26pm	13.7	11.2	15.3	122.3	415	79
May27am	15.5	9.5	30.9	57.0	723	71
May27pm	17.1	10.8	30.4	39.5	237	28
May28am	11.4	12.2	25.6	25.2	218	19
Jun8am	0.6	0.4	0.6		123	49
Jun8pm	0.8	1.1	9.9		406	60
Jun9am	7.6	6.3	7.6	42.5	220	57
Jun9pm	0.0	10.4	14.6	26.8	159	55
Jun10am	7.9	7.5	11.2	22.7	145	38
Jun10pm	0.0	12.3	10.7	20.0	105	43
Jun11am	11.0	8.1	16.5	21.3	116	48
Jun11pm	0.0	9.5	9.8	18.7	97	46
Jun12am	1.8	1.7	2.8	19.6	229	50

APPENDIX E

Wind speed and direction during all deployments